THEORETICAL AND EXPERIMENTAL INVESTIGATIONS ON ATOMIC AND MAGNETIC ORDERING IN FULL HEUSLER ALLOYS

A THESIS SUBMITTED TO
THE GRADUATE SCHOOL OF NATURAL AND APPLIED SCIENCES
OF
MIDDLE EAST TECHNICAL UNIVERSITY

BY

CEM TOPBAŞI

IN PARTIAL FULFILLMENT OF THE REQUIREMENTS
FOR
THE DEGREE OF MASTER OF SCIENCE
IN
METALLURGICAL AND MATERIALS ENGINEERING

JUNE 2008

Approval of the thesis:

THEORETICAL AND EXPERIMENTAL INVESTIGATIONS ON ATOMIC AND MAGNETIC ORDERING IN FULL HEUSLER ALLOYS

Submitted by **CEM TOPBAŞI** in partial fulfillment of the requirements for the degree of **Master of Science in Metallurgical and Materials Engineering Department, Middle East Technical University** by,

Prof. Dr. Canan Özgen _____
Dean, Graduate School of **Natural and Applied Sciences**

Prof. Dr. Tayfur Öztürk _____
Head of Department, **Metallurgical and Materials Engineering**

Prof. Dr. M. Vedat Akdeniz _____
Supervisor, **Metallurgical and Materials Engineering Dept., METU**

Prof. Dr. Amdulla O. Mekhrabov _____
Co-Supervisor, **Metallurgical and Materials Engineering Dept., METU**

Examining Committee Members:

Prof. Dr. Macit Özenbaş _____
Metallurgical and Materials Engineering Dept., METU

Prof. Dr. M. Vedat Akdeniz _____
Metallurgical and Materials Engineering Dept., METU

Prof. Dr. Amdulla O. Mekhrabov _____
Metallurgical and Materials Engineering Dept., METU

Prof. Dr. Ayhan Elmalı _____
Physics Engineering Dept., A.U.

Assist. Prof. Dr. Arcan F. Dericioğlu _____
Metallurgical and Materials Engineering Dept., METU

Date: 19.06.2008

I hereby declare that all information in this document has been obtained and presented accordance with the academic rules and ethical conduct. I also declare that, as required by these rules and conduct, I have fully cited and referenced all material and results that are not original to this work.

Name, Last name: Cem Topbaşı

Signature :

ABSTRACT

THEORETICAL AND EXPERIMENTAL INVESTIGATIONS ON ATOMIC AND MAGNETIC ORDERING IN FULL HEUSLER ALLOYS

Topbaşı, Cem

M.S. Department of Metallurgical and Materials Engineering

Supervisor: Prof. Dr. M. Vedat Akdeniz

Co-Supervisor: Prof. Dr. Amdulla O. Mekhrabov

June 2008, 159 pages

The aim of the study, which was carried out in two main parts, was to investigate the atomic and magnetic ordering in various full Heusler alloy systems.

In the theoretical part of the thesis, investigations based on the statisco-thermodynamical theory of ordering by means of Bragg-Williams-Gorsky (BWG) method combined with electronic theory in the pseudopotential approximation have been conducted to model order-order ($L2_1 \leftrightarrow B2$) and order-disorder ($B2 \leftrightarrow A2$) phase transformations in Ni-Mn-C (C=Ga, In, Sb) and A_2BGa (A=Fe, Ni, Co; B=Ni, Mn, Co, Fe) Heusler alloys. The partial ordering energies, calculated according to the electronic theory of alloys in pseudopotential approximation for the first two coordination spheres were utilized as input data for the theoretical superlattice formation models based on BWG approximation. Furthermore, the trends of $L2_1 \leftrightarrow B2$ transition temperatures with electron concentration at A, B and C atomic sites were determined.

In the experimental part of the thesis, structural and magnetic properties of Ni-Mn-Ga and Ni-Mn-Al Heusler alloys were investigated. For the Ni-Mn-Ga Heusler alloy system, it was found that the martensitic (T_M) and Curie temperatures (T_C) merge for $Ni_{54}Mn_{20}Ga_{26}$ and $Ni_{56}Mn_{18}Ga_{26}$ alloys by compositional tuning. For the Ni-Mn-Al Heusler alloy system, it was found that ferromagnetism was introduced into these alloys by low temperature aging, as a result of the stabilization of the $L2_1$ phase. In addition to that, magnetocaloric effect (MCE) was determined in the vicinity of the first order magneto-structural transition for Ni-rich Ni-Mn-Ga alloys and near the second order magnetic transition for the Ni_2MnAl alloy.

Keywords: Atomic Ordering, BWG Approximation, Ferromagnetism, Heusler Alloys, Magnetocaloric Effect.

ÖZ

TAM HEUSLER ALAŞIMLARINDAKİ ATOMİK VE MANYETİK DÜZENLENMENİN TEORİK VE DENEYSEL OLARAK ARAŞTIRILMASI

Topbaşı, Cem
Y. Lisans, Metalurji ve Malzeme Mühendisliği Bölümü
Tez Yöneticisi: Prof. Dr. M. Vedat Akdeniz
Ortak Tez Yöneticisi: Prof. Dr. Amdulla O. Mekhrabov

Haziran 2008, 159 sayfa

İki ana kısımda yürütülmüş olan bu çalışmanın amacı çeşitli Heusler alaşım sistemlerindeki atomik ve manyetik düzenlenmeyi incelemektir.

Tezin teorik kısımında, istatistiksel-termodinamik teorinin Bragg-Williams-Gorsky (BWG) metodu ile elektronik teorinin psödopotansiyel yaklaşımı kullanılarak Ni-Mn-C (C=Ga, In, Sb) ve A_2BGa (A=Fe, Ni, Co; B=Ni, Mn, Co, Fe) Heusler alaşımlarındaki düzen-düzen ($L2_1 \leftrightarrow B2$) ve düzen-düzensizlik ($B2 \leftrightarrow A2$) faz dönüşümleri modellenmiştir. Elektronik teorinin psödopotansiyel yaklaşımına göre ilk iki kordinasyon yarıçapı için hesaplanan kısmi düzenlenme enerjileri, BWG yaklaşımını temel alan teorik süper-örgü oluşum modellerine girdi verisi olarak kullanılmıştır. Buna ilaveten, $L2_1 \leftrightarrow B2$ dönüşüm sıcaklıklarının A, B ve C atomik konumlarındaki elektron konsantrasyonu ile değişimi belirlenmiştir.

Tezin deneysel kısmında, Ni-Mn-Ga ve Ni-Mn-Al Heusler alaşım sistemlerinin yapısal ve manyetik özellikleri incelenmiştir. Ni-Mn-Ga Heulser alaşım sisteminde

kompozisyon ayarlanarak martenzitik (T_M) ve Curie (T_C) dönüşüm sıcaklıkları $Ni_{54}Mn_{20}Ga_{26}$ ve $Ni_{56}Mn_{18}Ga_{26}$ alaşımları için birleştirilmiştir. Ni-Mn-Al Heusler alaşım sisteminde, düşük sıcaklık yaşlandırma ile $L2_1$ fazının miktarı arttırılarak ferromanyetik özellik kazandırılmıştır. Bunlara ek olarak, manyetokalorik etki, Ni'ce zengin Ni-Mn-Ga alaşımları için birinci derece yapısal-manyetik dönüşüm civarında, stokiyometrik Ni_2MnAl alaşımı için ise ikinici derece manyetik dönüşüm yakınıda belirlenmiştir.

Anahtar Sözcükler: Atomik Düzenlenme, BWG Yaklaşımı, Ferromanyetizma, Heusler Alaşımları, Manyetokalorik Etki.

To my beloved parents;
Filiz and O. Dogan Topbasi

ACKNOWLEDGEMENTS

I would like to express my gratitude to my supervisors Prof. Dr. M. Vedat Akdeniz and Prof. Dr. Amdulla O. Mekhrabov for their supervision, guidance, support and encouragement during this study. They have always trusted me and given me the freedom of doing independent research work.

I am sincerely greateful to Prof. Dr. Macit Özenbaş for supporting me throughout my thesis studies.

I would like to express my most sincere thanks to Prof. Dr. Ayhan Elmalı for mentoring me during my undergraduate and graduate years.

I must thank all of my labmates; Muratahan Aykol for his helpful discussions and stimulating ideas in and out the lab, Nagehan Duman for being so encouraging and supportive all the time, Mehmet Yıldırım for always lending a helping hand, Sıla Süer and Ozan Özkan for their sympathy and kindness, Sultan Aybar, an old but not forgotten labmate, for passing her experience and being there for me.

I would also thank Nihat Ali Işıtman and Serhat Ün for their valuable friendship and unconditional support.

This study was supported by the State Planning Organization (DPT) Grant No: BAP-03-08-DPT-2003 (06) K120920-19.

TABLE OF CONTENTS

LIST OF TABLES

LIST OF FIGURES

LIST OF SYMBOLS

ΔS_M	Magnetic entropy change
ΔT_{ad}	Adiabatic temperature change
T	Temperature
p	Pressure
V	Volume
T_C	Curie temperature
H	Magnetic field
M	Magnetization
T_M	Martensitic transformation temperature
T_P	Premartensitic transition temperature
A_s	Austenite-start temperature
A_f	Austenite-finish temperature
M_s	Martensite-start temperature
M_f	Martensite-finish temperature
M_{sat}	Saturation magnetization
e/a	Electron concentration
LRO	Long range order
η_i	i-th long range order parameter
R	Interatomic distance
R_i	Radius of the i-th coordination sphere
$W^{AB}(R_i)$	Partial ordering energy between A and B atoms at R_i
$V^{AB}(R_i)$	Pairwise interaction energies between A and B atoms at R_i
P_A^{α}	Probability of finding A atom in α lattice site
x_A	Atomic fraction of A atom
E_i	Potential energy of a system considering interactions of atoms at Ri
Φ	Configurational entropy.
Tc_1	B2↔A2 phase transition temperature
Tc_2	$L2_1$↔B2 phase transition temperature

$\bar{\Omega}_0$	Average atomic volume of the ternary alloy
ε(q)	Dielectric constant in Hartree approximation
ε*(q)	Modified dielectric constant
k	Boltzmann's constant
ω_i^0	Form factor of an unscreened pseudopotential of i component ion
φ	Ewald parameter
Z_i^*	Effective valency of the i component atom

CHAPTER 1

INTRODUCTION

Full Heusler alloys are magnetic ternary intermetallic compounds with the $L2_1$-type crystal structure. Typically, these alloys undergo a low temperature martensitic transformation (austenite↔martensite), a magnetic transformation (ferromagnetic ↔paramagnetic) and relatively high temperature atomic ordering (order↔order and order↔disorder) transformations.

After the discovery of the ferromagnetic shape memory (FSM) and giant magnetocaloric effects (GMCE) in Ni-Mn-Ga alloy, Ni-Mn based Heusler alloys have received considerable attention due to their unique magnetic and structural properties [1-9]. Ni-Mn based Heusler alloys which exhibit GMCE can be used as magnetic refrigerant materials in magnetic refrigerators. Magnetic refrigeration (MR) is an alternative cooling technology which offers high energy efficiency. A large MCE (the change in magnetic entropy, ΔS_M) of 5 $JKg^{-1}K^{-1}$ was reported for Ni-Mn-Ga alloys for the second order magnetic transition (ferromagnetic ↔paramagnetic) [5, 10]. However, the highest ΔS_M values of ~20 $JKg^{-1}K^{-1}$ were obtained at the coupled magnetic (ferromagnetic↔paramagnetic) and structural (martensite↔austenite) transition in Ni-Mn-Ga Heusler alloys [7, 10]. The coupled (magneto-structural) transition can be achieved through compositional tuning of the structural and magnetic transitions temperatures.

On the other hand, ferromagnetic shape memory effect observed in Ni-Mn based Heusler alloys allows these alloys to be used as magnetically driven sensors and actuators. Ferromagnetic shape memory alloys offer a faster response time and

better energy conversion than conventional shape memory alloys, piezoelectric ceramics and megnetostrictive materials.

This makes the Ni-Mn based Heusler alloys center of attention for basic research and investigation, leading to technological applications as a working body in MRs and sensors or actuators in intelligent systems.

A promising alternative for the Ni-Mn-Ga Heusler alloy system is the Ni-Mn-Al Heusler system. Ni-Mn-Al Heusler alloys have the potential to replace Ni-Mn-Ga Heusler alloys in MR and FSM applications since Ni-Mn-Al alloys offer better mechanical properties, cost less and are easier to produce. Ni-Mn-Al alloys exhibit similar structural transformations to the Ni-Mn-Ga alloys. Nevertheless, the ferromagnetic $L2_1$ phase which is readily stabilized in Ni-Mn-Ga alloys could not be stabilized in Ni-Mn-Al alloys in previous studies as a single phase. Ferromagnetism plays a crucial role in both magnetocaloric and FSM properties and long term aging (near 660 K) is necessary to increase the amount of ferromagnetic $L2_1$ phase in these alloys due to the lower $L2_1 \leftrightarrow B2$ transition temperatures of these alloys.

The martensitic and magnetic phase transformations in Heusler alloys have been investigated extensively [2, 3]. However, the high temperature order-order and order-disorder phase transformations which were reported to affect the stability of the bcc phase [11, 12] and magnetic properties [13] were studied to a smaller extent [14-16]. Previous investigations concerning high temperature (order-order) $L2_1 \leftrightarrow B2$ transformation mainly involve fitting of experimental data to typical parabolic curves based on Bragg-Williams-Gorsky (BWG) approximation. It was also shown that the $L2_1 \leftrightarrow B2$ transformation temperature depends on valence electron concentration of atoms at lattice sites of A [17, 18] or B and C [19, 20] in A_2BC –type ordered Heusler alloys. Furthermore, the statisco-thermodynamical treatments based on BWG approximations have been utilized in order to calculate $B2 \leftrightarrow A2$ and $L2_1 \leftrightarrow B2$ critical transformation temperatures [14, 21]. Nevertheless,

the problem of order-order and/or order-disorder phase transformations in solids is a typical many-particle problem that can not be treated exactly by analytical and statistical-thermodynamical methods. It seems likely that atomic ordering processes in A_2BC–type ordered full Heusler alloys occur mainly at the first and second coordination spheres by the rearrangement of atoms into ordered sublattices. Therefore, realistic description of the atomic ordering mechanism and order-order and/or order-disorder transformation phenomena in these alloys require the magnitudes of interatomic interaction and/or partial ordering energies between constitute element atoms in the first and second coordination spheres.

Present thesis aims in general to investigate the atomic and magnetic ordering in Ni-Mn based Heusler alloys. The studies are carried out in two main parts. The theoretical part involves the modelling and simulation of atomic ordering processes in full Heusler alloys and experimental part involves the investigation of structural, magnetic and magnetocaloric properties of Ni-Mn-Ga and Ni-Mn-Al Heusler alloys.

The purpose of the theoretical part of the thesis is to investigate the general trends of B2↔A2 order-disorder and $L2_1$↔B2 order-order high temperature phase transformations in full Heusler alloys. In this respect, the present theoretical studies involve, for the first time, the combination of statisco-thermodynamical theory of ordering by means of BWG method with electronic theory in the pseudopotential approximation to predict B2↔A2 and $L2_1$↔B2 critical transformation temperatures which inevitably occurs A_2BC–type ordered full Heusler alloys.

In the experimental part of the present thesis, structural and magnetic properties of Ni-Mn-Ga and Ni-Mn-Al Heusler alloy systems were investigated by means of X-ray diffraction (XRD), scanning electron microscopy (SEM) and vibrating sample magnetometer (VSM) measurements. The goal of the studies conducted for the Ni-Mn-Ga system was to investigate compositional dependence of structural and magnetic properties of Ni-rich Ni-Mn-Ga Heusler alloys and furthermore, to

determine a composition where a magneto-structural transformation occurs and to measure the MCE near this temperature. The studies performed for the Ni-Mn-Al system aimed to investigate the effects of low temperature aging for various time periods (12, 24 and 48 days) on the stabilization of the $L2_1$ phase and magnetic properties in $Ni_{50}Mn_{50-x}Al_x$ alloys ($10<x<40$) and in addition to that, to determine MCE for the 48 day-aged Ni_2MnAl alloy.

CHAPTER 2

MAGNETIC REFRIGERATION AND MAGNETOCALORIC EFFECT

Today, the refrigeration system is completely based on the vapor-compression cycle. It is a well established and reliable technology. As a result of extended research focused on the improvement of the conventional refrigerator system, the highest limit of energy efficiency was reached and the predicted advances are incremental. In addition to that, various refrigerant materials are ozone depleting gases or hazardous materials.

Magnetic refrigeration (MR) is a promising alternative for the conventional compressor based refrigeration in use today. Primarily, MR offers high energy efficiency [22-25]. In a MR system, the energy-consuming compressor of the conventional refrigerator system is replaced by a magnetic refrigrant material and a permanent magnet. Furthermore, MRs are expected to have a much more compact design and generate less noise than the conventional refigerator units. In addition to that, MR is an environmental friendly technology because of the elimination of ozone depleting gases and hazardous refrigerant materials.

MR is based on the magnetocaloric effect (MCE*)* which is described as the change in the temperature of a material due to the application of a magnetic field. Warburg discovered MCE in iron in 1881 [26]. Debye [27] and Giauque [28] clarified the nature of MCE and later suggested cooling by means of adiabatic demagnetization. In 1933, Giauque and MacDougall [29] reached 0.25 K by adiabatic demagnetization. Up to 1997, there had been improvements about the utilization of MCE for cooling but in 1997, the proof-of-principle MR with potential energy savings up to 30% was presented [30]. While the first MR prototypes required large superconducting magnets, a later version utilizes the field of a permanent magnet

and runs virtually silent and vibration free, proving the viability of a compact MR unit [31].

To design a successful MR unit; the performance of the magnets can be increased, the engineering of the MR which covers the design of refrigeration cycle, planning of the heat transfer flow and the heat exchange can be improved but the most important part of the MR is the magnetic refrigerant material which determines the viability of proposed system.

The magnetic properties of materials result from magnetic moments carried by electrons (caused by orbital and spin motion of electrons) and the interaction between them. *Diamagnetic materials* have no net magnetic moment unless a field is applied. External magnetic field induces a net magnetic moment which opposes the applied magnetic field. *Paramagnetic materials* have a non-zero magnetic moment because of the unpaired electrons. Without an applied magnetic field, the magnetic moments are randomly oriented. The degree of allignment depends on the strength of the applied magnetic field. The net magnetization, M, has a linear dependency on the applied magnetic field, H. The *ferri- and ferromagnetic materials* have a spontaneous magnetization even in the absence of the magnetic field as a result of the strong interactions between the magnetic moments. Significantly larger magnetization values can be obtained in these materials than the *para- and antiferromagnetic materials*. In addition to that, magnetization increases and reaches a maximum value called the saturation magnetization, M_{sat}, on the application of an external magnetic field. As the applied field decreases, magnetization decreases slowly but does not reduce to zero. This irreversibility of magnetization is called hysteresis. This is a major characteristic of ferromagnetic materials. Above a certain temperature called the Curie temperature, T_c, the long range magnetic order does not exist. In *antifferromagnetic materials* spins are arranged antiparallel to each other and their moments cancel each other. M-H curves of the antiferromagnetic materials exhibit a linear behavior.similar to the paramagnetic materials.

Most of the magnetic materials order through a second order magnetic transition like the ferromagnet, ferrimagnet or antiferromagnet↔paramagnet transitions. These materials exhibit conventional MCE. Several materials, nevertheless, order ferromagnetically through a first order magnetic phase transition, which may be coupled with a change of the crystal structure. Coupled magnetic and structural transitions (magneto-structural transition) results in quite large MCE values. Such behaviour is named as giant magnetocaloric effect (GMCE) by Pecharsky and Gschneidner in 1997 [32]. They observed GMCE in Gd-Si-Ge compounds through a magnetostructural transition. This can be accepted as a milestone for the MR technology [32]. Since then there has been a growing interest in magnetocaloric materials. Figure 2.1 shows the number of publications related to MCE between 1990 and 2007. Other canditate magnetic refrigerant materials which exhibit GMCE include, Ni-Mn-Ga [7], La-Fe-Si-(Hi) [33-35] and Mn-As-(Fe, Sb, P) [36-38] compounds.

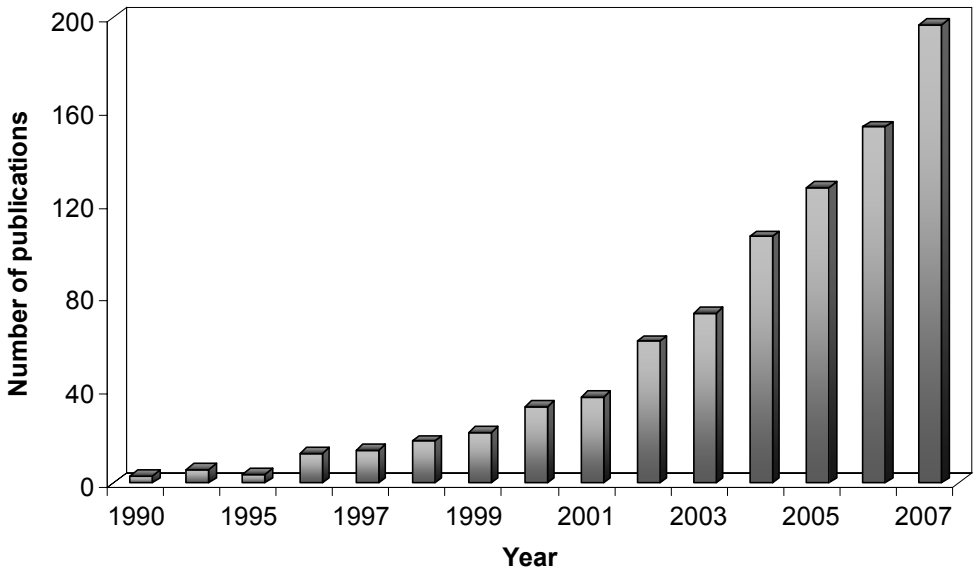

Figure 2.1 Number of publications related to MCE published between 1990 and 2007 (numbers were taken from the ISI database).

2.1 FUNDAMENTALS OF MAGNETOCALORIC EFFECT

MCE is expressed quantitatively as the adiabatic temperature change (ΔT_{ad}) and the isothermal magnetic entropy change (ΔS_M). ΔT_{ad} and ΔS_M are functions of the initial temperature (i.e the temperature before the magnetic field was changed) and the magnetic field change ($\Delta H=H_1-H_0$). Under constant pressure, total entropy of a magnetic material can be approximated as a sum of magnetic (S_M), lattice (S_L) and electron (S_E) parts [39].

$$S(H,T) = S_M(H,T) + S_L(T) + S_E(T) \quad \textbf{(2.1)}$$

A representitive entropy (S)-temperature (T) diagram of a magnetic material is shown in Figure 2.2. Blue lines represent the entropy in the absence of a magnetic field (H_0=0) and in non-zero ($H_1 \neq 0$) magnetic field. The horizontal and vertical arrows demonstrate the ΔT_{ad} and the ΔS_M, respectively. The green line represents the non-magnetic part of the entropy (S_L+S_E) and the red lines show the magnetic entropy in zero and non-zero magnetic fields. S_0 and T_0 are zero field entropy and temperature and similarly, S_1 and T_1 are entropy and temperature at the non-zero magnetic field (H_1).

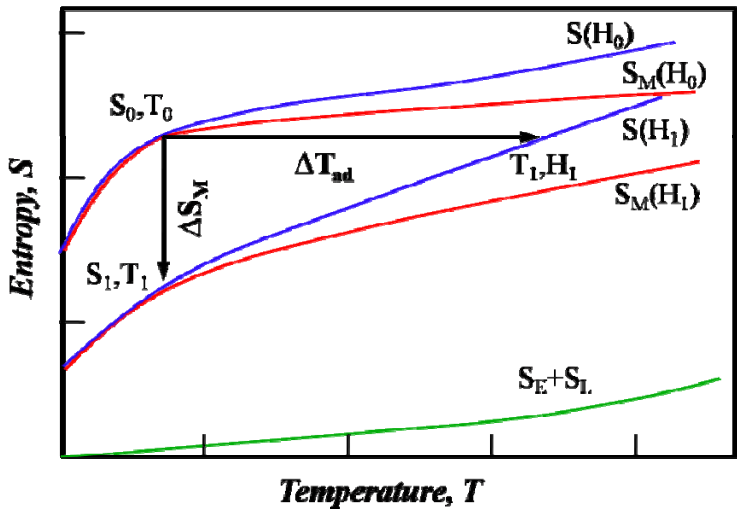

Figure 2.2 S-T diagram of a magnetic material.

In order to describe MCE, internal energy (U), free energy (F) and the Gibbs free energy (G) are used. The internal enegy (U) of a system can be expressed as a function of the volume (V), the entropy (S), magnetic field (H) or as a function of or as a function of V,S and magnetic moment M [40-42]

The total differential of U can be written as

$$dU = TdS - pdV - MdH \qquad \textbf{(2.2.a)}$$

$$dU = TdS - pdV - HdM \qquad \textbf{(2.2.b)}$$

Where T is the absolute temperature and p is the pressure. The free energy (F) which can be represented as a function of V, T and H is defined for systems for under constant volume as [40-42]

$$F = U - TS \qquad \textbf{(2.3)}$$

With the total differential

$$dF = -SdT - pdV - MdH \tag{2.4}$$

The Gibbs free energy (G) which can be a expressed as a function of T, p and H and used for systems under constant presssure [40-42]

$$G = U - TS + pV - MH \tag{2.5}$$

The total differential has the form

$$dG = -SdT + Vdp - MdH \tag{2.6}$$

For the free energy (F), the internal parameters S, p and M conjugated to external variables T, V and H can be determined by the following equations of state [40-42]

$$S(T,H,V) = -\left(\frac{\partial F}{\partial T}\right)_{H,V} \tag{2.7.a}$$

$$M(T,H,V) = -\left(\frac{\partial F}{\partial H}\right)_{V,T} \tag{2.7.b}$$

$$p(T,H,V) = -\left(\frac{\partial F}{\partial V}\right)_{H,T} \tag{2.7.c}$$

Analogously, for the Gibbs free energy we have the following equations [40-42]

$$S(T,H,V) = -\left(\frac{\partial G}{\partial T}\right)_{H,p} \tag{2.8.a}$$

$$M(T,H,V) = -\left(\frac{\partial G}{\partial H}\right)_{T,p} \qquad \textbf{(2.8.b)}$$

$$p(T,H,V) = -\left(\frac{\partial F}{\partial V}\right)_{H,T} \qquad \textbf{(2.8.c)}$$

If the magnetic moment (M) is chosen as an external variable instead of the magnetic field H, then

$$H = -\left(\frac{\partial G}{\partial M}\right)_{T,p} \qquad \textbf{(2.9)}$$

So-called Maxwell Equations can be obrained from the equaitions [40-42]

$$\left(\frac{\partial S}{\partial H}\right)_{T,p} = \left(\frac{\partial M}{\partial T}\right)_{H,p} \qquad \textbf{(2.10.a)}$$

$$\left(\frac{\partial S}{\partial p}\right)_{T,H} = -\left(\frac{\partial V}{\partial T}\right)_{H,p} \qquad \textbf{(2.10.b)}$$

$$\left(\frac{\partial S}{\partial M}\right)_{T,p} = -\left(\frac{\partial H}{\partial T}\right)_{M,p} \qquad \textbf{(2.10.c)}$$

The finite isothermal entropy change under change of magnetic field can be calculated by using the Maxwell Equation (2.10.a)

$$\Delta S_m(T,H) = S_M(H_1,T) - S_M(H_0,T) = -\int_{H_0}^{H_1}\left(\frac{\partial M}{\partial T}\right)_H dH \qquad \textbf{(2.11)}$$

It is evident that from Equation 2.11 that, $|\Delta S_M|$ is large when $\left(\partial M/\partial T\right)_H$ is large. A large change in magnetization is aimed near RT for magnetic refrigerant materials. Since $\left(\partial M/\partial T\right)_H$ peaks at the magnetic ordering temperature, a quite large MCE is expected close to this magnetic phase tansition. This effect can be maximized when the magnetic phase transformation is accompanied with a structural transition.

2.2 METHODS OF MAGNETOCALORIC PROPERTIES INVESTIGATION

MCE measurements can be performed directly or indirectly. In direct measurements, the material is subjected to a varying magnetic field and the temperature change of the material is directly measured whereas, in the indirect measurements the MCE is determined by using magnetization data.

2.2.1 Direct Measurements

The direct measurements of ΔS_M is inconvenient but ΔT_{ad} can be directly determined by directly measuring the temperatures of a magnetic material under a changing external magnetic field [43-45]. Measuring the initial (T_0) and final (T_1) tempeartures of the sample under a magnetic field change (H_1-H_0) is necesssary in direct measurements of MCE. ΔT_{ad} can be expressed as

$$\Delta T_{ad}(T_0, H_1 - H_0) = T_1 - T_0 \qquad \textbf{(2.12)}$$

A sudden change in the applied magnetic field is needed to conduct direct measurements. The measurements can be performed on stationary samples by changing the field or by moving the sample in and out of an external magnetic field. Direct measuremnets of MCE under 10 to 40 kOe have been reported. Employing electromagnets in direct measurements usually restricts the magnetic field to below 20 kOe.

The accuracy of direct measurement depends on the errors the thermometry and external magnetic field setting, degree of the insulation of sample, etc. Considering all these sources of error, accuracy is reported to be 5-10% range.

2.2.2 Indirect Measurements

Unlike direct measurements which yield ΔT_{ad} only, indirect measurements allow one to calculate both the ΔS_M and ΔT_{ad} from heat capacity measuremnts, or ΔS_M from isothermal magnetization maeasurements.

Experimentally determined M(H) isotherms can be used to calculate ΔS_M by employing Equation (2.11). For magnetization measurements made at dicrete temperature intervals ΔS_M can be calculated by numerical integration of Equation (2.11), which can be given by

$$\Delta S_m(T,H) = \sum_i \frac{M_{i+1}(T_{i+1},H) - M_i(T_i,H)}{T_{i+1} - T_i} \Delta H \qquad \textbf{(2.13)}$$

Where $M_{i+1}(T_{i+1},B)$ and $M_i(T_i,B)$ represent the values of the magnetization in a magnetic field H at the temperatures T_{i+1} and T_i, respectively. Equation (2.13) can be used for calculations of ΔS_M from M(H) isotherms when the sample undergoes a second order transformation since at the first order transformation $\left(\partial M/\partial T\right)_H$ is infinite. Nevertheless, $\left(\partial M/\partial T\right)_H$ goes to infinity only in ideal first-order phase transitions and in real materials the $\left(\partial M/\partial T\right)_H$ has finite values. This allows one to use Equation (2.13) in this case.

2.3 MAGNETIC REFRIGERATION

The processes that occur in a magnetic refrigerant material under a changing magnetic field are analogues to the processes that occur in a gaseous system under varying pressure. A MR cycle is shown in Figure 2.3.

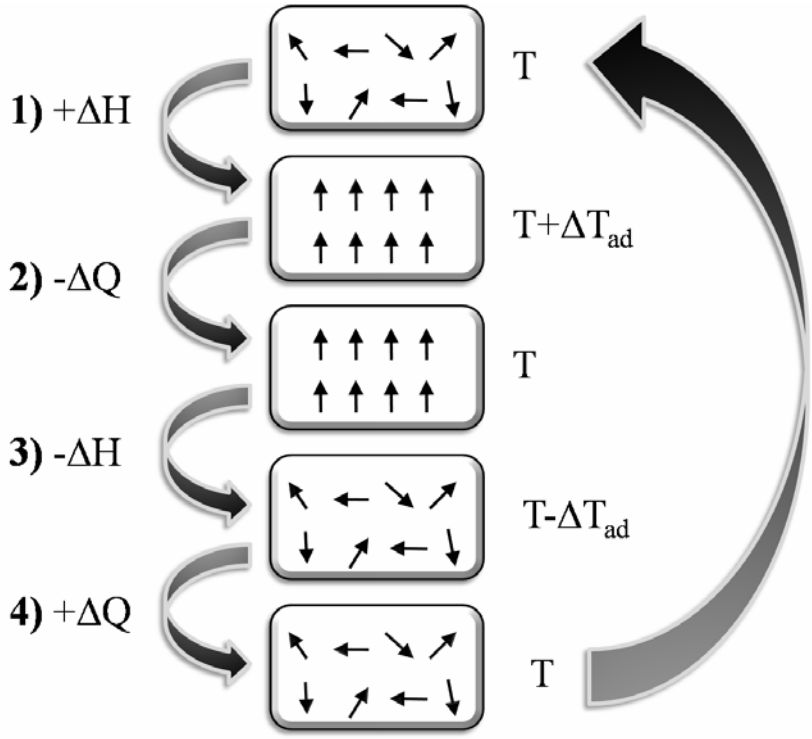

Figure 2.3 A MR cycle.

1) Adiabatic Magnetization: Similar to the adiabatic compression of a gas which results in the increase of the velocities of the constituent molecules in order to maintain the total entropy constant, the application of an external magnetic field under adiabatic conditions results in the alignment of spins and the decrease in S_M is compensated by the increase in the S_L and S_E in order to keep the total entropy constant. This generates lattice vibrations and the increase in the temperature of the magnetic material ($+\Delta T_{ad}$).

2) The added heat (+Q) can be taken away from the system by the cooling body under the constant external magnetic field for the MR and constant pressure for the conventional refrigerator. Once sufficiently cooled the external magnetic field can be removed.

3) Adiabatic Demagnetization: When the the external magnetic field is decreased under adiabatic conditions (total entropy constant) magnetic part of the entropy, S_M, increases and in order to maintain the total entropy (S_L+S_E+S_M) constant and compansate for the increase in the S_M , (S_E+S_M) should decrease. This results in the decrease in the lattice vibrations and the decrease in the temperature of the magnetic material.

4) Under constant magnetic field, the magnetic material cools the medium to be refrigerated. Once the magnetic refrigerant and the refrigerated medium are in thermal equilibrium, the cycle repeats itself.

CHAPTER 3

FERROMAGNETIC SHAPE MEMORY EFFECT

Recently, actuator materials received great interest for the application of these smart materials in various intelligent systems. Actuator materials which combine large strains, high force production and fast dynamic response are needed for those applications. Different physical mechanisms are responsible for electric, magnetic or thermal energy transformations into mechanical work. These mechanisms which produce the actuation determine the functionality of these materials. The reverse energy conversion is used for sensing.

3.1 MECHANISMS OF SHAPE MEMORY AND FERROMAGNETIC SHAPE MEMORY EFFECTS

Magnetostrictive materials, piezoelectric ceramics and shape memory alloys (SMAs) are conventionally considered as actuator materials. Among these materials, SMAs exhibit strains of ~10% which is two orders of magnitude higher than the magnetostrictive materials and piezoelectric ceramics. They also offer high power density when compared with piezoelectric ceramics and magnetostrictive materials.

Stress and operating temperature are critical parameters for SMAs to induce high strain and power density. Below martensite start temperature (M_s), a small magnitude of stress can create large strain that can be explained by the easy rearrangement of martensite variants under stress loading. After unloading, heating the SMA above the austenite finish temperature (A_f) allows the deformed SMA to recover its original shape. This phenomenon is called the shape memory effect (SME). Previous investigations about the SMAs have been focused on the SMAs

exhibiting large displacements which allow these alloys to be used in applications like actuators, electrical connectors and biomedical instruments. The SME involves a diffusionless martensitic transformation which can be reversibly transformed from the low-temperature martensitic phase to the high-temperature austenitic phase. Certain alloys, like Ni-Ti, Cu-Zn-Al and Cu-Ni-Al have the ability to maintain their original shape on the application of a sufficient temperature change.

Ferromagnetic shape memory alloys (FSMAs) are a novel class of SMAs which combine the properties of ferromagnetism with the reversible martensitic transformation. A comparison between SMAs and FSMAs is given in Table 3.1.The conventional shape memory alloys (SMAs) have a relatively slow response time when compared to FSMAs. This is due to the temperature controlled activation mechanism in SMAs. Different from the conventional SMAs, the thermoelastic martensitic transformation can be induced by an external magnetic field in FSMAs [46-49]. Ni_2MnGa and its off-stoichiometric derivatives is the prototype of FSMAs [50-64], Other FSMAs such as Ni-Mn-Al [1, 65, 66], Fe-Pd [67-69], Co-Ni-Al [70-72] and Co-Ni-Ga [73, 74] are of increasing interest as well. These smart materials have attracted attention of the scientific community due their probable application as human implants. Attempts have been made to improve the physical and mechanical properties of implants. Ni-Mn-Ga FSMAs alloys have a potential for biomedical applications [75]. As shown in Figure 3.1 there is a growing interest in FSMAs due to the possibility of inducing the shape memory effect with an externally applied magnetic field. The term ‘‘ferromagnetic shape memory effect’’ is used to indicate the reversible shape change is caused by either rearranging the martensite variants or inducing the austenite/martensite transformation with the application of an external field.

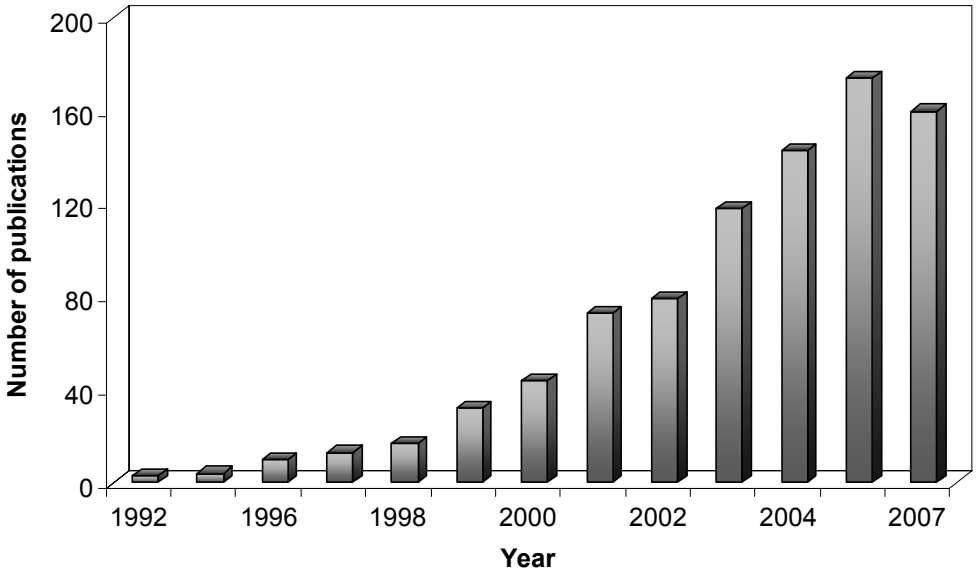

Figure 3.1 Number of publications related to FSME published between 1992 and 2007 (numbers were taken from the ISI database).

Table 3.1 Comparison of FSMAs and SMAs.

	Shape Memory Alloy (SMA)	**Ferromagnetic Shape Memory Alloy (FSMA)**
Prototype Material	Ni-Ti	Ni-Mn-Ga
Mechanism	Strain as a result of martensitic transformation and twin boundary motion	MFIS in martensitic phase due to twin boundary motion
Driving Force	Cooling and heating stress	Magnetic field or cooling and heating stress
Advantages & Disadvantages	Large strain (~10%) Slower response Poor energy conversion	Large Strain (~10%) Fast response, Contact free High energy conversion

FSMAs undergo a martensitic transformation from the high symmetry (cubic) phase to the low symmetry (tetragonal or orthorhombic) phase upon cooling. In the martensitic phase, to minimize the overall shape change and macroscopic strain energy of the sample, a special microstructure develops. Twinning occurs because generally there are several crystallographically equivalent ways to deform the high symmetry (cubic) structure. As a result, the deformation can take various directions in the FSMA. The structural domains with distinct boundaries are called twin variants. In the absence of an external magnetic field, the magnetization in ferromagnetic materials tends to align along definite crystallographic directions. The preferred axes are called the easy directions because it is easiest to magnetize a demagnetized sample to saturation if the external magnetic field is applied along the preferred direction. Both on the application of an external magnetic field along easy and hard directions lead to the saturation of magnetization but the latter necessitates application of larger external magnetic fields. If the easy axis is in the same direction with the twin direction, in a twinned microstructure similar to the lattice orientations the alignment directions of magnetic moments differ. A schematic illustration is given in Figure 3.2.b. In the presence of an external magnetic field, magnetic moments tend to align in the external field direction.

If the magnetic anisotropy energy, which is a measure of the energy required to change the direction of magnetic moments out of easy axis, is greater than the energy to move the twins it is favorable for the twins to move rather than the rotation of magnetization out of east direction. Percentage of twins in which the direction of easy axis is parallel to the external magnetic field will grow at the expanse of other twin variants as schematized in Figure 3.2.c. Magnetic field induced redistribution of the twin variants result in net shape changes in FMSM alloys.

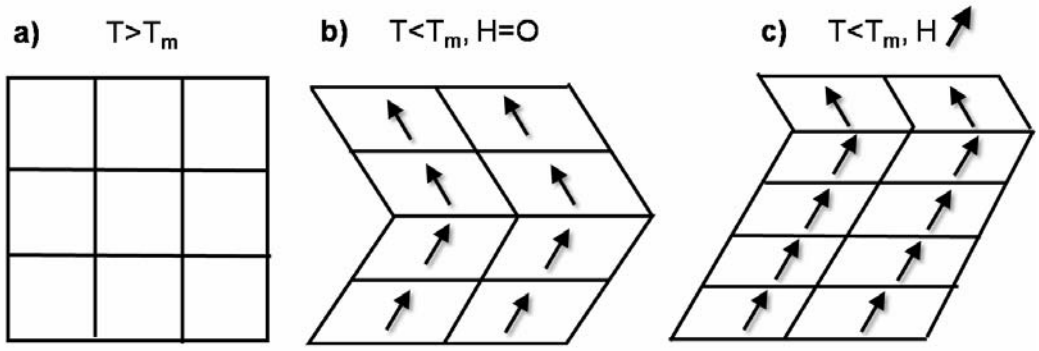

Figure 3.2 Phase transformation from the austenitic, (a), to the martensitic phase, (b), and rearrangement of twin variants under an external field, (c).

Based on the mechanism described above, the fundamental requirements for the occurrence of FSME in a material can be given as:

- The material should exhibit a thermoelastic martensitic transformation in the ferromagnetic state ($T_C > T_M$).

- Magnetic anisotropy energy should be higher than the energy needed for the twin boundary motion.

In practice, the FSMA should be in martensitic phase near the operation temperature and in order to obtain FSME in smaller magnetic fields, materials with high magnetic moments are desirable.

3.2 MARTENSITIC TRANSFORMATIONS

Heusler alloys undergo a relatively low temperature martensitic transformation. Similar martensitic transformations are known to occur in many metallic alloys but some Ni-based Heusler alloys are one of the rare materials that undergo this displacive, diffusionless solid state structural transformation in ferromagnetic state

(below Curie temperature, T_C). The nature of martensite remains of the greatest technological importance, but after a century of study fundamental physics still lacks explanation of this phenomenon. Typically, upon cooling, the high-temperature symmetric phase (austenite) transforms to a low-temperature structure with lower symmetry (martensite) through a first-order phase transition [76]. Martensitic transformation involves a cooperative rather than diffusive displacement of atoms. Sometimes, the martensitic transformation is called a *shear* or *displacive transformation*. The diffusionless character of the martensitic transformation suggests that martensite can form at very low temperatures, where diffusion is not imaginable over the time period of the experiment. The martensitic transformation is characterized by the austenite-start A_s, Austenite-finish A_f, martensite-start, M_s, and the martensite-final, M_f , temperatures. $T_M= (M_s+M_f)/2$ is sometimes used for simplicity.

During the martensitic transformation, atoms move only small distances relative to their neighbours, however the macroscopic effect is quite large. A passage of a slip dislocation through a crystal causes the formation of a step. A passage of many such dislocations on parallel slip planes causes macroscopic shear. Slip causes a change in shape but not a change in the crystal structure, because the Burgers vectors of the dislocations are also lattice vectors. In Figure 3.3, the schematic representations of the three variants that may occur below M_s are given. The easy axis of the martensite is the compression (short) axis. Therefore, the magnetizations shown in Figure 3.3 are in $\pm m_i$ directions.

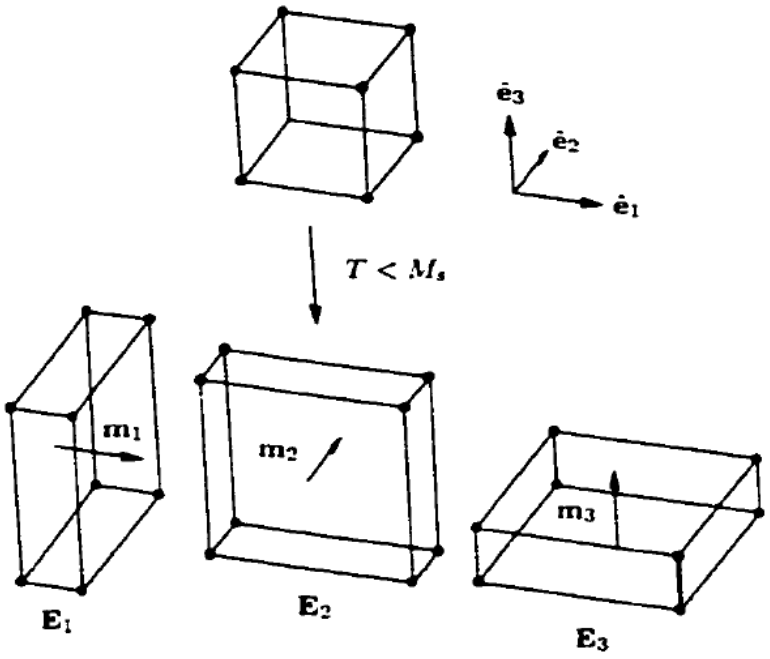

Figure 3.3 Tetragonal variant structures, cubic axis and associated magnetizations are denoted using E_i, e_i and M_i, respectively [54].

CHAPTER 4

HEUSLER ALLOYS

In 1903, German mining engineer and chemist Friedrich Heusler found that the addition of Al, Sn, Sb, Bi or In alloying elements to binary Cu-Mn makes this compound ferromagnetic although the constituting elements are paramagnetic, diamagnetic or antiferromagnetic [77]. Recently, Heusler alloys named after Friedrich Heusler have received considerable attention due to their unique properties like giant magnetocaloric effect (GMCE) and ferromagnetic shape memory effect (FSME).

4.1. THE HEUSLER ($L2_1$- TYPE) STRUCTURE

At present, two groups of alloys are called Heusler alloys: The semi-Heusler alloys represented by the formula ABC and the full Heusler alloys symbolized with the formula A_2BC. The completely ordered $L2_1$-type ordered crystal structure of A_2BC type full Heusler alloy is given in Figure 4.1. Unit cell of A_2BC consists of eight B2 (bcc) cells in which the corner lattice sites of α_1 and α_2 are occupied by A atoms and body centered lattice sites of β and γ are occupied by B and C atoms, respectively.

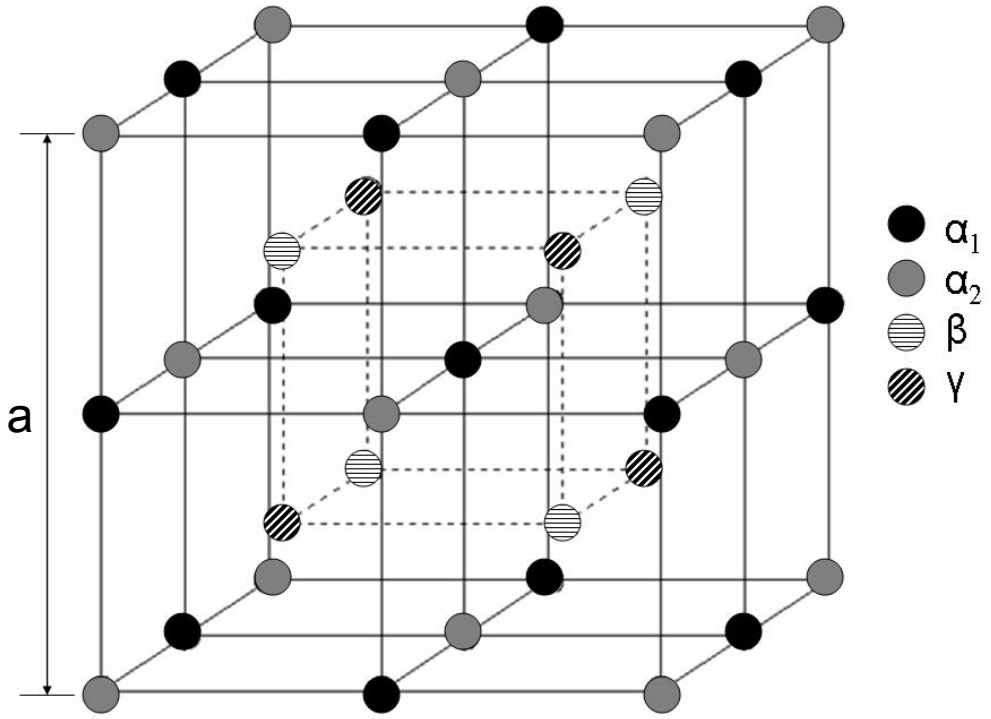

Figure 4.1 The unit cell of the $L2_1$-type ordered crystal structure.

A2, B2 and $L2_1$ phases have the same unit cell with different atomic distributions over α_1, α_2, β and γ lattice sites. The A2 phase forms at high temperatures upon solidification in which atoms are distributed randomly in the lattice sites of $L2_1$-type (space group: Fm3m) crystal structure. Chemical ordering can occur directly to completely ordered $L2_1$ phase or via intermediate partially ordered B2 phase, in which A atoms are distributed orderly over α_1 and α_2 lattice sites, while B and C atoms are distributed randomly over β and γ lattice sites.

A element is generally a transition metal, such as Co, Cu, Ni or Fe ; B element is typically Mn and C element can be Ge, Si, Ga, Sn, Sb, Al or In. If the elements A and C are non-magnetic, the magnetization is mainly confined to the Mn sublattice. When the element A is Ni or Co, an additional magnetization appears at the A

atomic site [78]. Main combinations of elements that form the Heusler structure are given in Figure 4.2.

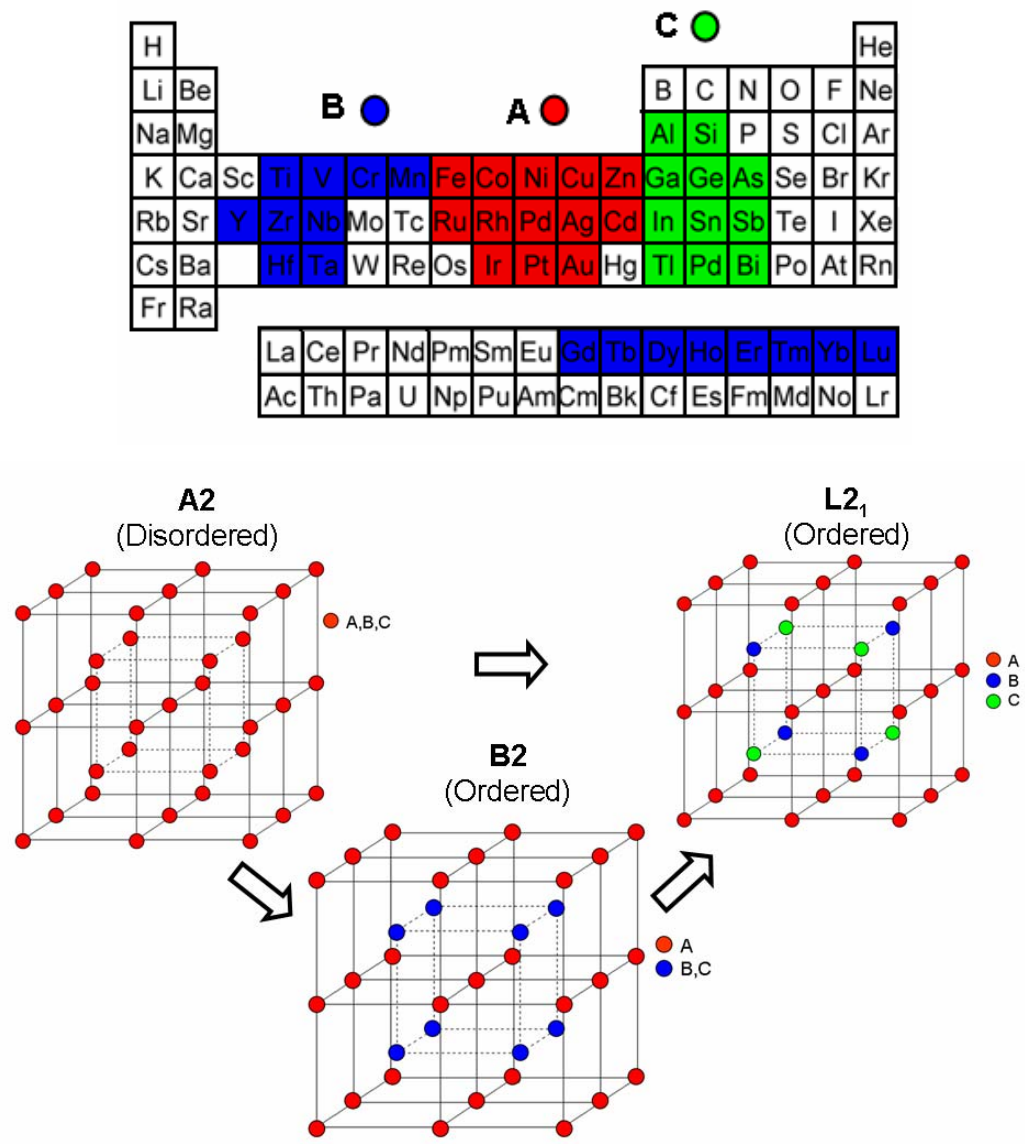

Figure 4.2 Main combinations of elements that form the Heusler ($L2_1$- type), B2 and A2 structures, data taken from [79].

4.2. Ni-Mn-Ga AND Ni-Mn-Al HEUSLER ALLOYS: EXPERIMENTAL BACKGROUND

In this section, the literature concerning the magnetic and structural properties of the Ni-Mn-Ga and Ni-Mn-Al full Heusler alloys are reviewed separately.

4.2.1. Ni-Mn-Ga Heusler Alloys

Stoichiometric Ni_2MnGa alloy undergoes a relatively low temperature martensitic transformation (T_M) at around 202 K, a magnetic transition (T_C) near 376 K, order-order and order-disorder transitions at 1071 K and 1382 K, respectively [16, 80]. Near stoichiometric Ni_2MnGa alloys have been investigated thoroughly in literature [13, 52, 54, 55, 59, 60, 81-87].

Upon cooling, a first order structural transformation occurs in Ni-Mn-Ga alloys from the cubic structure to a tetragonal [80] or orthorhombic [88, 89] structure. P. J. Webster et al. determined the crystal structure of the cubic parent phase of Ni_2MnGa alloy as the $L2_1$ structure [80]. $L2_1$ –type structure is shown in Figures 4.1 and 4.2. In the martensitic transformation, the unit cell of the cubic $L2_1$ –type structure contracts along one <100> axis and extends along the other two, as shown in Figure 3.3. It is important to note that the strains are exaggerated in this figure for clarity and the deformations are from the simple cubic cell not the $L2_1$-type Heusler structure. T_M of Ni-Mn-Ga alloys span over a wide range, from 160 K to 620 K [50, 60, 90, 91] and these temperatures are very sensitive to composition. For instance, 1-2 at. % change in composition can alter T_M by 50 K. Tuning of T_M is possible by changing the Ni:Mn:Ga ratios. It was well established that T_M increases with increasing e/a (electron concentration) [3]. e/a is calculated with the following equation for Ni-Mn-Ga alloys. Number of 3d+4s electrons for Ni, Mn and Ga are taken as 10, 7 and 3 respectively.

$$e/a = \frac{10\times(Ni\ at.\%) + 7\times(Mn\ at.\%) + 3\times(Ga\ at.\%)}{100} \qquad \textbf{(4.1)}$$

Neutron diffraction measurements for the Ni_2MnGa alloy have shown that in the $L2_1$-type structure magnetization is mainly confined to Mn sites. These moments were reported to be ~4 μ_B, whereas at Ni sites moments of ~0.3 μ_B were found [2]. Therefore, the ferromagnetic ordering below T_C in the Ni_2MnGa alloy can be mainly attributed to the Mn-Mn interactions. T_C is between 320 K and 380K for Ni-Mn-Ga alloys and unlike T_M, T_C decreases slightly with e/a [2, 3].

Combining the properties of the reversible martensitic and magnetic transitions gives Ni-Mn-Ga alloys unique magnetocaloric and FSM properties. The discovery of quite large MFIS in Ni-Mn-Ga Heusler alloys stimulated interest in FSMAs [46-49]. There is a significant interest in both the fundamental science behind the thermoelastic martensitic transformation in Heusler alloys and in potential applications of these smart materials. In Ni-Mn-Ga Heusler alloys for compositions where $T_m > T_C$, martensitic transformation occurs in ferromagnetic state. This receives great technological interest because designing new shape memory devices like sensors or actuators is possible by combining the magnetic properties of martensitic phase with the thermoeleastic martensitic transformation. Among all the investigated FSMA's largest MFIS was reported for the slightly off stoichiometric single crystal Ni-Mn-Ga [88]. The Ni-Mn-Ga Heusler alloys with non-modulated martensite have shown a MFIS of ~6 %, while for the alloys having orthorhombic martensite the MFIS values were reported to be ~10 % [51, 92, 93].

Besides the FSM properties, Ni-Mn-Ga Heusler alloys also gained interest as a candidate magnetic refrigerator material for the past years because these alloys exhibit GMCE. By compositional tuning of T_M and T_C of Ni-Mn-Ga alloys can be merged and as a result of this magneto-structural transition, GMCE was observed and large ΔS_M values which are comparable to the reported values for the $Gd_5(GeSi)_4$ alloys [23, 94] were observed in Ni-Mn-Ga alloys [7, 10].

Ni-rich (more than 1-2 at.%) Ni-Mn-Ga alloys did not attract attention due to their FSM properties because magnetic field induced twin boundary motion is hindered by the large twinning stress [84, 95, 96]. However Ni-rich Ni-Mn-Ga alloys received attention due to their unique combination of ferromagnetism and a structural transition. Coupled magnetic and structural (magneto-structural) transitions were observed in these alloys. As shown in Figure 4.3, T_C decreases slightly whereas T_M increases with increasing excess Ni (x) and these temperatures merge for $18<x<27$ [2, 97]. This attractive but unexplained property was reported for other FSM systems like Co-Ni-(Al and Ga) [98, 99] and Ni-Fe-Ga [100, 101]. The coupling of T_m and T_C in Ni-Mn-Ga alloys occur in different regions of the phase diagram for the substitution of Ni for Mn in $Ni_{2+x}Mn_{1-x}Ga$ ($0.18<x<0.27$) [2], for the substitution of Mn for Ga in $Ni_2Mn_{1+x}Ga_{1-x}$ [8] and for the substitution of Ni for Ga in $Ni_{2+x}MnGa_{1-x}$ [102] alloys.

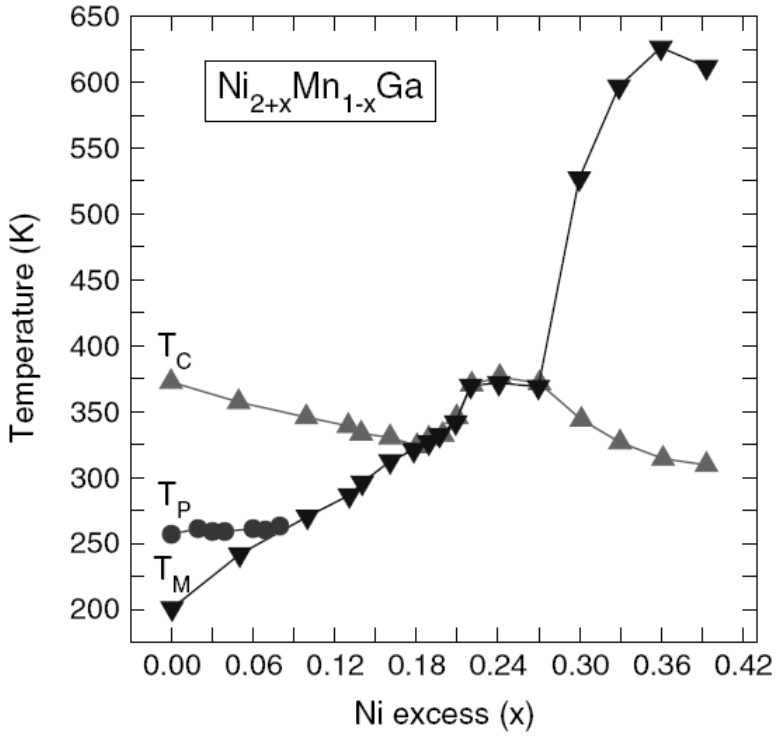

Figure 4.3 T_C, T_M and premartensitic transition temperatures, T_P, as a function of the excess Ni concentration, x, in $Ni_{2+x}Mn_{1-x}Ga$ alloys [97].

The increase in the T_M in Ni-Mn-Ga alloys can be attributed to the increase in e/a. The empirical dependence of e/a and T_m is valid for a large composition interval. Since the Mn atoms have a magnetic moment of ~4μ_B [80] the decrease in T_C in $Ni_{2+x}Mn_{1-x}Ga$ can be due to the dilution of the magnetic subsystem. But for the Mn-rich $Ni_2Mn_{1+x}Ga_{1-x}$ alloys, the decrease of T_C can be attributed to the more pronounced antiferromagnetic interactions between the Mn atoms.

The ability to control structural and magnetic phase transitions in Ni-Mn-Ga alloys with adjusting e/a, allows to study MCE at magnetic and structural phase transitions occurring at different temperatures for various compositions. The maximum ΔS_M value of 5 $JK^{-1}Kg^{-1}$ was obtained by changing the external magnetic field (without magneto-structural phase transition) in Ni-Mn-Ga alloys [5, 94, 103]. But a quite

large ΔS_M value of 20 $JK^{-1}Kg^{-1}$ at a relatively small magnetic change (ΔH=16 kOe) was obtained at the temperature where a magneto-structural transition occurs [10].

The magnitude of MCE observed in Ni-Mn-Ga Heusler alloys is greater than the other candidate magnetic refrigerant materials: Gd, $La(Fe_{13-x}Si_x)H_y$ and $Gd_x(Si_{1-x}Ge_x)_4$ alloys near RT. Only $Mn(As_{1-x}Sb_x)$ alloy exhibits greater $|\Delta S_M|$ values near RT. $Ni_{50+x}Mn_{25-x}Ga_{25}$ alloy together with the $La(Fe_{13-x}Si_x)H_y$, $Gd_x(Si_{1-x}Ge_x)_4$, $Mn(As_{1-x}Sb_x)$ alloys show first order magnetic (magneto-structural) phase transitions. On the other hand the prototype magnetic refrigerant material Gd undergoes a second order magnetic transition. There are several advantages of Ni-Mn-Ga Heusler alloys over other candidate magnetic refrigerants. Ni-Mn-Ga Heusler alloys do not contain expensive rare earth materials like Gd and La or toxic elements like As or P.

4.2.2.Ni-Mn-Al Heusler Alloys

The Ni-Mn-Ga Heusler alloys received great attention due to extraordinary properties like FSME and MCE as discussed in the previous part. One of the potential alternatives to these alloys, the Ni-Mn-Al Heusler alloys, became a focus of research in the last decades.

Ternary Ni-Mn-Al alloys were firstly studied as an alloying addition of Mn to binary Ni-Al alloys to improve the high temperature shape memory properties of relatively brittle binary Ni-Al alloys. K. Ishida et al. reported that addition of Mn alloying element together with Fe, Co and Cr elements results in an increase in ductility of binary Ni-Al alloys [104].

At RT, both Ni_2MnAl and Ni_2MnGa Heusler alloys have the $L2_1$ -type crystal structure with similar lattice parameters but these alloys have different atomic ordering characteristics. Both Ni-Mn-Ga and Ni-Mn-Al alloys undergo $B2 \leftrightarrow L2_1$ order-order phase transitions upon cooling [16, 105]. In the B2 phase, Ni atoms are

distributed orderly at the corner lattice sites while in the $L2_1$ phase, a further ordering occurs at the body centered sites in the Mn-Ga and Mn-Al sublattices for the Ni-Mn-Ga and Ni-Mn-Al alloys (Figures 4.1 and 4.2). Ni-Mn-Ga alloys have high $B2 \leftrightarrow L2_1$ transition temperatures (~1100 K) when compared to the Ni-Mn-Al alloys which have relatively low $B2 \leftrightarrow L2_1$ transition temperatures (~660 K). Annealing of the Ni-Mn-Ga alloys around the relatively higher $B2 \leftrightarrow L2_1$ transition temperatures (~1100 K) allow the stabilization of a single $L2_1$ phase. Conversely, stabilization of the fully ordered $L2_1$ phase in Ni-Mn-Al alloys necessitates long term aging at around the $B2 \leftrightarrow L2_1$ transition temperature (~660 K). This is mainly attributable to the slower diffusion kinetics at 660 K. In the previous studies concerning the stabilization of $L2_1$ phase in Ni-Mn-Al alloys, a mixture of $L2_1$ and B2 phases were obtained, although $L2_1$ is the thermodynamically stable phase [65, 105].

Another similarity between the Ni-Mn-Al and Ni-Mn-Ga alloys revealed by the investigations of R. Kainuma et al. and S. Morito et al. is the martensitic transitions. It was reported that martensitic transformations taking place between 239 K and 873 K in Ni-Mn-Al alloys are sensitive to composition and they are analogous to the ones observed in Ni-Mn-Ga alloys. For the low Al and Mn concentration, 2M ($L1_0$) phase forms and for the higher Al and Mn concentration 10M, 14M, 12M phases form [106, 107].

R. Kainuma et al. studied the martensitic transitions that occur in Ni-Mn-Al alloys quenched from elevated temperatures over 1273 K. R. Kainuma et al. reported the formation of 2M ($L1_0$), 10M, 14M and 12M martensitic structures from the parent B2 phase [106]. The M_s, M_f , A_s and A_f temperatures of Ni-Mn-Al alloys determined from DSC curves are given in Table 4.1 [106]. M_s' and A_f' denote temperatures of additional transitions observed in DSC curves [106]. It is important to note that the binary $Ni_{50}Mn_{50}$ alloy has a high martensitic transition temperature (M_s=947 K) and this temperature decreases drastically with the substitution of Al

for Mn in $Ni_{50}Mn_{50-x}Al_x$ alloys. For the substitution of Al for Mn by 20 at. % (x=20), M_s decreases from 947 K to 251 K [106].

Table 4.1 M_s, M_f, A_s, A_f, M_s' and A_f' data of Ni-Mn-Al alloys [106].

Transformation Temperatures (K)						
Alloy	M_s	M_f	A_s	A_f	M_s'	A_f'
$Ni_{50}Mn_{50}$	947	933	980	992	—	—
$Ni_{50}Mn_{46}Al_4$	862	840	866	881	—	—
$Ni_{50}Mn_{42}A_8$	746	732	758	776	810	834
$Ni_{50}Mn_{38}Al_{12}$	614	558	577	641	647	685
$Ni_{50}Mn_{34}Al_{16}$	464	401	407	465	513	538
$Ni_{50}Mn_{30}Al_{20}$	251	239	261	297	292	295
$Ni_{44}Mn_{46}Al_{10}$	541	532	621	635	—	—
$Ni_{45}Mn_{40}Al_{15}$	389	354	367	392	—	—
$Ni_{55}Mn_{30}Al_{15}$	659	651	706	722	—	—
$Ni_{55}Mn_{25}Al_{20}$	461	434	459	472	—	—
$Ni_{60}Mn_{15}Al_{25}$	508	506	704	717	—	—

K. Ishida et al. and R. Kainuma et al. reported that increasing the amount of the $L2_1$ phase in a B2+$L2_1$ phase mixture results in the stabilization of cubic structure which leads to a decrease in martensitic transition temperature [104, 108]. Even for some Ni-Mn-Al alloys which undergo martensitic transitions in B2 phase, the stabilization of the fully ordered $L2_1$ phase results in the disappearance of the martnesitic transition [107]. On the other hand, A. Fujita et al. reported the occurrence of martensitic transition in off-stoichiometric Ni-Mn-Al alloys aged for

25 days at 673 K [109]. Y. Sutou et al. reported that for some compositions, the martensitic transformation occurs in alloys having a $L2_1$ phase but M_s decreases about 20 K as a result of low temperature aging [105].

Besides the similar crystal structures and martensitic transitions of Ni-Mn-Al and Ni-Mn-Ga alloys, another resemblance turns out as both alloys have martensitic and magnetic phase transformation temperatures depending similarly on valence-electron-per-atom or electron-to-atom ratio (e/a) [3, 66, 110]. e/a also controls the high temperature order-order transitions in A_2BC-type Heusler alloys, as studied comprehensively in the theoretical part of the study.

The number of outermost electrons for Ni, Mn and Al are assumed to be 10, 7 and 3, respectively. e/a for Ni-Mn-Al alloys is calculated by

$$e/a = \frac{10\times(Ni\ at.\%) + 7\times(Mn\ at.\%) + 3\times(Al\ at.\%)}{100} \qquad \textbf{(4.2)}$$

For Ni-Mn-Ga and Ni-Mn-Al alloys M_s and T_C can be expressed as as function of e/a. The reported values of M_s and T_C for Ni-Mn-Al [110] and Ni-Mn-Ga [3] alloys are shown in Figure 4.4.

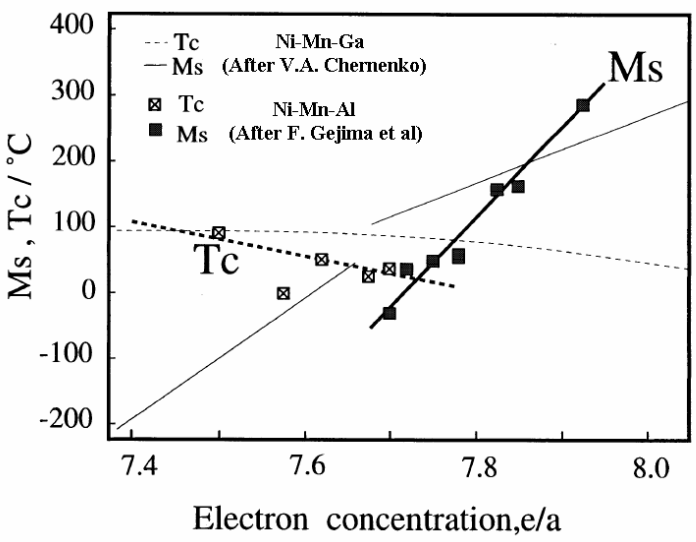

Figure 4.4 M_s and T_c versus e/a, reproduced after [110].

As can be clearly seen from Figure 4.4, for both Ni-Mn-Al and Ni-Mn-Ga alloys M_s decreases with decreasing e/a. But the decrease in Ni-Mn-Al alloys is greater than the decrease in Ni-Mn-Ga alloys. As a result of this, unlike Ni_2MnGa alloy (e/a=7.5) which exhibits a martensitic transformation at around 203 K, martensitic transition is not observed in stoichiometric Ni_2MnAl alloy (e/a=7.5). Martensitic transitions occur in off-stoichiometric Ni-Mn-Al alloys [110].

Similar to Ni-Mn-Ga Heusler alloys, the magnetic moment is mainly located at the Mn sites (~$4\mu_B$) in Ni-Mn-Al Heusler alloys. Magnetic moment of Ni is small and the magnetic moment of Al is almost negligible. However Ni atoms contribute to the ferromagnetism in Ni-Mn-Al alloys that can be explained by examining the density of states of Ni-Mn-Al alloys. Ni states are nearly equally distributed in spin up and spin down parts, whereas Mn states are generally located in the spin up part.

In Ni-Mn-Al alloys, the Mn-Mn distance governs the magnetic state of these alloys. In the fully ordered $L2_1$ phase Mn-Mn interatomic distance is 0.7a, while in the B2 and A2 phases this distance is 0.5a. The fully ordered $L2_1$ phase in Ni-Mn-Al Heusler alloys was reported to be ferromagnetic [65, 66, 110, 111] whereas

antiferromagnetism is ascribed to the partially ordered B2 phase [112]. The ground state of the Ni-Mn-Al Heusler alloys is ferromagnetic in a wide composition range [113].

Magnetic properties of aged Ni-Mn-Al alloys were investigated in a few studies. In 1999, F. Gejima et al. reported T_C values for the aged $Ni_{50}Mn_{50-x}Al_x$ (x=25, 22, 20) alloys in a very brief communication [110]. However, these T_C values were determined indirectly from calorimetric measurements and magnetization measurements are necessary to ensure the validity of these results. These T_C values for Ni-Mn-Al alloys are shown in Figure 4.4 as a function of e/a. It is seen from Figure 4.4 that there is a more noticeable decrease in T_C with increasing e/a for the Ni-Mn-Al alloys when compared to Ni-Mn-Ga alloys.

M. Acet et al. reported that M-H curves for the Ni_2MnAl alloy having the $L2_1$ phase have significant curvature. However, Ni_2MnAl alloy in the B2 phase has linear M-H curves [65]. The curvature observed in M-H curves for the Ni_2MnAl alloy having the $L2_1$ phase was claimed to be an indication of the ferromagnetism in this alloy. Temperature dependence of susceptibility for the Ni_2MnAl alloy having the $L2_1$ phase exhibits a ferromagnetic-like behaviour in contrast to the Ni_2MnAl alloy having the B2 phase which exhibits a typical antiferromagnetic-paramagnetic transition [65]. But M. Acet et al. stated that low temperature aging for 30 days was inable to stablize a pure $L2_1$ phase due to the unsaturation of magnetization in external magnetic fields as high as 50 kOe [65]. M. Acet et al. reported important evidence for the ferromagnetic nature of the $L2_1$ phase in the Ni-Mn-Al alloys but the reported data is restricted for the stoichiometric Ni_2MnAl alloy. In order to determine a relationship between atomic and magnetic ordering in Ni-Mn-Al system, off-stoichiometric Ni-Mn-Al alloys should also be investigated.

The low temperature aged (around 660 K) Ni_2MnAl alloys were obtained as a mixture of B2 and $L2_1$ phases and the magnetic state incorporates ferromagnetic

and antiferromagnetic parts with close Curie (T_C=273 K) and Neel (T_N=295 K) temperatures [65, 112].

In 2000, A. Fujita et al. reported the ferromagnetic shape memory (FSM) properties of the $Ni_{53}Mn_{25}Al_{22}$ alloy. The polycrystalline $Ni_{53}Mn_{25}Al_{22}$ alloy was reported to undergo a martensitic transition in the ferromagnetic state. Under an external magnetic field of 70 kOe and just below the M_f, a maximum relative length change of -100 ppm was reported [109]. In addition to that, for a single crystal cut from the polycrystalline specimen a maximum relative length change value which is ten times greater than the value reported for the polycrystalline sample was observed [109].

It is reasonable to suspect that the same mechanism which is responsible for the explanation of the observed ferromagnetic shape memory effect (FSME) in Ni-Mn-Ga alloys can be employed to describe the large magnetic field induced strains (MFIS) in Ni-Mn-Al alloy based on the fact that both Ni-Mn-Al and Ni-Mn-Ga alloys exhibit martensitic transitions in the ferromagnetic state. In the Ni-Mn-Ga system quite large MFIS were observed as a result of the rearrangement of twin variants under an applied magnetic field [47].

When compared to the MFIS reported for the Ni-Mn-Ga system (~10%), the MFIS value reported for the Ni-Mn-Al system (~0.17%) [109] seems quite small. This can be attributed to the fact that a single ferromagnetic ($L2_1$) phase could not be obtained in Ni-Mn-Al alloys under normal heat treatment conditions. The previously investigated Ni-Mn-Al Heusler alloys were obtained as a mixture of antiferromagnetic (B2) and ferromagnetic ($L2_1$) phases.

Furthermore, unllike the Ni-Mn-Ga system which is extensively studied for magnetocaloric properties, there are no studies concerning the MCE in Ni-Mn-Al Heusler alloys in literature.

4.3. ATOMIC ORDERING PROCESSES IN FULL HEUSLER ALLOYS

Ordered structures occur commonly in solid solutions and show remarkable physical, mechanical, electrical and magnetic properties. To clarify these interesting properties continuous theoretical and experimental investigations have been conducted on the atomic ordering processes in alloys for the last decades.

Intermetallic phases are formed from two or more elements, they have ordered structures and exhibit unique properties that differ from the constituent elements. Intermetallics captured attention for the development of materials for specific applications (e.g. materials that exhibit shape memory effect). Designing intermetallic compounds with desired properties necessitates the quantitative explanations of the changes in their properties. Besides, materials for practical applications are rarely binary systems. The theoretical treatments on the superlattice formations in binary alloys have been well established but the theoretical considerations on ternary alloys have been limited. This can be attributed to the requirement of much more complicated treatments for the ternary alloys. Consequently, treatments of multicomponent systems are of great importance. Firstly, the type of ordered structure and the effect of temperature and composition on atomic ordering processes must be clarified in order to improve the properties of alloys.

In order to characterize the order-order ($L2_1 \leftrightarrow B2$) and order-disorder ($B2 \leftrightarrow A2$) transitions in A_2BC type full Heusler alloys, relatively simple analytical calculations based on the Bragg-Williams-Gorski (BWG) approximation can be employed. The Bragg-Williams approximation was developed by W. L. Bragg and F.R.S. Williams in 1934 with the intention to model order-disorder transitions in binary alloys [114]. Unlike W. L. Bragg and F.R.S. Williams who considered only the interactions between nearest neighbor atoms, V.V. Geichenko and G. Inden took into account the interactions between next-nearest neighbor atoms, allowing to model the multiple ordering processes like $DO_3 \leftrightarrow B2 \leftrightarrow A2$ phase transformations in

Fe_3Al [115]. With this final adjustment to Bragg-Williams model, the BWG approximation which considers both the nearest and next-nearest neighbor interactions was established.

The BWG approximation has been employed in various investigations for the characterization of atomic ordering processes in alloys. T. Hirone and S. Matsuda investigated the third alloying element addition on ordering in B2 type structure [116]. S. Matsuda investigated superlattice formation by considering the interactions between first and second nearest neighbor atoms in the stoichiometric Cu_2MnAl alloy. S. Matsuda defined four order parameters to characterize the order-order ($L2_1 \leftrightarrow B2$) and order-disorder ($B2 \leftrightarrow A2$) transition of atomic species A, B and C at non-equivalent sublattices. V. P. Fadin et al. expanded the model to off-stoichiometric compositions but the interactions taken into account were confined to interactions between the nearest neighbor atoms [117]. Y. Murakami et al. developed a superlattice formation model that considers both the interactions between the nearest and next nearest neighbor atoms in order to describe the double ordering in A_2BC-type Heusler alloys having arbitrary compositions in β phase region [14]. In the study of Y. Murakami et al., calculated values of $L2_1 \leftrightarrow B2$ and $B2 \leftrightarrow A2$ transition temperatures were compared with experimentally determined temperatures for the β phase Au-Cu-Zn and Ag-Cu-Zn alloys. However, Y. Murakami et al. used predicted values of ordering energies that showed the best agreement with the experimental data. In 1997, R. Kainuma et al. reported a model based on the BWG approximation to analyze the $L2_1 \leftrightarrow B2$ transition temperatures in Ni-Al-Ti-Fe system [21]. Similar to the model of Y. Murakami et al., the model of R. Kainuma et al. considered the interactions between the nearest and next nearest neigbour atoms and both models are valid in the β phase region. The details of determination of the $L2_1 \leftrightarrow B2$ and $B2 \leftrightarrow A2$ phase transitions according to the models of Y. Murakami et al. [14] and R. Kainuma [21] will be discussed in the next section. R. Kainuma et al. estimated the values of ordering energies and calculated the $L2_1 \leftrightarrow B2$ transition temperatures according to these values. In the study of R. Kainuma et al., the predicted parabolic curve representing the $L2_1 \leftrightarrow B2$

transition temperatures were compared against the experimentally determined values of these temperatures by thermal analysis for the NiAl-Ni_2AlTi pseudobinary system [21]. Model of R. Kainuma et al. [21] was also employed in the investigation of ordering and phase separation in Co-Al-Ti ternary system [18]. K. Ishikawa et al. showed that the experimentally established $L2_1 \leftrightarrow B2$ transition temperature data for the CoAl-Co-Ti pseudobinary system can be fitted with a parabolic curve evaluated by the model of R. Kainuma et al. [21]. In another investigation, the ordering energies between the Al and Ti atoms for the second coordination sphere were approximated for the A-Al-Ti (A= Ti, V, Cr, Mn, Fe, Co, Ni and Cu) ternary systems. It was reported that the predicted values of ordering energies increases linearly with the increase in the electron concentration at the A site [17].

4.3.1. Calculation of the B2↔A2 and $L2_1$↔B2 Critical Transformation Temperatures in $A_{50}B_{50-x}C_x$ Full Heusler Alloys

Y. Murakami et al. [14] constructed the thermodynamical model, involving the B2↔A2 and $L2_1 \leftrightarrow B2$ transformations by including both the interactions between nearest and next nearest neighbour atoms for bcc alloys near the β phase region. Long range order (LRO) parameters of η_1, η_2 and η_3 proposed by Murakami et al. [14] were defined as;

$$\eta_1 = 2 \cdot (P_A^{\alpha} - x_A) \tag{4.3}$$

$$\eta_2 = \frac{4 \cdot (P_B^{\beta} - x_B)}{3} \tag{4.4}$$

$$\eta_3 = \frac{4 \cdot (P_C^{\gamma} - x_C)}{3} \tag{4.5}$$

Where P_A^α , P_B^β and P_C^γ are the probabilities of finding A, B and C atoms in α, β and γ lattice sites respectively. It is worth to note that in the treatment given in [14] $\alpha_1+\alpha_2 =\alpha$ was used because atomic fraction of A element atoms is close to 1/2 in order to avoid the occurrence of the $D0_3$ structure and allow only B2 and $L2_1$ structures in $A_{50}B_{50-x}C_x$ alloys. Atomic fractions of A, B and C atoms are represented as x_A, x_B and x_C respectively.

Perfect order can be attained for only the stoichiometric A_2BC alloys and by the use of LRO parameters defined above, ordering of atoms in $L2_1$, B2, and A2-type lattices can be represented as:

i. Since in a perfectly ordered $L2_1$ lattice, all A, B and C atoms should be at their original lattice sites ($P_A^\alpha = P_B^\beta = P_C^\gamma = 1$) then,

$$\eta_1 = \eta_2 = \eta_3 = 1 \qquad \textbf{(4.6)}$$

ii. Considering perfectly ordered B2 lattice where all the A atoms occupy their original lattice site of α ($P_A^\alpha = 1$) and B and C atoms occupy their lattice sites of β and γ with an equal probability ($P_B^\beta = P_C^\gamma = 1/2$), it is evident that,

$$\eta_1 = 1 \text{ and } \eta_2 = \eta_3 = 1/3 \qquad \textbf{(4.7)}$$

iii. For the A2 lattice there is a random distribution of A, B and C atoms over α, β and γ lattice sites and completely disordered state can be given by;

$$\eta_1 = \eta_2 = \eta_3 = 0 \qquad \textbf{(4.8)}$$

Moreover, the free energy of A_2BC alloy system is given by [14]

$$F = E_1 + E_2 - T\Phi \tag{4.9}$$

Where E_1 and E_2 are the potential energies of the system taking into account interactions of atoms at the first and second coordination spheres, respectively, T is the temperature and Φ is the configurational entropy.

For the calculation of the B2↔A2 (Tc_1) and $L2_1$↔B2 (Tc_2) phase transformation temperatures following equations have been obtained by minimizing free energy of system with respect to η_1 and η_2 LRO parameters [14],

$$\begin{aligned} Tc_1 = \frac{8}{k}\cdot\Big\{&\Big(x_A\cdot x_B\cdot W^{AB}(R_1)+x_A\cdot x_C\cdot W^{AC}(R_1)+x_B\cdot x_C\cdot W^{BC}(R_1)\Big)^2 \\ &+\Big[\Big(x_A\cdot x_B\cdot W^{AB}(R_1)+x_A\cdot x_C\cdot W^{AC}(R_1)+x_B\cdot x_C\cdot W^{BC}(R_1)\Big)^2 \\ &-x_A\cdot x_B\cdot x_C\Big(4\cdot W^{AC}(R_1)\cdot W^{BC}(R_1)-\Big(W^{AC}(R_1)-W^{AB}(R_1)+W^{BC}(R_1)\Big)^2\Big)\Big]^{1/2}\Big\} \end{aligned} \tag{4.10}$$

$$\begin{aligned} Tc_2 = &\frac{3\cdot W^{BC}(R_2)}{k} \\ &\cdot\frac{\Big[64\cdot x_B\cdot x_C(1-x_A)\cdot(1-x_A+\eta_1)+(5\cdot x_B-x_C)\cdot(5\cdot x_C-x_B)\cdot\eta_1^2\Big]}{8\cdot(1-x_A{}^2)\cdot(2-2\cdot x_A+\eta_1)} \end{aligned} \tag{4.11}$$

Here k is the Boltzmann's constant; $W^{AB}(R_1)$, $W^{AC}(R_1)$ and $W^{BC}(R_1)$ represent the partial ordering energies at the 1st coordination sphere for A-B, A-C, B-C atomic pairs, respectively while $W^{BC}(R_2)$ is the partial ordering energy at the 2nd coordination sphere for B-C atomic pair in A_2BC type alloy system.

The partial ordering energies between the atoms of suffixed letters for the l-th coordination sphere are given by

$$W^{AB}(R_l) = V^{AA}(R_l) + V^{BB}(R_l) - 2\cdot V^{AB}(R_l) \tag{4.12}$$

$$W^{AC}(R_l) = V^{AA}(R_l) + V^{CC}(R_l) - 2 \cdot V^{AC}(R_l) \quad \textbf{(4.13)}$$

$$W^{BC}(R_l) = V^{BB}(R_l) + V^{CC}(R_l) - 2 \cdot V^{BC}(R_l) \quad \textbf{(4.14)}$$

Where $V^{AB}(R_l)$, $V^{BC}(R_l)$, $V^{AC}(R_l)$, $V^{AA}(R_l)$, $V^{BB}(R_l)$ and $V^{CC}(R_l)$ denote the pairwise interaction energies between the atoms of suffixed letters for the l-th coordination sphere.

By taking into account criteria (i), Equation (4.6), for fully ordered $L2_1$-type superlattice (Figure 4.1), the $L2_1 \leftrightarrow B2$ transformation temperature of Tc_2 can be rewritten as

$$Tc_2 = \frac{3 \cdot W^{BC}(R_2)}{k} \cdot \frac{\left[64 \cdot x_B \cdot x_C \cdot (1 - x_A) \cdot (2 - x_A) + (5 \cdot x_B - x_C) \cdot (5 \cdot x_C - x_B)\right]}{8 \cdot (1 - x_A^{\,2}) \cdot (3 - 2 \cdot x_A)} \quad \textbf{(4.15)}$$

Another BWG approximation employed in the investigation of phase separation between the B2 and $L2_1$ phases of A_2BC type structure was developed in [17, 18, 21, 118]. R. Kainuma et al. [21] proposed the following equation for the calculation of $L2_1 \leftrightarrow B2$ critical transformation temperature, Tc_2, for ternary alloys of $A_{X_A}B_{X_B}C_{X_C}$,

$$\begin{aligned} Tc_2 = \frac{3}{k} \cdot \Bigg\{ \Omega + \Bigg[\Omega^2 - \Bigg(& 4 \cdot W^{AC}(R_2) \cdot W^{BC}(R_2) - \\ & \left(W^{AC}(R_2) + W^{BC}(R_2) - W^{AB}(R_2) \right)^2 \Bigg) \\ \cdot \Big[4 \cdot W^{AC}(R_2) \cdot W^{BC}(R_2) - \left(W^{AC}(R_2) + W^{BC}(R_2) - W^{AB}(R_2) \right)^2 \Big] & \\ \cdot (x_A - \eta_1) \cdot (x_B - \eta_2) \cdot (x_C - \eta_3) \Big]^{1/2} \Bigg\} & \end{aligned} \quad \textbf{(4.16)}$$

Where

$$\Omega = (x_A - \eta_1)\cdot(x_B - \eta_2)\cdot W^{AB}(R_2) + (x_A - \eta_1)\cdot(x_C - \eta_3)\cdot W^{AC}(R_2) + (x_B - \eta_2)\cdot(x_C - \eta_3)\cdot W^{BC}(R_2) \quad \textbf{(4.17)}$$

η_i is the LRO parameter of the component i at the $L2_1 \leftrightarrow B2$ transformation temperature and was defined as [21]

$$\eta_i = \left(P_i^{\alpha_1} + P_i^{\alpha_2} - P_i^{\beta} - P_i^{\gamma}\right)/4 \quad \textbf{(4.18)}$$

P_i^L is the probability of an i atom to occupy the sublattice site of L (L ≡ α_1, α_2, β or γ). In the β phase region where x_A = 1/2; based on the assumption that all A atoms occupy their original α lattice sites (figure 1), i.e. $x_A = \eta_1$, $x_B = -\eta_2$ and $x_C = -\eta_3$, R. Kainuma et al. [21] obtained that,

$$Tc_2 = \frac{24}{k}\cdot W^{BC}(R_2)\cdot x_C\cdot(1/2 - x_C) \quad \textbf{(4.19)}$$

It is obvious that calculation of Tc_1 order-disorder and Tc_2 order-order phase transformation temperatures for these two approaches necessitate sign and magnitude of partial ordering energies between constituent element atoms at the first and second coordination spheres. Since the pair wise interatomic interaction potentials and/or partial ordering energies are constant parameters of theory in the statisco-thermodynamical approximations, it is impossible to determine the sign and magnitude of these parameters by using statistical methods. Therefore, electronic theory of binary and/or multicomponent alloys in different approximations should be employed for that purpose.

4.3.2. Calculation of Partial Ordering Energies for Ternary Alloys

The partial ordering energies, $W^{\alpha\beta}(R_l)$, of substitutional A-B-C alloys as a function of interatomic distance, R, can be calculated based on the electronic theory of

multicomponent alloys in the pseudopotential approximation by using the following equations [119-127]

$$W^{ij}(R_l) = \frac{\bar{\Omega}_0}{\pi^2} \cdot \int_0^{\infty} F^{ij}(q) \cdot \frac{SinqR_l}{qR_l} \cdot q^2 dq \qquad \textbf{(4.20)}$$

where

$$F^{ij}(q) = -\frac{\bar{\Omega}_0}{8\pi} \cdot \left|\omega_i^0(q) - \omega_j^0(q)\right|^2 \cdot q^2 \cdot \frac{\varepsilon(q)-1}{\varepsilon^*(q)}$$

$$+\frac{2\pi}{\bar{\Omega}_0 q^2} \cdot |Z_i^* - Z_j^*|^2 \cdot \exp\left(-\frac{q^2}{4\varphi}\right) \qquad \textbf{(4.21)}$$

$\bar{\Omega}_0$ is the is the average atomic volume of the ternary alloy, *ε(q)* is the dielectric constant in Hartree approximation; *ε*(q)* is the modified dielectric constant which takes into account the correlation and exchange effects [128]; $\omega_i^0(q)$ and $\omega_j^0(q)$ are the form factors of an unscreened pseudopotential of *i* and *j* component ions (i,j ≡A,B or C) respectively; $Z_i^*(Z_j^*)$ is the effective valency of the *i(j)* component atoms and φ is the Ewald parameter. Equations (4.20) and (4.21) enable one to calculate partial ordering energies as a function of interatomic distance, R, for any ternary alloy provided that the form factor of unscreened pseudopotentials, $\omega^0(q)$, and effective valences, *Z**, are known for the ions involved. Unlike simple metal alloys, the form factor of the pseudopotential for transition metals must contain terms responsible for the d-resonance effect. The model pseudopotential, employed in our calculations in which the d-resonance effect is partly taken into account for transition metals was developed by Animalu [129].

CHAPTER 5

EXPERIMENTAL PROCEDURE

This study was carried out in two parts, as mentioned previously. First part covers the modelling and simulation of relatively high temperature atomic ordering processes in full Heusler alloys and the second part involves experimental studies on atomic and magnetic ordering and magnetocaloric effect in these alloys. Theoretical and experimental investigations, as a whole, cover the atomic, magnetic and structural phase transitions that inevitably occur in a variety of A_2BC-type Heusler alloys.

In this chapter, the stages of the modelling and simulation of atomic ordering processes in Heusler alloys are presented. Furthermore, the various experimental techniques used in the experimental studies are given.

5.1. METHODS OF THEORETICAL MODELING AND SIMULATION OF ATOMIC ORDERING PROCESSES IN FULL HEUSLER ALLOYS

Figure 5.1 shows the stages of the theoretical studies. Firstly, the partial ordering energies between A-B, B-C and A-C pairs for the A_2BC-type Heusler alloys were calculated by means of the electronic theory of alloys in pseudopotential approximation by a computer program which was formulated based on Equations (4.20) and (4.21) by Prof. Dr. A. O. Mekhrabov.

Secondly, the ordering energies for the first two coordination spheres were used as input data for the superlattice formation models of R. Kainuma et al [21] and Y. Murakami et al. [14]. These models are presented in detail in the previous Chapter. It is important to note that, experimental lattice parameters from literature were

used to determine the radii of the coordination spheres to reach more accurate results. $L2_1 \leftrightarrow B2$ and $B2 \leftrightarrow A2$ phase transformations were calculated for A_2BC-type ordered $Ni_{50}Mn_{50-x}C_x$ (C=Ga, In and Sb) and $A_{50}B_{50-x}Ga_x$ (A=Fe, Ni, Co; B=Ni, Mn, Co, Fe) full Heusler alloys by using this method.

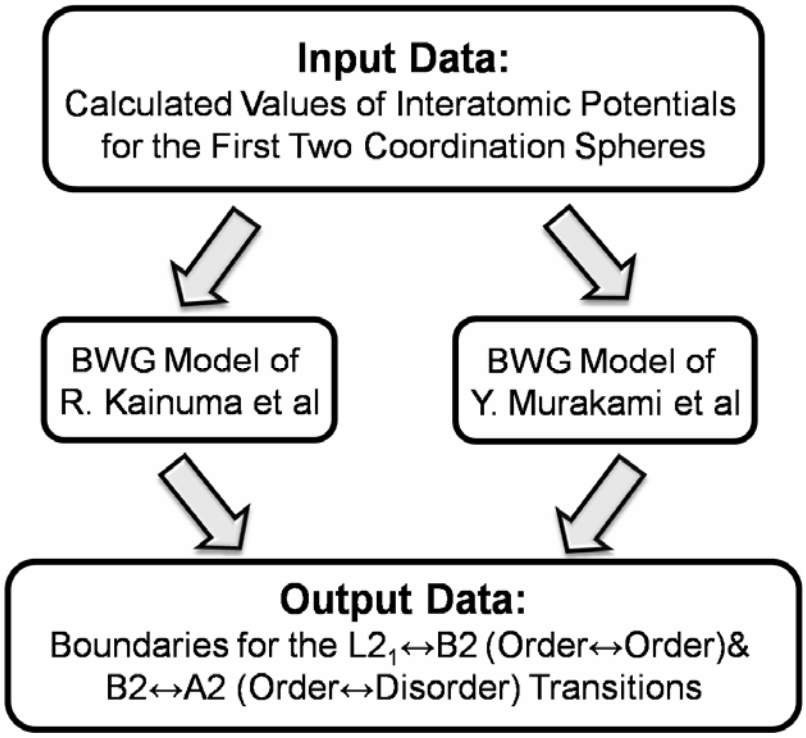

Figure 5.1 Stages of modeling and simulation of atomic ordering processes in full Heusler alloys.

5.2. METHODS OF EXPERIMENTAL INVESTIGATION OF ATOMIC AND MAGNETIC PROPERTIES OF FULL HEUSLER ALLOYS

The experimental investigations on the Ni-Mn-Al and Ni-Mn-Ga Heusler alloy systems involve sample preparation, heat treatment, RT X-ray diffraction (XRD) measurements and magnetization measurements as a function of temperature and external magnetic field.

In Table 5.1, compositions and e/a of the investigated Ni-Mn-Ga and Ni-Mn-Al alloys are presented. As discussed in Chapter 4, the T_M and T_C can be normalized with e/a in Heusler alloys. Therefore, the key parameter was e/a in determining the studied compositions.

For all of the produced alloys, the weight loss after the final melting was found to be minimal, thus, the targeted compositions were achieved in all the alloys under investigation. However, further confirmation was done by general EDS analyses, results of which are presented in Figures A.1-A.9, for each alloy.

Table 5.1. Nominal compositions and e/a values of produced Ni-Mn-Al and Ni-Mn-Ga alloys.

Alloy No	Composition	e/a
1	$Ni_{49}Mn_{25}Ga_{26}$	7.43
2	$Ni_{54}Mn_{20}Ga_{26}$	7.59
3	$Ni_{56}Mn_{18}Ga_{26}$	7.63
4	$Ni_{50}Mn_{50}$	8.49
5	$Ni_{50}Al_{50}$	6.48
6	$Ni_{50}Mn_{25}Al_{25}$	7.5
7	$Ni_{50}Mn_{20}Al_{30}$	7.29
8	$Ni_{50}Mn_{30}Al_{20}$	7.68
9	$Ni_{50}Mn_{40}Al_{10}$	8.08

5.2.1. Sample Preparation

Polycrystalline samples were prepared by conventional arc melting method in argon atmosphere. The method involves repeated melting of the elements in an argon atmosphere.

All the alloys were prepared from high purity (%99.99) starting elements Ni, Mn, Ga and Al. The constituent elements were weighed to obtain the desired composition. The mixture of elemental components was placed on a copper-hearth inside the arc melting chamber. Prior to each melting, the chamber was evacuated to 5×10^{-5} mbar and backfilled with argon gas for four times. Melting was done under a protective Argon atmosphere and alloys were melted turned over and remelted four times to ensure homogeneity. After the melting process, the alloys were cut into ~1.5 mm slices by using a linear precision saw. For the heat treatment, slices cut from ingots were put into quartz tubes filled with Argon gas and aged at 660 K for 12,24 and 48 days followed by furnace cooling.

5.2.2. Sample Characterization

X-ray Diffractometry

XRD measurements were conducted to determine the effects of composition and heat treatment on crystal structures and atomic ordering in the samples at RT. XRD was performed using a Rigaku diffractometer. CuK_{α} radiation was utilized in the diffraction angle (2θ) range of 20-100°.

Scanning Electron and Optical Microscopy

Scanning electron microscopy (SEM) studies were performed using a JSM-6400 Electron Microscope (JEOL) equipped with NORAN System 6 X-ray Microanalysis System & Semafore Digitizer. Energy dispersive spectroscopic analyses (EDS) were employed to determine the general compositions of alloys. Optical microscopy is employed in the investigation of the microstructure of the samples.

Magnetization Measurements

Magnetization measurements were conducted on ADE Magnetics Model EV9 Vibrating Sample Magnetometer (VSM) with an optional temperature controller. These measurements were performed as a function of temperature and magnetic field up to 2.2 kOe. Measurement of MCE is done by following these steps:

i. Determination and characterization of the phase transitions that occur in the sample by M-T measurements. M-T measurements were performed on both cooling and heating in order to determine the order of these transitions.

ii. Performing isothermal M-H measurements in the vicinity of the phase transition temperatures. Prior to each isothermal measurement the sample was heated above T_C to achieve demagnetization.

iii. Calculation of ΔS_M values by employing the M-H data in Equation (2.13)

CHAPTER 6

RESULTS AND DISCUSSIONS

This study was carried out under two main parts. First part covers the theoretical modelling of atomic ordering processes in full Heusler alloys. Second part involves both the experimental studies on the Ni-Mn-Ga alloy system which is known as the representative of the Heusler family and a potential candidate to this alloy system, Ni-Mn-Al Heusler alloys. In this chapter the results of these investigations will be presented and evaluated.

6.1. THEORETICAL INVESTIGATIONS ON MODELLING AND SIMULATION OF ATOMIC ORDERING PROCESSES IN FULL HEUSLER ALLOYS

Results and discussion of the theoretical studies consist of two parts. In the first part, calculated (order-order) $L2_1 \leftrightarrow B2$ and (order-disorder) $B2 \leftrightarrow A2$ critical phase transformation temperatures for the $Ni_{50}Mn_{50-x}C_x$ (C=Ga, In, Sb) alloys are given. The calculated transformation temperatures are compared against the previously reported experimental data. Furthermore, a relationship between the number of valence electrons at C atomic site and $L2_1 \leftrightarrow B2$ phase transformation temperatures is given.

In the second part, $L2_1 \leftrightarrow B2$ transformation temperatures, calculated for the $A_{50}B_{50-x}Ga_x$ (A=Fe, Ni, Co; B=Ni, Mn, Co, Fe) alloys are given. Besides, calculated values of $B2 \leftrightarrow L2_1$ phase transformation temperatures are compared against available experimental data from literature and the trends of these temperatures with electron concentration at the A and B atomic sites are given.

6.1.1. Calculated (order-order) $L2_1 \leftrightarrow B2$ and (order-disorder) $B2 \leftrightarrow A2$ Critical Phase Transformation Temperatures for the $Ni_{50}Mn_{50-x}C_x$ (C=Ga, In, Sb) Heusler Alloys

The calculated values of partial ordering energies were used as input data for the superlattice formation models of R. Kainuma et al. and Y. Murakami et al. The boundaries for the (order-order) $L2_1 \leftrightarrow B2$ and (order-disorder) $B2 \leftrightarrow A2$ transitions calculated for the $Ni_{50}Mn_{50-x}C_x$ (C=Ga, In, Sb) alloys are given in this part.

Partial ordering energies as a function of interatomic distance calculated by using the electronic theory of alloys in pseudopotential approximation are given in Figures 6.1-6.3 for A-B, A-C and B-C pairs in the stoichiometric Ni_2MnGa, Ni_2MnIn and Ni_2MnSb alloys respectively.

The calculated Radii for the first (R_1) and second (R_2) coordination spheres from experimental [79] lattice parameters (a) for Ni_2MnGa, Ni_2MnIn and Ni_2MnSb alloys are given in Table 6.1.

Table 6.1 a, R_1 and R_2 values of the $Ni_{50}Mn_{50-x}C_x$ (C=Ga, In, Sb) alloys.

Alloy	Ni_2MnGa	Ni_2MnIn	Ni_2MnSb
a (at.u.)	11.058	11.468	11.345
R_1 (at.u.)	4.788	4.966	4.913
R_2 (at.u.)	5.529	5.734	5.673

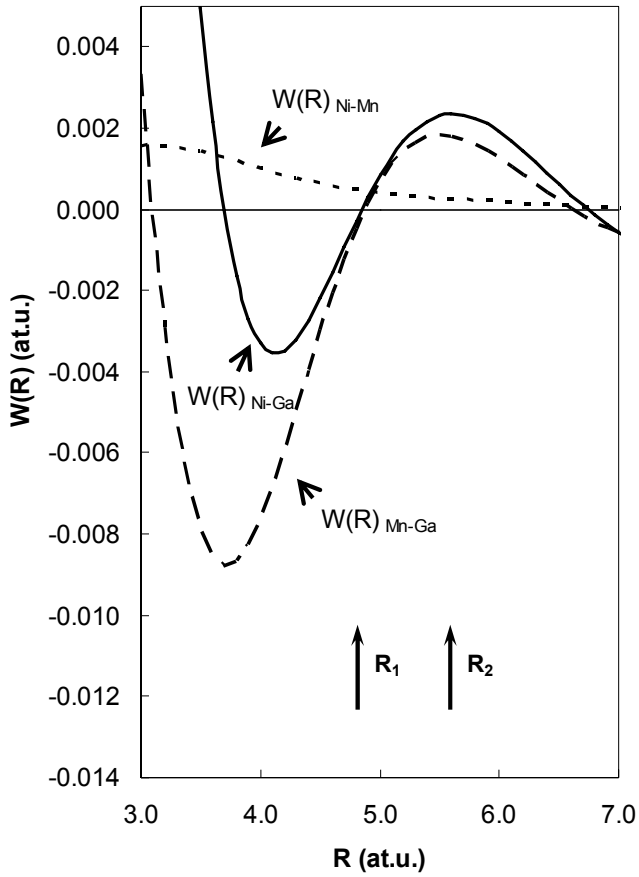

Figure 6.1 Variation of partial ordering energies for Ni-Mn (dotted line), Ni-Ga (solid line) and Mn-Ga (dashed line) pairs with interatomic distance, R, for the stoichiometric Ni_2MnGa alloy. (1 at. u.(energy) = 2 Ry = 27.2 eV; 1at. u.(length) = 0.529177 Å)

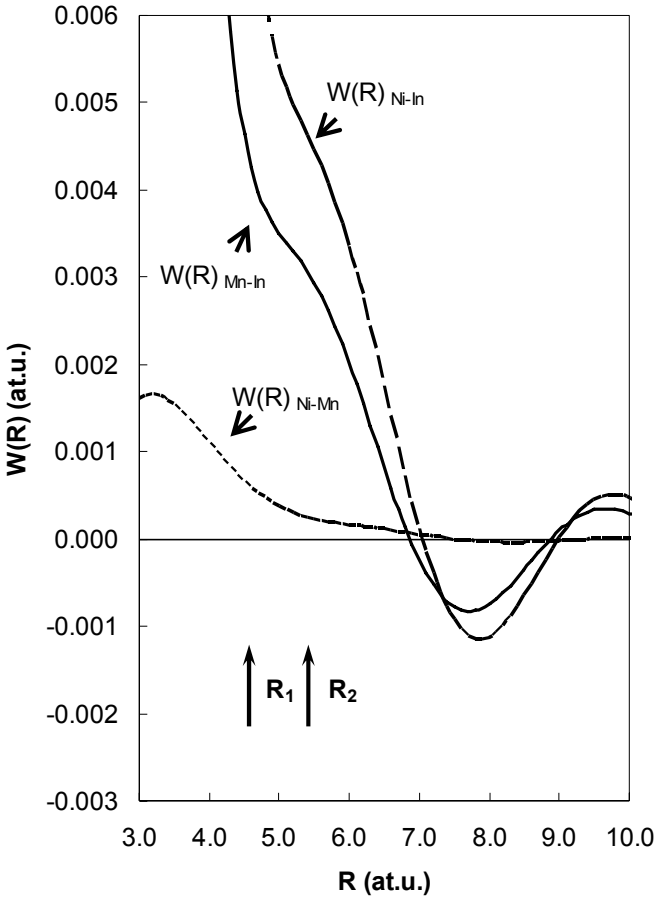

Figure 6.2 Variation of partial ordering energies for Ni-Mn (dotted line), Mn-In (solid line) and Ni-In (dashed line) pairs with interatomic distance for the stoichiometric Ni_2MnIn alloy. (1 at. u.(energy) = 2 Ry = 27.2 eV; 1at. u.(length) = 0.529177 Å)

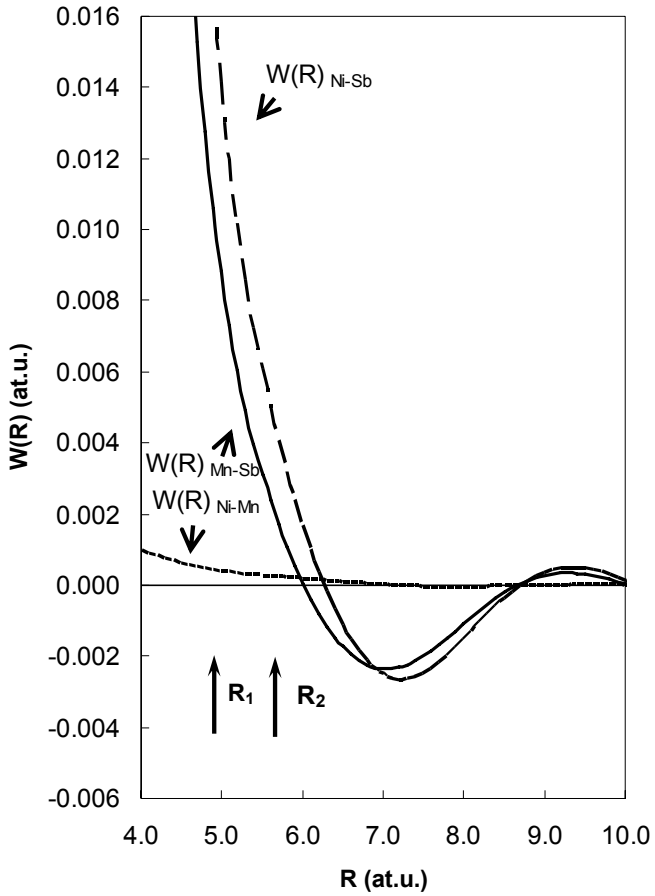

Figure 6.3 Variation of partial ordering energies for Ni-Mn (dotted line), Mn-Sb (solid line) and Ni-Sb (dashed line) pairs with interatomic distance for the stoichiometric Ni_2MnSb alloy. (1 at. u.(energy) = 2 Ry = 27.2 eV; 1at. u.(length) = 0.529177 Å)

It is evident from Figures 6.1-6.3 that the variation of partial ordering energies with interatomic distance have quasi-oscillatory and sign changing character, a well-known feature for metallic interactions. This suggests that the magnitudes of partial ordering energies may differ for different pairs (A-B, A-C and B-C), not only in terms of quantity but also in terms of sign.

6.1.1.1. $L2_1 \leftrightarrow B2$ (order-order) Phase Transformation for the $Ni_{50}Mn_{50-x}C_x$ (C=Ga, In, Sb) Heusler Alloys

Calculated magnitudes of the partial ordering energies for B-C atomic pairs at the second coordination sphere which governs $L2_1 \leftrightarrow B2$ order-order phase transformation in $Ni_{50}Mn_{50-x}Sb_x$, $Ni_{50}Mn_{50-x}Ga_x$ and $Ni_{50}Mn_{50-x}In_x$ alloys ($10<x<45$) are given in Table 6.2.

Table 6.2 Calculated partial ordering energies for B-C atomic pairs at the second coordination sphere for $Ni_{50}Mn_{50-x}C_x$ alloys where C=Ga, In, Sb in the composition range of $10<x<45$.

$Ni_{50}Mn_{50-x}C_x$ x (at. %)	Partial Ordering Energies ($x10^{-3}$) $W^{BC}(R_2)$ (at.u.)		
	C=Ga	C=In	C=Sb
10	1.910	2.847	1.715
15	1.881	2.751	1.776
20	1.853	2.653	1.832
25	1.827	2.554	1.882
30	1.802	2.456	1.929
35	1.778	2.361	1.971
40	1.756	2.268	2.010
45	1.733	2.180	2.046

It is obvious from the values presented in Table 6.2 that substituting Sb for Mn in $Ni_{50}Mn_{50-x}Sb_x$ alloy tends to increase in $W^{BC}(R_2)$ values. However, $W^{BC}(R_2)$ values decrease when Mn is substituted by Ga and In in $Ni_{50}Mn_{50-x}Ga_x$ and $Ni_{50}Mn_{50-x}In_x$ alloys respectively. As can be seen from Equations (4.15) and (4.19), the $L2_1 \leftrightarrow B2$ transformation temperature is directly proportional to the magnitude of the partial ordering energies for B-C atomic pairs at the second coordination sphere. This would tend to suggest that the alloy which has a greater $W^{BC}(R_2)$ value would display a higher $L2_1 \leftrightarrow B2$ transformation temperature. The calculated $L2_1 \leftrightarrow B2$ transformation temperatures based on the data given in Table 6.2 for $Ni_{50}Mn_{50-x}Sb_x$, $Ni_{50}Mn_{50-x}In_x$ and $Ni_{50}Mn_{50-x}Ga_x$ alloys are shown in Figures 6.4-6.8 as a function of C alloying element composition. It is evident from Figures 6.4-6.8 that the model proposed by Kainuma et al. [21], Equation (4.19), yields to higher $L2_1 \leftrightarrow B2$ transformation temperatures than that of model proposed by Murakami et al. [14], Equation (4.15), for all alloy systems under investigation.

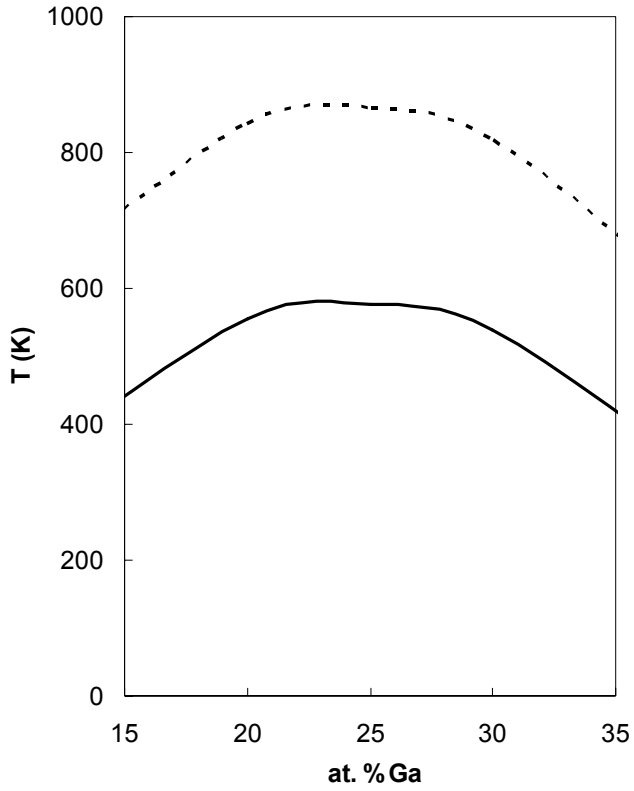

Figure 6.4 $L2_1 \leftrightarrow B2$ transformation temperatures calculated by using Equation (4.15) (solid line) and Equation (4.19) (dotted line) for $Ni_{50}Mn_{50-x}Ga_x$ alloy in the composition range of 15<x at% <35.

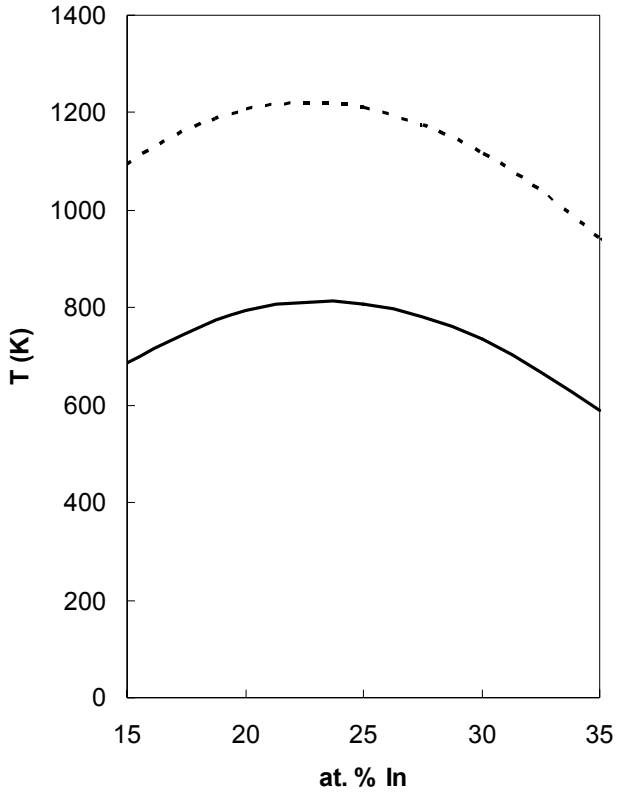

Figure 6.5 $L2_1 \leftrightarrow B2$ transformation temperatures calculated by using Equation (4.15) (solid line) and Equation (4.19) (dotted line) for $Ni_{50}Mn_{50-x}In_x$ alloy in the composition range of 15<x at% <35.

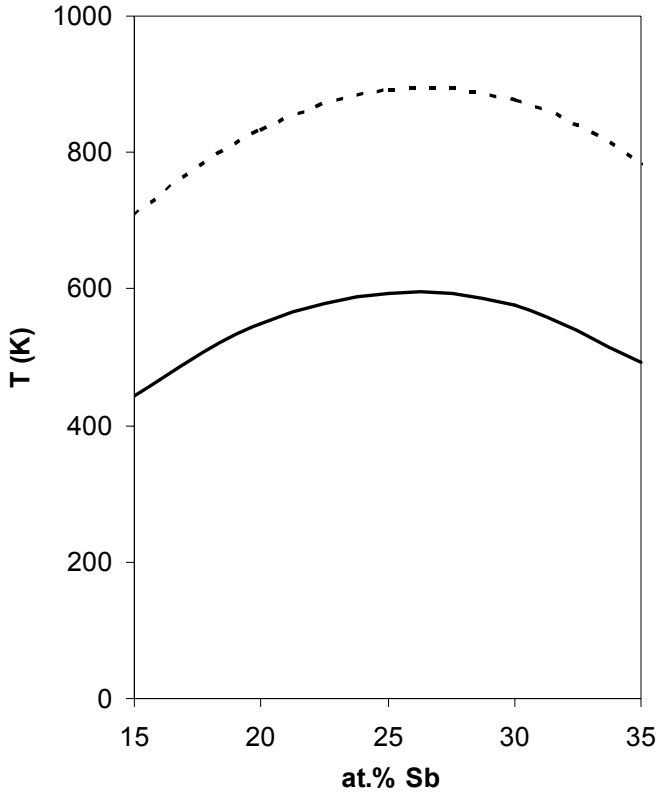

Figure 6.6 $L2_1 \leftrightarrow B2$ transformation temperatures calculated by using Equation (4.15) (solid line) and Equation (4.19) (dotted line) for $Ni_{50}Mn_{50-x}Sb_x$ alloy in the composition range of 15<x at% <35.

The experimental quasi-binary temperature-composition diagram [16] in which the boundaries of the $L2_1 \leftrightarrow B2$ and $B2 \leftrightarrow A2$ transformations for the $Ni_{50}Mn_{50-x}Ga_x$ alloy is illustrated in Figure 6.7 Calculated $L2_1 \leftrightarrow B2$ transformation temperature, according to Equation (4.19), is also shown in the same figure for comparison with experimental data.

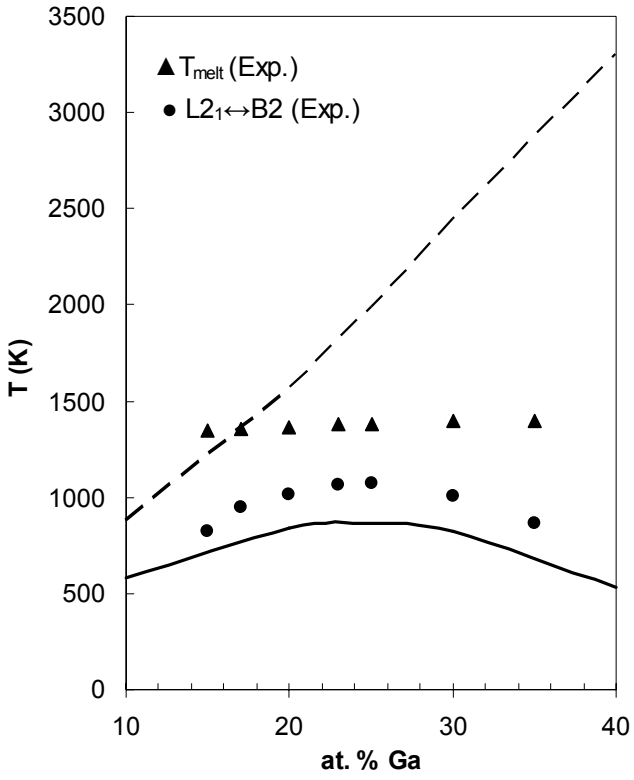

Figure 6.7 Composition temperature diagram showing the calculated $L2_1 \leftrightarrow B2$ (solid line) and $B2 \leftrightarrow A2$ (dashed line) transitions for $Ni_{50}Mn_{50-x}Ga_x$ alloy, experimental data is taken from [16].

The variation of $L2_1 \leftrightarrow B2$ transformation temperature as a function of composition, x, shows a parabolic behaviour for both theoretical prediction and experimentally reported data. The difference between the experimental and calculated transformation temperatures is found to be ~205 K for the stoichiometric Ni_2MnGa alloy indicating a relatively good qualitative agreement.

It is interesting to note that the $L2_1 \leftrightarrow B2$ transformation temperature decreases with an increase in the valence electron concentration of atoms substituted at C lattice site of Ni_2MnC (C=In, Sb) alloys, Figure 6.8 Such a decrease in the $L2_1 \leftrightarrow B2$ transformation temperature due to substitution of atoms at the C lattice site with atoms having a greater electron concentration was also reported for other Ni_2AlC (C= Ti, V, Cr or Mn) full Heusler alloys [118].

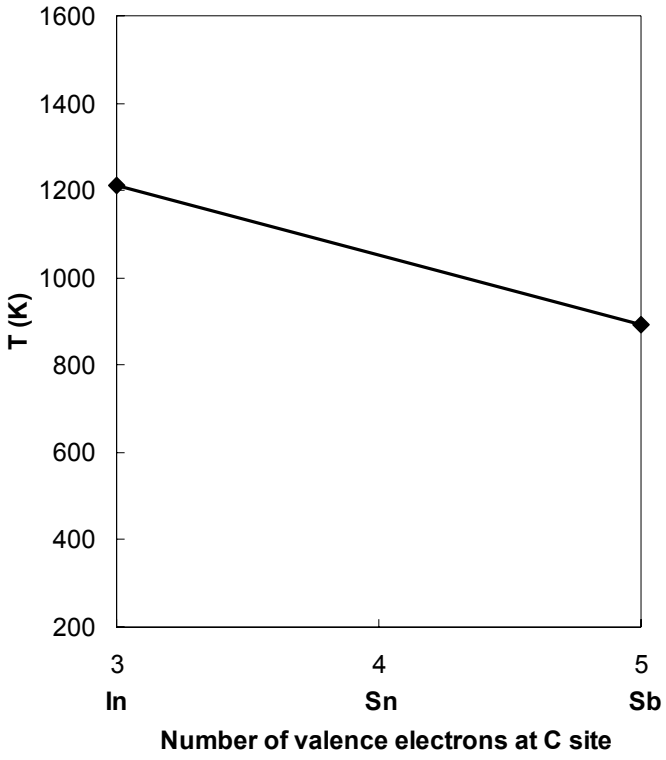

Figure 6.8 $L2_1 \leftrightarrow B2$ transformation temperature for the stoichiometric Ni_2MnC (C=In, Sb) alloys as a function of number of valence electrons at C lattice site. Number of valence electrons for In, Sn and Sb atoms are taken as 3, 4 and 5 respectively.

6.1.1.2. B2↔A2 (order-disorder) Phase Transformation for the $Ni_{50}Mn_{50-x}C_x$ (C=Ga, In, Sb) Heusler Alloys

As it was shown in Equation (4.10), the prediction of B2↔A2 transformation temperatures requires calculation of magnitudes of the partial ordering energies for A-B, A-C and B-C atomic pairs at the first coordination sphere only. Calculated values of the partial ordering energies at the 1st coordination sphere for $Ni_{50}Mn_{50-x}C_x$ (C = In, Sb and Ga) alloys are presented in Table 6.3 Calculated

B2↔A2 transformation temperatures based on data given in Table 6.3 imply that B2↔A2 order-disorder phase transformation would occur at very high temperatures even above the melting point of the alloys. This would tend to suggest that B2 ordered superstructure could prevail in the liquid state which makes the experimental determination of transformation temperatures impractical. It is of research interest to clarify and validate the utilization of present approach based on the combination of statistical thermodynamical theory with electronic theory in pseudopotential approximation for the prediction of B2↔A2 transformation temperatures in $Ni_{50}Mn_{50-x}C_x$ alloys by comparing with experimentally available data in the literature. Therefore, such a comparison could only be made for $Ni_{50}Mn_{50-X}Ga_X$ alloys which has been studied experimentally by Overholser et al. [16]. Calculated B2↔A2 transformation temperatures based on the present approach are plotted as a function of Ga concentration for $Ni_{50}Mn_{50-X}Ga_X$ alloys in Figure 6.7 where experimentally determined melting temperatures of these alloys are also shown for comparison.

Table 6.3 Calculated $W^{AB}(R_1)$, $W^{AC}(R_1)$ and $W^{BC}(R_1)$ values for the $A_{50}B_{50-x}C_x$ alloy where A=Ni, B=Mn, C=Ga, In, Sb

	Partial Ordering Energies at R_1 ($x10^{-3}$) (at. u.)								
	C= Ga			C= In			C= Sb		
at. %C	W^{AB}	W^{AC}	W^{BC}	W^{AB}	W^{AC}	W^{BC}	W^{AB}	W^{AC}	W^{BC}
10	0.49	-0.209	-2.084	0.405	6.536	4.289	0.443	15.802	9.920
20	0.487	-0.31	-2.141	0.393	5.827	3.766	0.442	16.182	10.39
25	0.486	-0.355	-2.166	0.39	5.544	3.549	0.441	16.345	10.39
35	0.485	-0.395	-2.213	0.387	5.298	3.358	0.441	16.495	10.51
45	0.483	-0.469	-2.254	0.385	4.900	3.037	0.44	16.756	10.74

It is evident from Figure 6.7 that, Tc_1 starts around 1000 K at 10 at.% of Ga, then linearly increases with increasing Ga content and reaches to a very high temperature of 3300 K at 40 at.%Ga. Overholser et al. [16] reported a similar composition-temperature diagram in which the B2↔A2 transformation temperature linearly increases from approximately 1400 K to 2375 K with increasing Mn content in the $Ni_{50}Mn_XGa_{50-X}$ alloy (10<x<40). However, Overholser et al. [16] pointed out that solid↔liquid transformation takes place before B2↔A2 transformation on heating, therefore, B2↔A2 transformation was not observed experimentally in the composition range of 10<x<40 for the $Ni_{50}Mn_XGa_{50-X}$ alloy. As can be seen from Figure 6.7, results of our calculations are in good qualitative agreement with experimental observations [16], where calculated B2↔A2 transformation temperatures are considerably higher than experimental solid↔liquid transformation temperatures. It seems that the B2↔A2 order-disorder transformation unlikely to occur in the solid state for $Ni_{50}Mn_{50-x}C_x$ (C = Ga, In and Sb) alloys in the 10<x<40 at% composition range.

6.1.2. Calculated (order-order) $L2_1$↔B2 Critical Phase Transformation Temperatures for the A_2BGa (A=Fe, Ni, Co; B=Ni, Mn, Co, Fe) Heusler Alloys

In this section, the calculated values of partial ordering energies for the second coordination sphere were used as input data for the superlattice formation models of R. Kainuma et al. [21] and Y. Murakami et al. [14]. The boundaries for the (order-order) $L2_1$↔B2 transition are determined for the $Ni_{50}Co_{50-x}Ga_x$, $Fe_{50}Co_{50-x}Ga_x$, $Fe_{50}Ni_{50-x}Ga_x$, $Co_{50}Mn_{50-x}Ga_x$ and $Co_{50}Fe_{50-x}Ga_x$ alloys (15<x<35). The calculated $L2_1$↔B2 transition temperatures were compared against the existing experimental data from literature.

Furthermore, in the previous section the effect of electron concentration at the C atomic site on the $L2_1$↔B2 transformation temperatures in Ni_2MnC (C= In, Sb) alloys were given. In this section this comparative study is extended to cover the

effect of electron concentration at the A and B atomic sites on the $L2_1 \leftrightarrow B2$ transformation temperature in A_2NiGa (A=Fe, Co), Ni_2BGa (B=Mn, Co), Fe_2BGa (B=Co, Ni) and Co_2BGa (B=Co, Fe) Heusler alloys. The trends of the calculated $L2_1 \leftrightarrow B2$ transformation temperatures with electron concentration are compared with the previously reported trends for the A_2BC –type Heusler alloys.

Experimental lattice parameters [130, 131] and calculated R_2 values are given in Table 6.4. Calculated values of $W^{BC}(R_2)$ which govern the $L2_1 \leftrightarrow B2$ order-order phase transformation in $Ni_{50}Co_{50-x}Ga_x$, $Fe_{50}Co_{50-x}Ga_x$, $Fe_{50}Ni_{50-x}Ga_x$, $Co_{50}Mn_{50-x}Ga_x$ and $Co_{50}Fe_{50-x}Ga_x$ alloys ($10<x<40$) are presented in Table 6.5. It is evident from the data given in Table 6.5 that partial ordering energy between B and C atoms for the second coordination sphere for $Ni_{50}Co_{50-x}Ga_x$, $Fe_{50}Co_{50-x}Ga_x$, $Fe_{50}Ni_{50-x}Ga_x$ and $Co_{50}Mn_{50-x}Ga_x$ alloys have a maximum at x=10 and this value decreases with the increase in Ga concentration in $10<x<40$.

Table 6.4 Experimental lattice parameters (a) tabulated together with calculated 2nd nearest neighbor distances (R_2). (1 at.u.(length) = 0.529177 Å).

Alloy	Ni_2CoGa	Fe_2CoGa	Fe_2NiGa	Co_2MnGa	Co_2FeGa
a (at.u.)	10.081[a]	10.898[a]	10.923[a]	10.9[a]	10.841[b]
R_2 (at.u.)	5.041	5.449	5.462	5.45	5.4205

[a] Reference [130].

[b] Reference [131].

Table 6.5 Calculated partial ordering energies for B-C atomic pairs at the second coordination sphere for $A_{50-x}B_{50}Ga_x$ alloys where A=Fe, Ni, Co; B=Ni, Mn, Co, Fe in the composition range of 10<x<40.

	Partial Ordering Energies ($x10^{-3}$) ($W^{BC}(R_2)$) (at.u.)				
$A_{50}B_{50-x}Ga_x$ x (at. %)	A=Ni, B=Co	A=Fe, B=Co	A=Fe, B= Ni	A=Co, B=Mn	A=Co, B=Fe
10	1.612	3.522	3.540	1.873	2.299
20	1.365	3.447	3.468	1.809	1.897
25	1.254	3.407	3.429	1.779	1.688
30	1.152	3.366	3.388	1.751	1.476
40	0.966	3.283	3.304	1.698	1.058

Among the investigated compositions, considering only stoichiometric A_2BC alloys with C= Ga, Fe_2NiGa and Fe_2CoGa alloys have the highest partial ordering energies between B and C atoms for the second coordination sphere. $L2_1 \leftrightarrow B2$ transition temperatures were determined by employing the calculated $W^{BC}(R_2)$ values given in Table 6.5 in Equations (4.15) and (4.19).

Partial ordering energies calculated as a function of interatomic distance by using the electronic theory of alloys in pseudopotential approximation are given in Figures 6.9-6.12 for B-C pairs in the A_2MnGa (A=Ni, Co), Ni_2BGa (B=Mn, Co), Fe_2BGa (B=Ni, Co) and Co_2BGa (B=Fe, Mn) alloys, respectively.

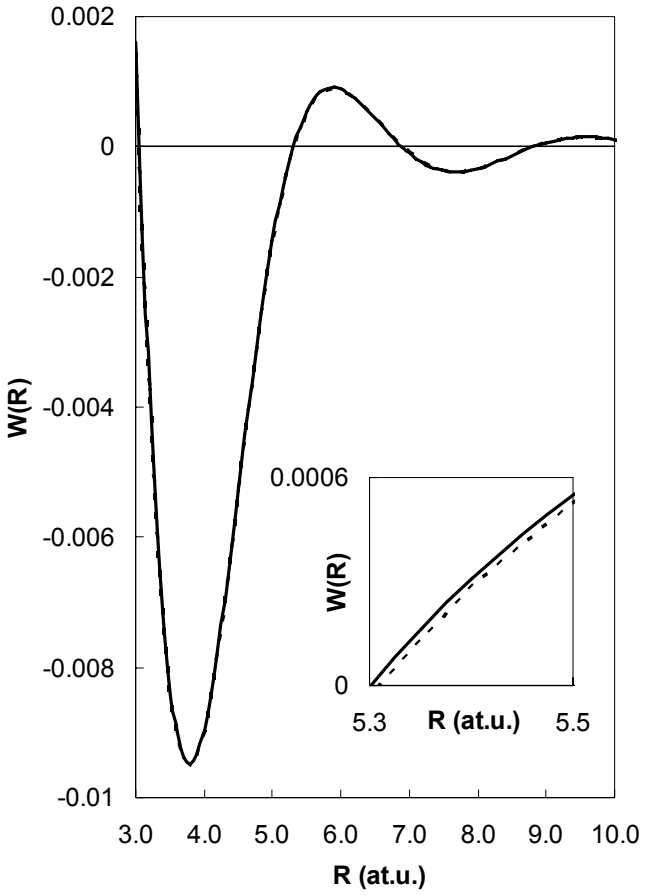

Figure 6.9 Variation of partial ordering energies for Mn-Ga pair with interatomic distance, R, for the stoichiometric Ni_2MnGa (dotted line) and Co_2MnGa (solid line) alloy. The inset shows W(R) in 5.3<R<5.5 in more detail. (1 at. u.(energy) = 2 Ry = 27.2 eV; 1at. u.(length) = 0.529177 Å)

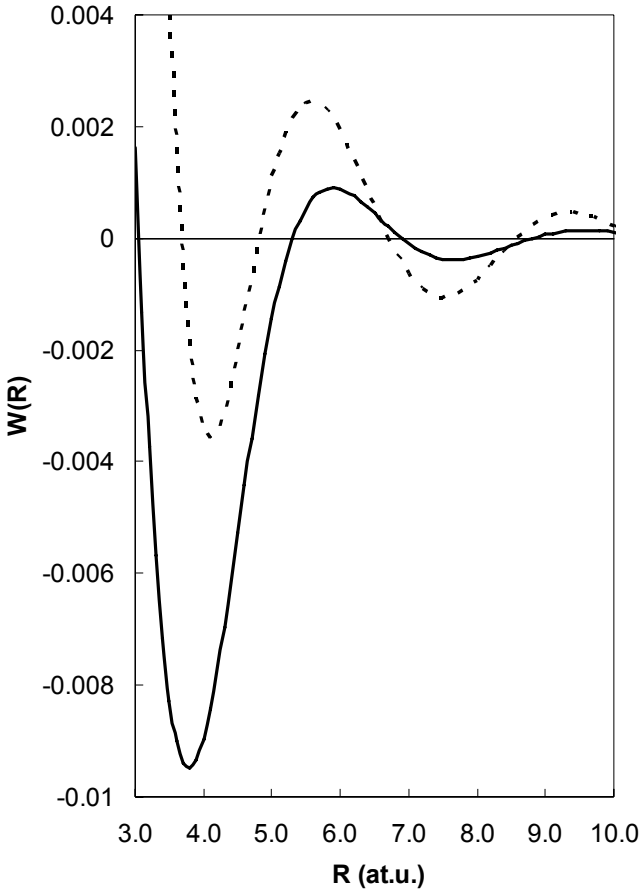

Figure 6.10 Variation of partial ordering energies for Mn-Ga and Co-Ga pairs with interatomic distance, R, for the stoichiometric Ni_2MnGa (solid line) and Ni_2CoGa (dotted line) alloys. (1 at. u.(energy) = 2 Ry = 27.2 eV; 1at. u.(length) = 0.529177 Å)

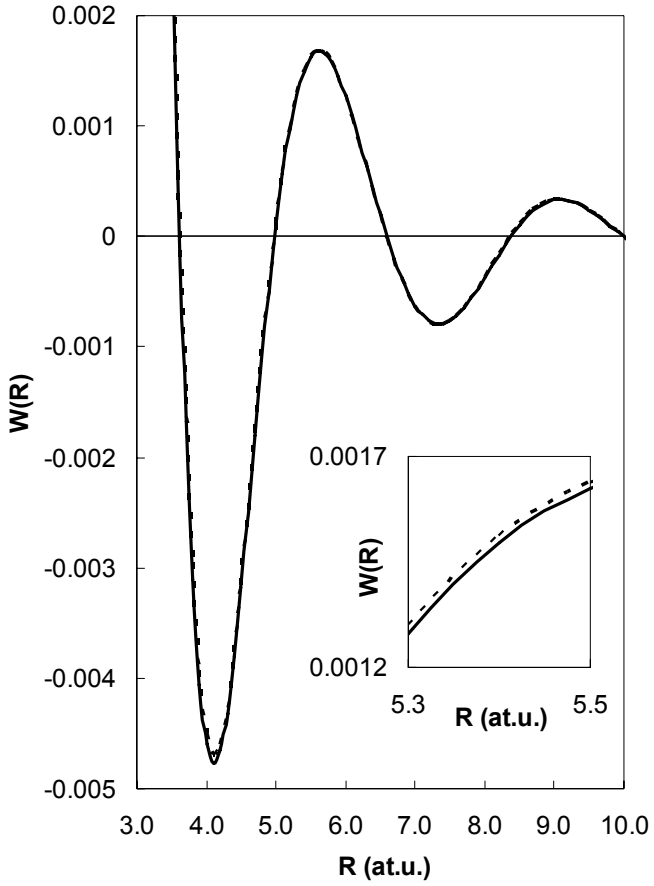

Figure 6.11 Variation of partial ordering energies for Ni-Ga and Co-Ga pairs with interatomic distance, R, for the stoichiometric Fe_2NiGa (dotted line) and Fe_2CoGa (solid line) alloys. The inset shows W(R) in 5.3<R<5.5 in more detail. (1 at. u.(energy) = 2 Ry = 27.2 eV; 1at. u.(length) = 0.529177 Å)

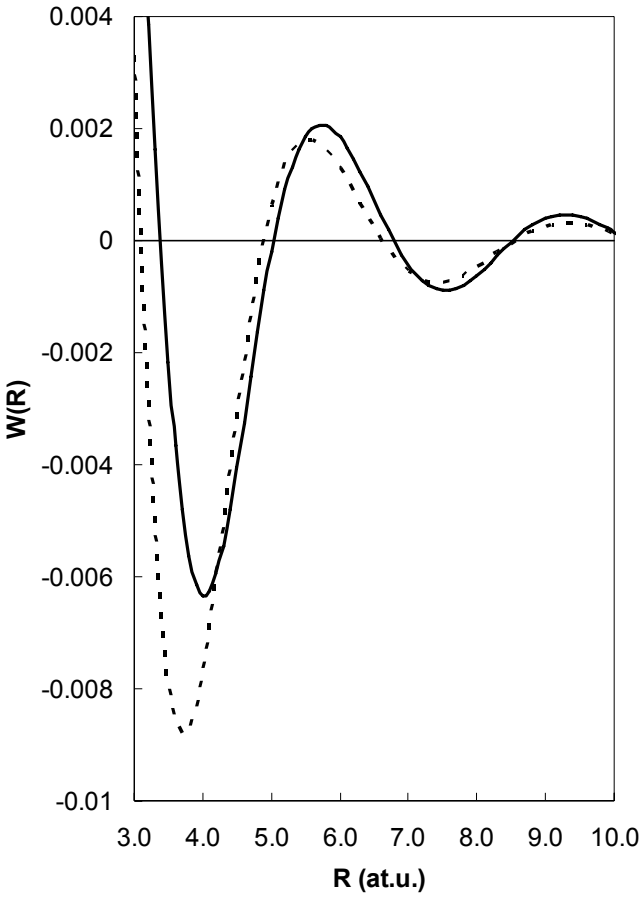

Figure 6.12 Variation of partial ordering energies for Mn-Ga and Fe-Ga pairs with interatomic distance, R, for the stoichiometric Co_2MnGa (dotted line) and Co_2FeGa (solid line) alloys. (1 at. u.(energy) = 2 Ry = 27.2 eV; 1at. u.(length) = 0.529177 Å)

It can be seen from Figure 6.9 that partial ordering energies for Mn-Ga pair as a function of interatomic distance for the Ni_2MnGa and Co_2MnGa alloys follow the same path. This suggests that substitution of Ni for Co at the A site has a negligible affect on the calculated partial ordering energies for the Mn-Ga pair in A_2MnGa (A=Ni and Co) alloys. Similarly, it is evident from Figure 6.11 that $W^{BC}(R_2)$ values for the Fe_2NiGa and Fe_2CoGa alloys are identical in 3<R at.u.<10, indicating that substitution of Ni for Co has an insignificant effect on partial ordering energies for the Ni-Ga and Co-Ga pairs.

The calculated values of partial ordering energies were used as input data for the superlattice formation model of Y. Murakami et al. and R. Kainuma et al. The boundaries for the $L2_1 \leftrightarrow B2$ transitions calculated for the $Ni_{50}Mn_{50-x}Ga_x$, $Co_{50}Mn_{50-x}Ga_x$, $Ni_{50}Co_{50-x}Ga_x$, $Fe_{50}Ni_{50-x}Ga_x$, $Fe_{50}Co_{50-x}Ga_x$, $Co_{50}Fe_{50-x}Ga_x$ and $Co_{50}Mn_{50-x}Ga_x$ alloys are given in Figures 6.4 and 6.13-6.18 respectively.

It is evident from Figures 6.4 and 6.13 that $Ni_{50}Mn_{50-x}Ga_x$ has higher $L2_1 \leftrightarrow B2$ transition temperatures in the composition range 15<x<35. As mentioned previously, the ordering energies between the Mn-Ga pair has similar values for the $Ni_{50}Mn_{50-x}Ga_x$ and $Co_{50}Mn_{50-x}Ga_x$ alloys but the variation in R_2 values results in different $L2_1 \leftrightarrow B2$ transformation temperatures for these alloys.

Although the values of the partial ordering energies between B and C atoms for the Ni_2CoGa alloy are greater than the Ni_2MnGa alloy where $W^{BC}(R) > 0$ (Figure 6.10), the $L2_1 \leftrightarrow B2$ transition temperature of the Ni_2MnGa alloy is higher than that of the Ni_2CoGa alloy due to smaller value of the R_2 for the Ni_2CoGa alloy (Figures 6.4 and 6.14).

It is obvious from Figures 6.15 and 6.16 that the $L2_1 \leftrightarrow B2$ phase transformation temperatures for the $Fe_{50}Ni_{50-x}Ga_x$ and $Fe_{50}Co_{50-x}Ga_x$ alloys have similar values (± 6 K) which results in overlapping of the two curves representing the boundaries for $L2_1 \leftrightarrow B2$ transition for the $Fe_{50}Ni_{50-x}Ga_x$ and $Fe_{50}Co_{50-x}Ga_x$ alloys. Furthermore, the results obtained from the calculations based on the model of Y. Murakami et al. for the $Fe_{50}Co_{50-X}Ga_X$ alloy (Figure 6.16) are in fairly good agreement with the experimental transition temperature data from [131].

Below 23% Ga, $Co_{50}Fe_{50-X}Ga_X$ and above 23% Ga, $Co_{50}Mn_{50-X}Ga_X$ exhibits higher $L2_1 \leftrightarrow B2$ transition temperatures (Figures 6.17 and 6.18). The experimental temperature data from [131] exhibits a similar parabolic behaviour with the $L2_1 \leftrightarrow B2$ transition temperatures which were calculated according to the model of R. Kainuma et al. for the $Co_{50}Fe_{50-X}Ga_X$ alloy.

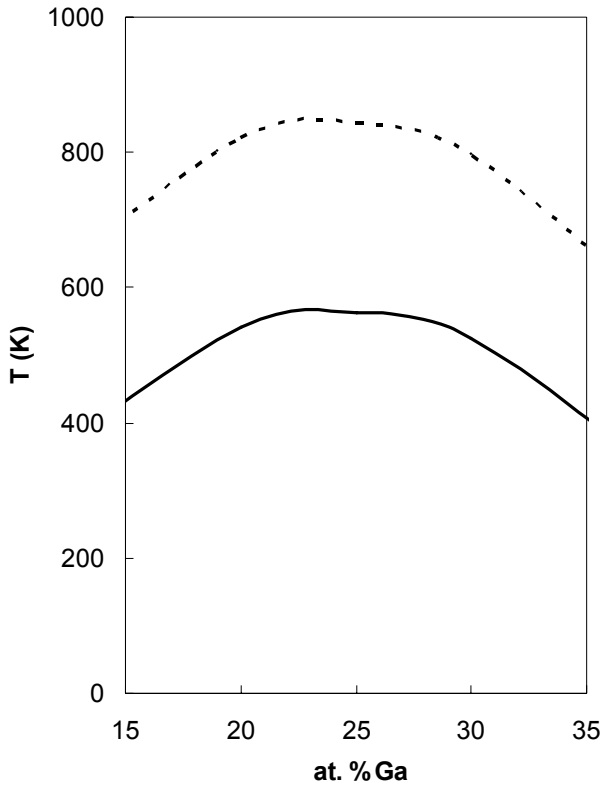

Figure 6.13 $L2_1 \leftrightarrow B2$ transformation temperatures calculated by using Equation (4.15) (solid line) and Equation (4.19) (dotted line) for $Co_{50}Mn_{50-x}Ga_x$ alloy in the composition range of 15<x at% <35.

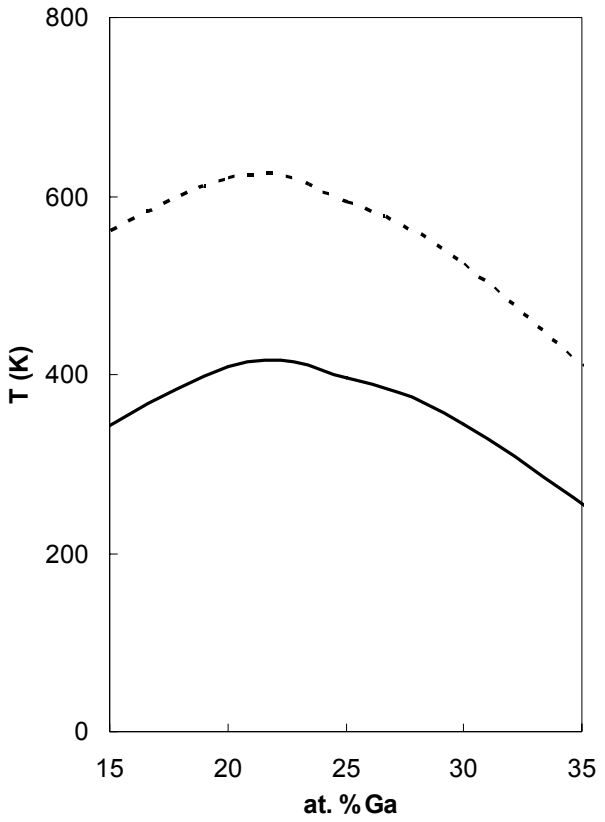

Figure 6.14 $L2_1 \leftrightarrow B2$ transformation temperatures calculated by using Equation (4.15) and Equation (4.19) for $Ni_{50}Co_{50-x}Ga_x$ alloy in the composition range of $15<x$ at% <35.

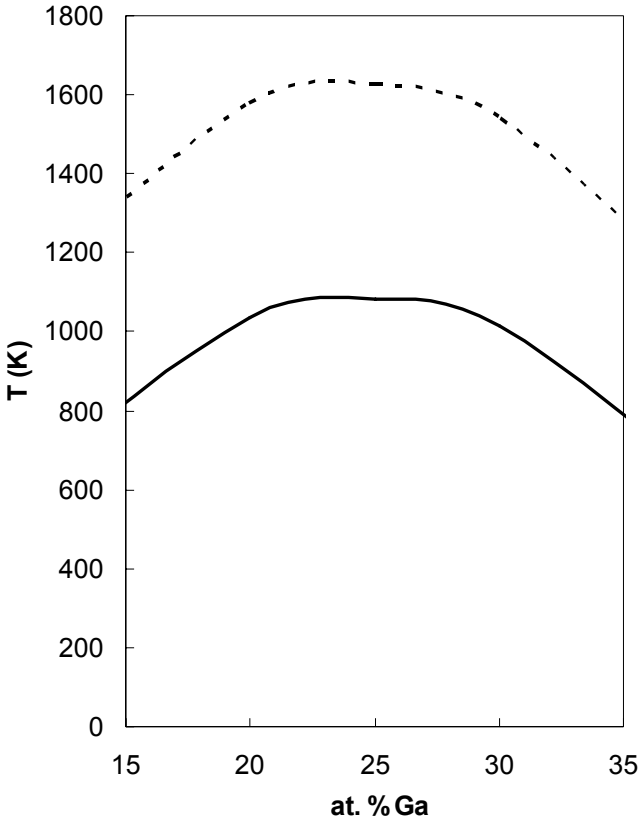

Figure 6.15 $L2_1 \leftrightarrow B2$ transformation temperatures calculated by using Equation (4.15) (solid line) and Equation (4.19) (dotted line) for $Fe_{50}Ni_{50-x}Ga_x$ alloy in the composition range of 15<x at% <35.

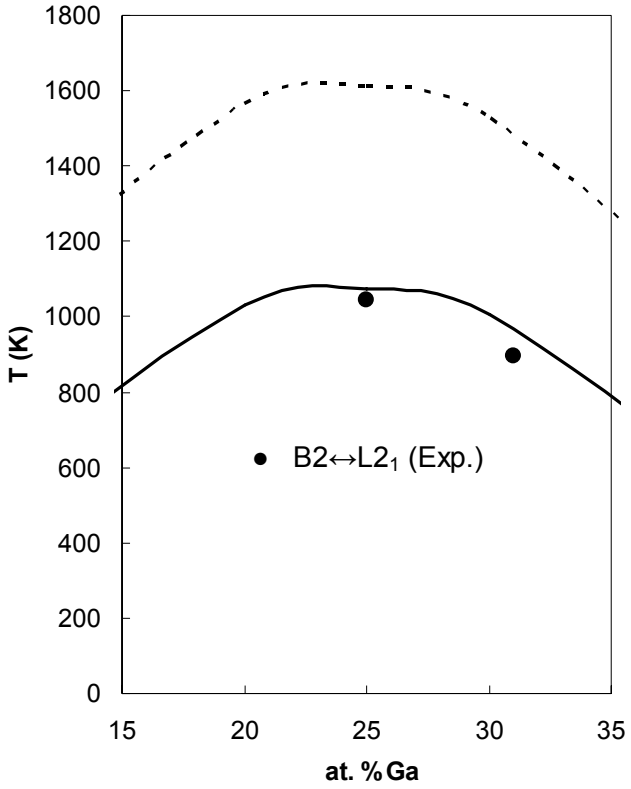

Figure 6.16 $L2_1 \leftrightarrow B2$ transformation temperatures calculated by using Equation (4.15) (solid line) and Equation (4.19) (dotted line) for the $Fe_{50}Co_{50-x}Ga_x$ alloy in the composition range of 15<x at% <35, experimental data from [131].

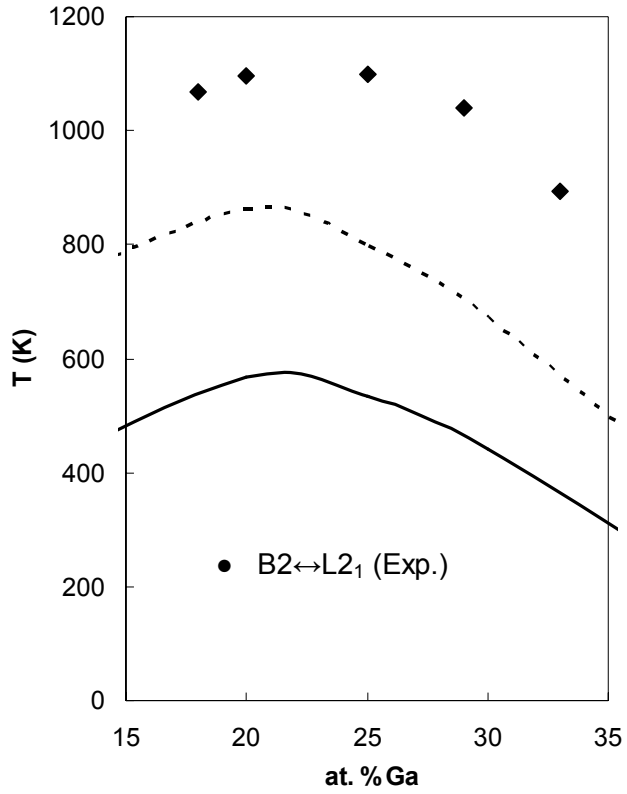

Figure 6.17 $L2_1 \leftrightarrow B2$ transformation temperatures calculated by using Equation (4.15) (solid line)and Equation (4.19) (dotted line) for $Co_{50}Fe_{50-x}Ga_x$ alloy in the composition range of 15<x at% <35, experimental data from [131].

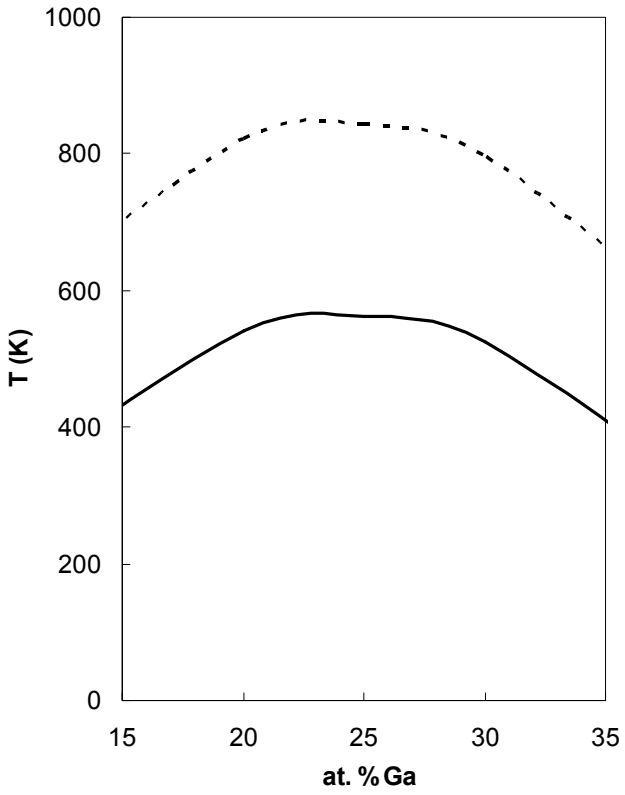

Figure 6.18 $L2_1 \leftrightarrow B2$ transformation temperatures calculated by using Equation (4.15) (solid line) and Equation (4.19) (dotted line) for $Co_{50}Mn_{50-x}Ga_x$ alloy in the composition range of 15<x at% <35.

In Figures 6.19-6.22, the effect of changes in electron concentration at A and B atomic sites on $L2_1 \leftrightarrow B2$ transition temperatures are given for A_2MnGa (A=Ni, Co), Ni_2BGa (B=Mn, Co), Co_2BGa (B=Fe, Mn) and Fe_2BGa (B=Ni, Co) alloys, respectively.

It is interesting to note that increasing the electron concentration at the A atomic site by substitution of Ni for Co in A_2MnGa (A=Ni and Co) alloys leads to an increase of the $L2_1 \leftrightarrow B2$ transition temperature (23 K), Figure 6.19. A similar relationship between the e/a at A site and $L2_1 \leftrightarrow B2$ transition temperature was reported for A_2AlTi (A=Fe, Co, Ni and Cu) alloys [17, 18, 21].

$Ni_{50}Mn_{50-x}Ga_x$ alloy has higher $L2_1 \leftrightarrow B2$ transition temperatures compared to $Ni_{50}Co_{50-x}Ga_x$ alloy in the composition range of $15<x$ at% <35. Figure 6.20 shows the decrease in $L2_1 \leftrightarrow B2$ transition temperatures due to the substitution of Mn for Co at the B atomic site. Similarly, there is a decrease in the $L2_1 \leftrightarrow B2$ transition temperatures with an increase in the number of 3d+4s electrons at B atomic site on the substitution of Fe for Mn, Figure 6.21. The decrease in the $L2_1 \leftrightarrow B2$ transition temperatures due to the substitution of atoms at B site with an atom having a greater electron concentration given in Figures 6.20 and 6.21 were also observed in Ni_2BAl (B= Ti, V, Cr or Mn) alloys [19].

It is evident from Figure 6.18 that the $L2_1 \leftrightarrow B2$ transition temperature is almost constant for the Fe_2CoGa and Fe_2NiGa alloys. Therefore, in order to obtain a general trend for the changes in $L2_1 \leftrightarrow B2$ transition temperature with electron concentration at the B site for Fe_2BGa (B=Ni, Co) alloys, additional calculations including the elements Mn, Fe and Cu are necessary. However, because of the limited experimental lattice parameter data for these alloys these calculations could not be performed in this study.

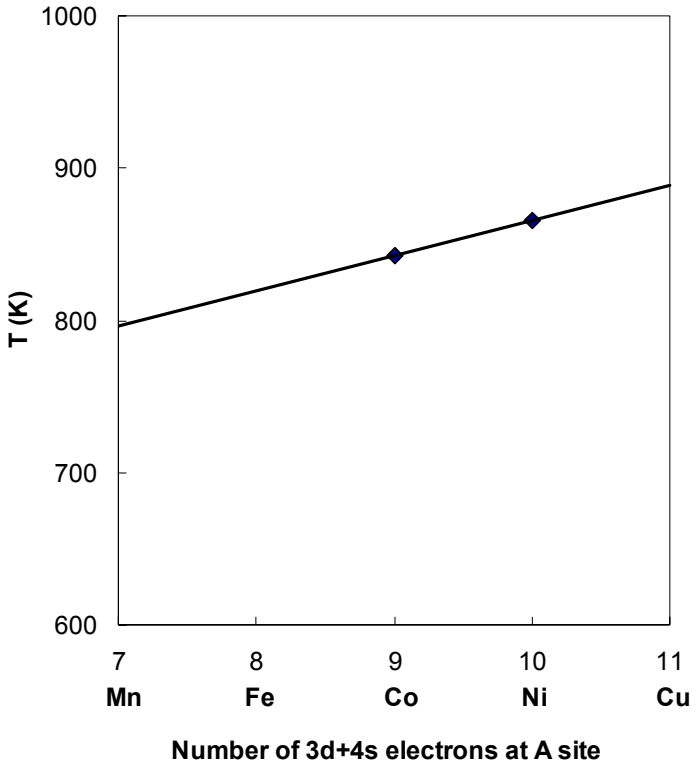

Figure 6.19 $L2_1 \leftrightarrow B2$ transformation temperature calculated according to the model of R. Kainuma et al.for the stoichiometric A_2MnGa (A=Ni and Co) alloys as a function of number of 3d+4s electrons at A lattice site. Number of 3d+4s electrons for Mn, Fe, Co, Ni and Cu atoms are taken as 7, 8, 9, 10 and 11 respectively.

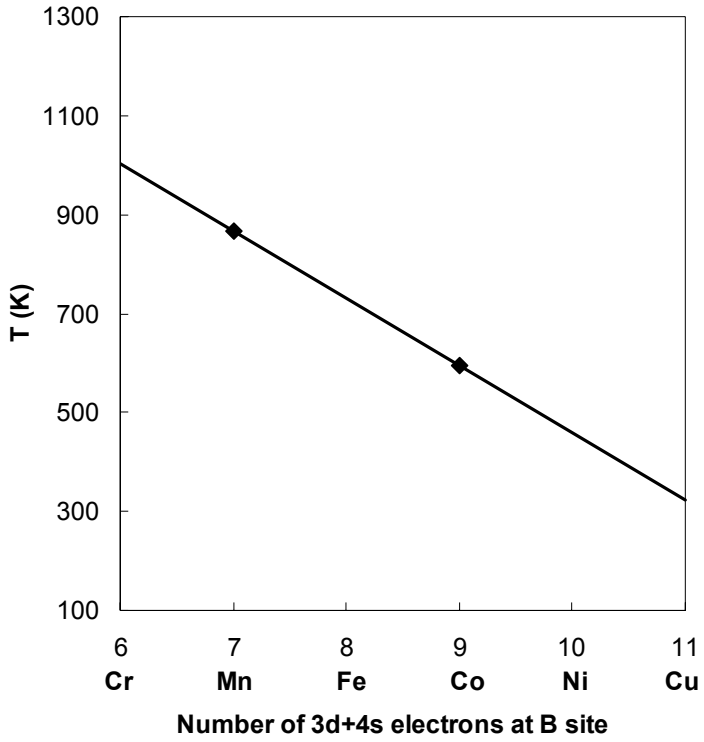

Figure 6.20 $L2_1 \leftrightarrow B2$ transformation temperatures calculated according to the model of R. Kainuma et al. for the stoichiometric Ni_2BGa (B=Mn and Co) alloys as a function of number of 3d+4s electrons at B lattice site. Number of 3d+4s electrons for Cr, Mn, Fe, Co, Ni and Cu atoms are taken as 6, 7, 8, 9, 10 and 11 respectively.

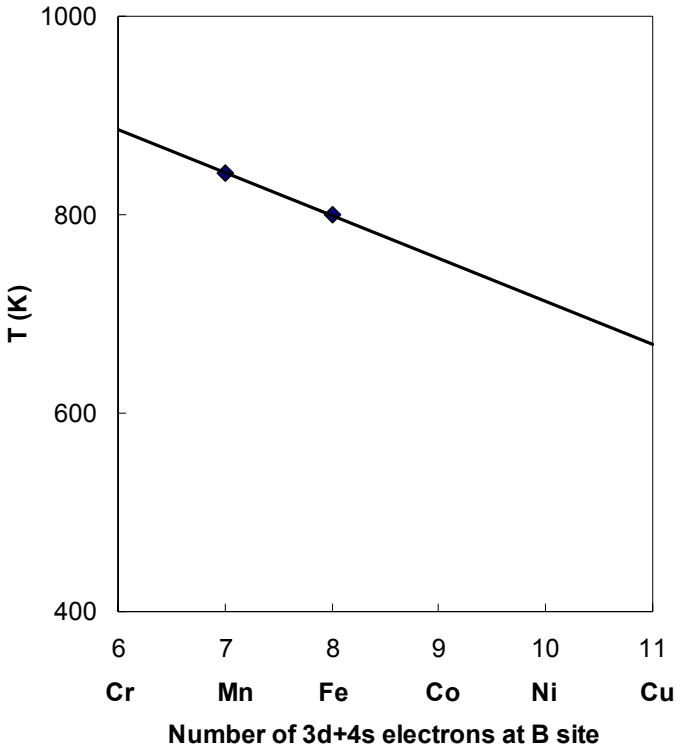

Figure 6.21 $L2_1 \leftrightarrow B2$ transformation temperature calculated according to the model of R. Kainuma et al.for the stoichiometric Co_2BGa (B=Fe and Mn) alloys as a function of number of 3d+4s electrons at B lattice site. Number of 3d+4s electrons for Cr, Mn, Fe, Co, Ni and Cu atoms are taken as 6, 7, 8, 9, 10 and 11 respectively.

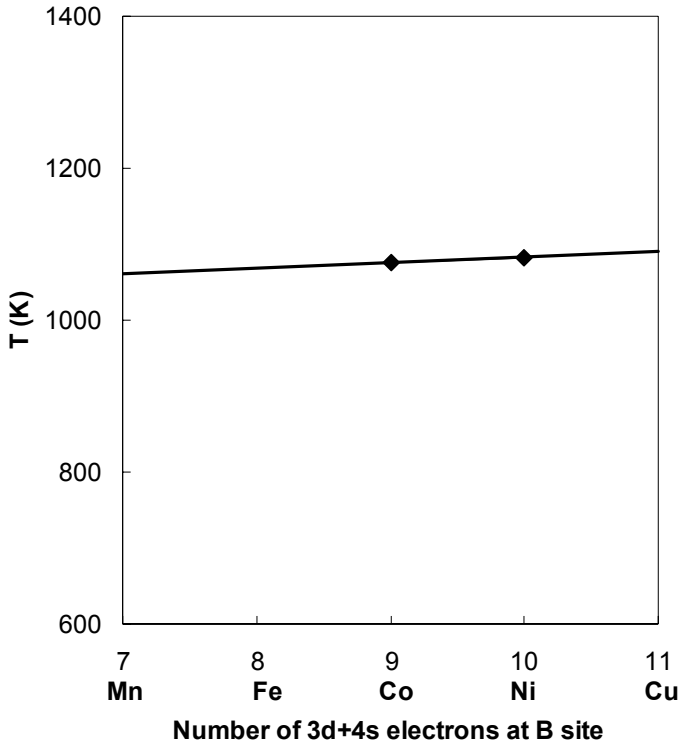

Figure 6.22 $L2_1 \leftrightarrow B2$ transformation temperature calculated according to the model of R. Kainuma et al.for the stoichiometric Fe_2BGa (B=Ni and Co) alloys as a function of number of 3d+4s electrons at B lattice site. Number of 3d+4s electrons for Mn, Fe, Co, Ni and Cu atoms are taken as 7, 8, 9, 10 and 11 respectively.

Thus, current predictions based on the statistico-thermodynamical theory of ordering by means of BWG methods combined with the electronic theory of alloys in the pseudopotential approximation, in regard to the modelling of the order-order ($B2 \leftrightarrow L2_1$) and order-disorder ($A2 \leftrightarrow B2$) phase transformations in the complex $Ni_{50}Mn_{50-x}C_x$ (C=Ga, In, Sb) and A_2BGa (A=Fe, Ni, Co; B=Ni, Mn, Co, Fe) full Heusler alloys are consistent qualitatively at the wide concentration range of $15<x<35$, with experimental observations reported in the literature. However, calculated magnitudes of order-order, Tc_2, and order-disorder, Tc_1, transformation temperatures show relatively slight deviation from the experimentally determined values. Such discrepancies are expected and may be attributed to the assumptions made in the calculation of partial ordering energies which do not take into account the effect of structural relaxations due to the atomic size differences, covalency, self-consistency, many-body-interactions etc. and also inter-influence of atomic and magnetic ordering processes. Furthermore, in the constructed lattice model of BWG approximations, the lattice is assumed to be both perfect (neglecting lattice defects, such as dislocations, grain boundaries etc) and rigid (neglecting lattice vibrations and elastic strains), so that only the configurational problem is taken into consideration. It is obvious that, for quantitative characterization of atomic and magnetic ordering processes and also for construction of complete theoretical phase diagrams of complex A_2BC-type ordered full Heusler alloys, the all above-mentioned and other factors should be taken into account in the constructed lattice model, that is not the intention of the theoretical part of the thesis.

6.2. EXPERIMENTAL INVESTIGATIONS ON THE STRUCTURAL AND MAGNETIC PROPERTIES OF Ni-Mn-Ga AND Ni-Mn-Al FULL HEUSLER ALLOYS

The results and discussion of the experimental investigations on the Ni-Mn-Ga and Ni-Mn-Al Heusler alloy systems are presented separately in this chapter. For the Ni-Mn-Ga Heusler alloy system, effects of composition on crystal structures and phase transformation temperatures were investigated. The magnetic properties, in particular, the magnetocaloric properties were investigated at the magneto-structural phase transformations for Ni-rich Ni-Mn-Ga Heusler alloys. For the Ni-Mn-Al alloy system, the effects of composition and aging on the atomic ordering and magnetic properties were examined. Furthermore, the MCE was determined for the stoichiometric Ni_2MnAl alloy.

6.2.1. Structural and Magnetic Properties of Ni-Mn-Ga Full Heusler Alloys

In this part, experimental results and their discussion are presented for the Ni-Mn-Ga full Heusler alloys. The compositions of the investigated Ni-Mn-Ga Heusler alloys determined by EDS analyses are given in Table 6.6 together with calculated e/a values and lattice parameters. Calculated lattice parameters are consistent with the previously reported values [79, 91]. The e/a values were calculated by using Equation 4.1.

Table 6.6 Compositions, lattice constants (a,b and c) and e/a for investigated Ni-Mn-Ga alloys.

Nominal Composition	Ni (at.%)	Mn (at.%)	Ga (at.%)	a=b (Å)	c (Å)	e/a
$Ni_{49}Mn_{25}Ga_{26}$	48.91	25.13	25.96	5.82	-	7.43
$Ni_{54}Mn_{20}Ga_{26}$	54.15	20.06	25.79	7.65	6.62	7.59
$Ni_{56}Mn_{18}Ga_{26}$	55.77	18.20	26.03	7.65	6.62	7.63

6.2.1.1. Effects of composition on crystal structure in $Ni_{49+x}Mn_{25-x}Ga_{26}$ (x=0, 5 and 7) Heusler alloys

XRD measurements were performed to investigate the effect of composition on crystal structure of the Ni-rich Ni-Mn-Ga alloys. XRD patterns of the as-cast $Ni_{49+x}Mn_{25-x}Ga_{26}$ (x=0, 5 and 7) alloys are given in Figure 6.23. All the fundamental peaks related to the A2 phase are present in the XRD pattern of the as-cast $Ni_{49}Mn_{25}Ga_{26}$ alloy. In the A2 phase, Ni, Mn and Ga atoms are randomly distributed over the body centered lattice sites of the $L2_1$ –type crystal structure (Figure 4.2). Because of the texturing in the polycrystalline Ni-Mn-Ga alloys the reflections related to the next nearest neighbour ordering and unique to the fully ordered $L2_1$ phase were not observed in many cases. Conventionally, although the observed reflections indicate the presence of A2 or B2 phases, the structure was treated as if it was the fully ordered $L2_1$ phase [53, 132, 133].

All the peaks observed in the XRD pattern of the as-cast $Ni_{54}Mn_{20}Ga_{26}$ and $Ni_{56}Mn_{18}Ga_{26}$ alloys (Figure 6.23) can be indexed according to the $L1_0$ –type structure with identical lattice parameters. The $L1_0$ –type structure is a tetragonal distortion of the fcc structure. On the transition from the $L2_1$ –type structure, the equivalent of this structure is the double $L1_0$ structure. Similar non-modulated

martensitic structures with martensitic transformation temperatures higher than the RT were observed in Ni-Mn-Ga alloys [91]. J. Pons et al reported the presence of $L1_0$ phase at RT in Ni-Mn-Ga alloys with e/a values between 7.67 and 8.10 [91]. This study shows the occurrence of these non-modulated martensitic structures in Ni-Mn-Ga alloys with e/a between 7.59 and 7.63.

Keeping Ga composition constant and substituting Ni for Mn increases e/a in Ni-Mn-Ga alloys. It was well established that the increase in e/a results in the unstabilization of the cubic structure and an increase in the T_M [2]. The XRD data shown in Figure 6.23 shows that as cast $Ni_{49}Mn_{25}Ga_{26}$ (e/a=7.43) has the cubic $L2_1$-type crystal structure, on the other hand, both the as cast $Ni_{54}Mn_{20}Ga_{26}$ (e/a=7.59) and $Ni_{56}Mn_{18}Ga_{26}$ (e/a=7.63) alloys have martensitic $L1_0$-type crystal structure at RT. It is evident from Figure 6.23 that, the splitting between the (222) and (440) peaks is more pronounced and the intensity of (400) peak is higher in $Ni_{56}Mn_{18}Ga_{26}$ alloy compared to the $Ni_{54}Mn_{20}Ga_{26}$ alloy. This can be attributed due to the higher e/a value of $Ni_{56}Mn_{18}Ga_{26}$ alloy.

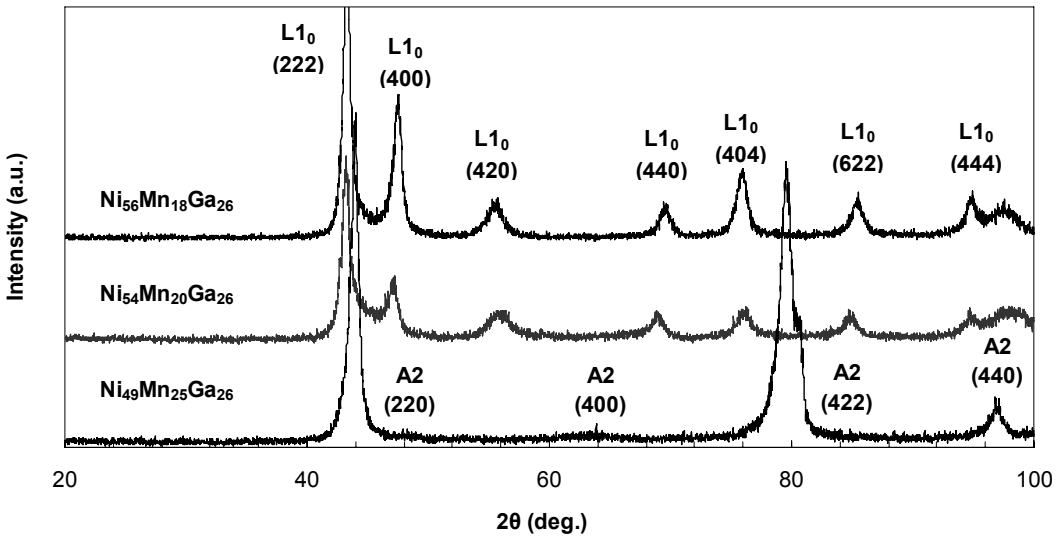

Figure 6.23 XRD pattern for the as-cast $Ni_{49+x}Mn_{25-x}Ga_{26}$ (x=0, 5 and 7) alloys measured at RT.

6.2.1.2. Effects of composition on the magnetic properties and phase transitions of $Ni_{49+x}Mn_{25-x}Ga_{26}$ (x=0, 5 and 7) Heusler alloys

Magnetic field and temperature dependence of magnetization are measured for the as-cast $Ni_{49+x}Mn_{25-x}Ga_{26}$ (x=0, 5 and 7) alloys with the intention of characterizing the magnetic behaviour and phase transitions in these alloys.

RT M-H curves are given for the as-cast $Ni_{49+x}Mn_{25-x}Ga_{26}$ (x=0, 5 and 7) alloys in Figures 6.24-6.26, respectively. It is evident from Figures 6.24-6.26 that as-cast $Ni_{49+x}Mn_{25-x}Ga_{26}$ (x=0, 5 and 7) alloys exhibit a strong ferromagnetic behaviour because large magnetization is obtained in these alloys on application of relatively small magnetic fields and in addition to that, magnetization saturates above a certain field. XRD could not supply information about the degree of ordering in the as-cast $Ni_{49}Mn_{25}Ga_{26}$ alloy due to texturing but the observed ferromagnetic behaviour indicates that the ferromagnetic $L2_1$ phase is present in this alloy.

Calculated $L2_1 \leftrightarrow B2$ transition temperature data for the $Ni_{50}Mn_{50-x}Ga_x$ ($10<x<40$) alloys shown in Figure 6.7 suggests that Ni_2MnGa alloy has the highest $L2_1 \leftrightarrow B2$ transition temperature among $Ni_{50}Mn_{50-x}Ga_x$ ($10<x<40$) alloys. Therefore, quenching Ni_2MnGa and near stoichiometric Ni-Mn-Ga Heusler alloys from high temperatures results in the formation of a pure $L2_1$ phase in these alloys. The arc melter employed in the production of $Ni_{49}Mn_{25}Ga_{26}$ alloy provides very high cooling rates, which may be equivalent to the cooling rates that occur in quenching process. As a result, the ferromagnetic $L2_1$ phase is present in the as-cast $Ni_{49}Mn_{25}Ga_{26}$ alloy.

It is evident from the insets of Figures 6.24-6.26 that the hysteresis of the $Ni_{56}Mn_{18}Ga_{26}$ and $Ni_{54}Mn_{20}Ga_{26}$ alloys are significantly larger than the $Ni_{49}Mn_{25}Ga_{26}$ alloy. This can be attributed to the less symmetrical tetragonal crystal structure of the $Ni_{56}Mn_{18}Ga_{26}$ and $Ni_{54}Mn_{20}Ga_{26}$ alloys.

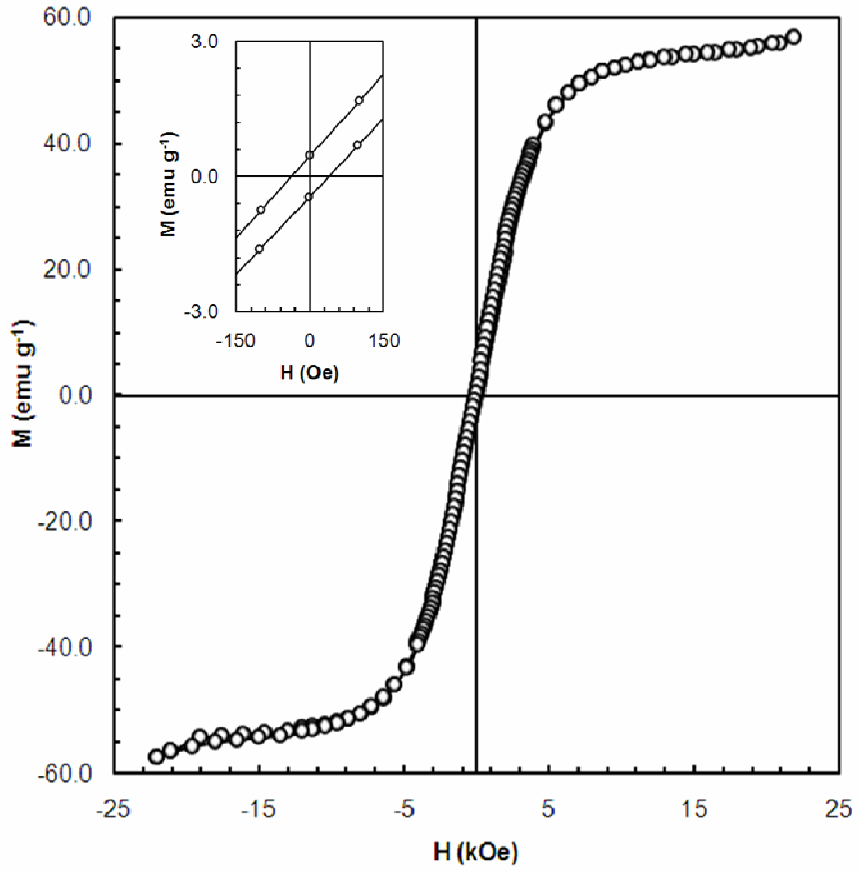

Figure 6.24 Hysteresis loop for the as-cast $Ni_{49}Mn_{25}Ga_{26}$ alloy measured at RT, inset shows the hysteresis in more detail.

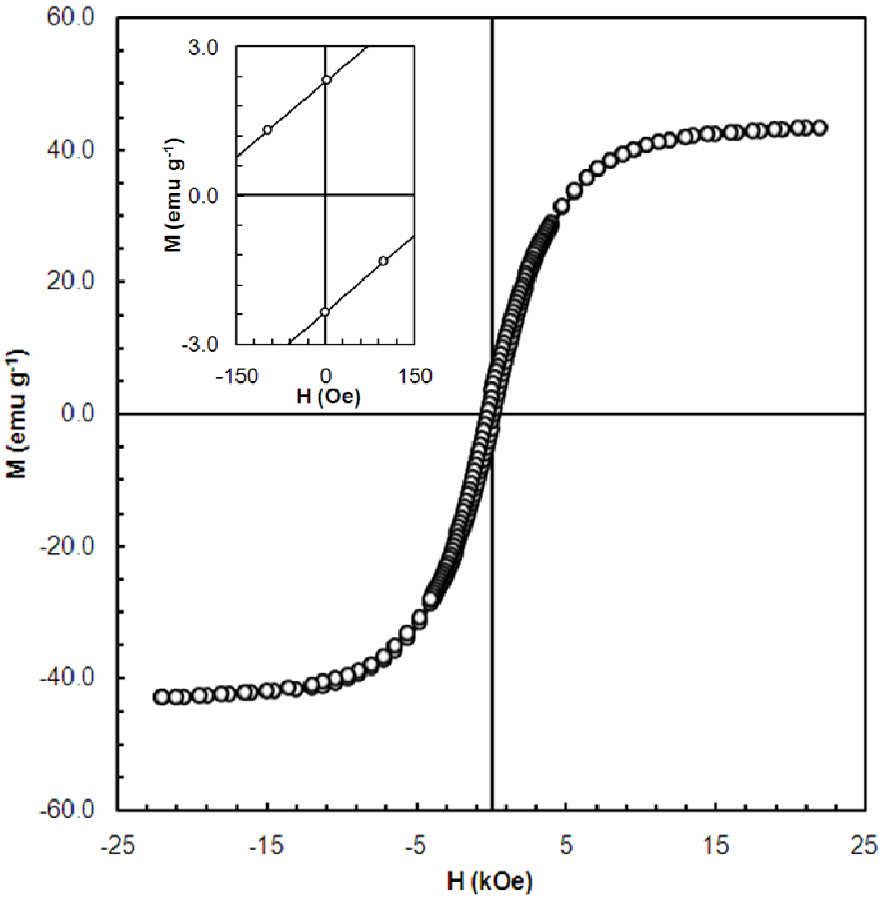

Figure 6.25 Hysteresis loop for the as-cast $Ni_{54}Mn_{20}Ga_{26}$ alloy measured at RT, inset shows the hysteresis in more detail.

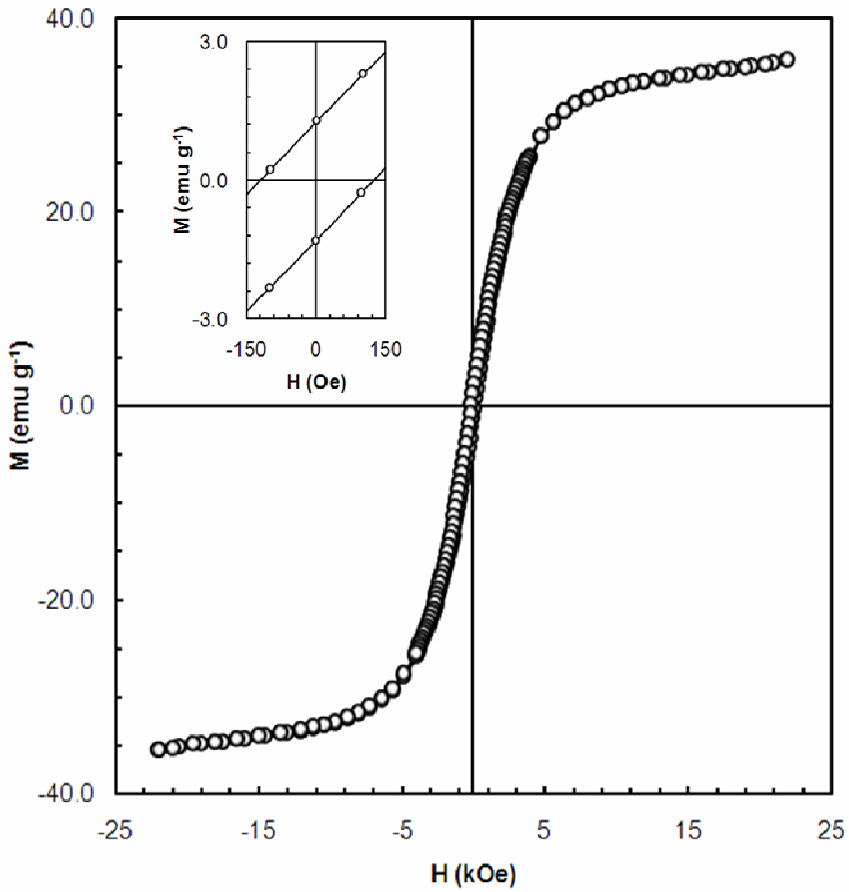

Figure 6.26 M-H curve for the as received $Ni_{56}Mn_{18}Ga_{26}$ alloy measured at RT, inset shows the hysteresis in more detail.

In Figure 6.27, saturation magnetization (M_{sat}) is given as function of excess Ni, x (at.%), in $Ni_{49+x}Mn_{25-x}Ga_{26}$ (x=0,5 and 7) alloys. It is evident from Figure 6.27 that, M_{sat} decreases with the substitution of Mn with Ni in $Ni_{49+x}Mn_{25-x}Ga_{26}$ (x=0,5 and 7) alloys. This is understandable since Mn atoms have a large magnetic moment (4 μ_B) [80, 134] and decreasing the Mn content results in the dilution of the magnetic subsystem.

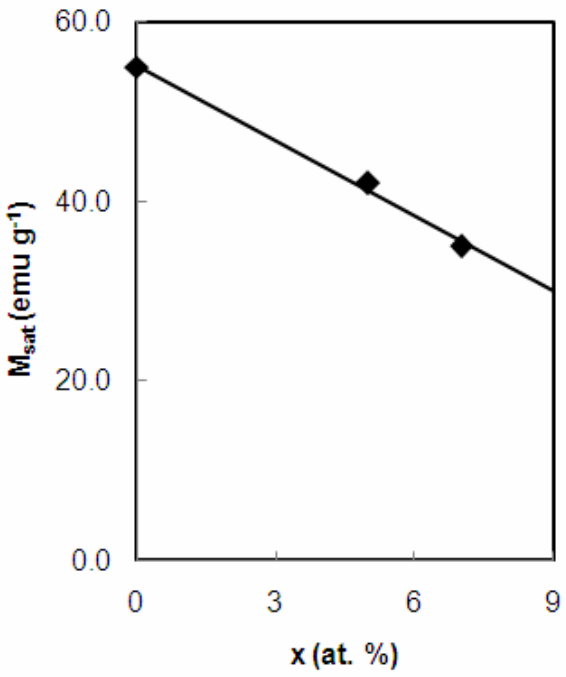

Figure 6.27 M_{sat} versus x for $Ni_{49+x}Mn_{25-x}Ga_{26}$ (x=0, 5 and 7) alloys.

Magnetization is given as a function of temperature for the as-cast $Ni_{49+x}Mn_{25-x}Ga_{26}$ (x= 0, 5 and 7) alloys in Figures 6.28-6.30 respectively. Analysis of magnetization versus temperature data point out that, as-cast $Ni_{49}Mn_{25}Ga_{26}$ alloy undergoes sequential phase transitions. It is evident from Figure 6.28 that, heating data do not retrace the cooling data but exhibit a narrow hysteresis near 200 K, indicating the occurrence of a first order transition. First order martensitic transitions from the cubic to tetragonal or orthorombic crystal structure were reported to occur in Ni-Mn-Ga alloys [80, 88, 89] and at the first order transition temperature, there is a jump in thermodynamical properties like magnetization. It can be concluded from the data shown in Figure 6.28 that, a structural transition occurs near 200 K from the cubic $L2_1$ phase to the low symmetry martensitic phase. P.J. Webster et al. reported for the stoichiometric Ni_2MnGa alloy a martensitic transformation temperature of 202 K [80]. Similar to the Ni_2MnGa alloy, near stoichiometric $Ni_{49}Mn_{25}Ga_{26}$ alloy undergoes a martensitic transition in the ferromagnetic state. It can be seen from Figure 6.28 that, the magnetization of the as-cast $Ni_{49}Mn_{25}Ga_{26}$ alloy drops instantaneously to values close to zero near 377 K. It was reported that stoichiometric Ni_2MnGa alloy undergoes a magnetic phase transition from ferromagnetic to paramagnetic phase at 376 K [80]. The $Ni_{49}Mn_{25}Ga_{26}$ alloy has a similar composition with the Ni_2MnGa alloy; therefore, it can be assumed that as-cast $Ni_{49}Mn_{25}Ga_{26}$ alloy undergoes a transition from the magnetically ordered ferromagnetic state to the magnetically disordered paramagnetic state at 377 K. The heating and cooling curves of the as-cast Ni_2MnGa alloy (Figure 6.28) do not display hysteresis in 300 K<T<450 K within experimental uncertainty. The magnetic transition around 377 K is of second order, which explains the absence of the hysteresis. As a result, the near stoichiometric $Ni_{49}Mn_{25}Ga_{26}$ alloy undergoes a low temperature first order martensitic transition around 200 K and a second order magnetic transition (ferromagnetic↔paramagnetic) near 377 K.

It can be seen from Figures 6.29 and 6.30 that the magnetic transition in $Ni_{54}Mn_{20}Ga_{26}$ and $Ni_{56}Mn_{18}Ga_{26}$ alloys have characteristics typical of a first order magneto-structural transition because of the following reasons. The magnetization

of as-cast $Ni_{54}Mn_{20}Ga_{26}$ and $Ni_{56}Mn_{18}Ga_{26}$ alloys drops significantly from high values to nearly zero. As shown in Figures 6.29 and 6.30, $Ni_{54}Mn_{20}Ga_{26}$ and $Ni_{56}Mn_{18}Ga_{26}$ alloys are ferromagnetic at RT and a significant decrease in magnetization near T_C is expected to occur in these alloys. Therefore, the decrease in magnetization at around 345 K for $Ni_{54}Mn_{20}Ga_{26}$ alloy (Figure 6.29) and 330 K for $Ni_{56}Mn_{18}Ga_{26}$ alloy (Figure 6.30) can be attributed to the ferromagnetic ↔paramagnetic transition. But unlike the ferromagnetic↔paramagnetic transition observed in $Ni_{49}Mn_{25}Ga_{26}$ at around 377 K (Figure 6.28), a marked hysteresis is associated with the transition in the as-cast $Ni_{54}Mn_{20}Ga_{26}$ and $Ni_{56}Mn_{18}Ga_{26}$ alloys (Figures 6.29 and 6.30). It was previously mentioned that heating and cooling data follow different paths for the $Ni_{49}Mn_{25}Ga_{26}$ alloy near the martensitic transition (~200 K). A similar hysteretic feature is observed in cooling and heating data for the $Ni_{54}Mn_{20}Ga_{26}$ and $Ni_{56}Mn_{18}Ga_{26}$ alloys in Figures 6.29 and 6.30. This indicates the occurrence of a first order transition near 345 K and 330 K for the $Ni_{54}Mn_{20}Ga_{26}$ and $Ni_{56}Mn_{18}Ga_{26}$ alloys, respectively. At RT, the $Ni_{54}Mn_{20}Ga_{26}$ and $Ni_{56}Mn_{18}Ga_{26}$ alloys have tetragonal $L1_0$-type structure determined by XRD (Figure 6.23) and it is assumed that the low symmetry $L1_0$-type structure transforms to a high symmetry $L2_1$-type structure as a result of the first order martensitic transformation around 345 K and 330 K for the $Ni_{54}Mn_{20}Ga_{26}$ and $Ni_{56}Mn_{18}Ga_{26}$ alloys, respectively. The relatively high temperature $L2_1$-type structure could not be confirmed with XRD measurements because of the absence of a temperature control unit in the diffractometer employed in this investigation. Consequently, it can be assumed that magnetic and martensitic transformations merge and a ferromagnetic ($L1_0$)↔paramagnetic ($L2_1$) transformation occurs around 345 K and 330 K in the $Ni_{54}Mn_{20}Ga_{26}$ and $Ni_{56}Mn_{18}Ga_{26}$ alloys, respectively. Coupling of structural and magnetic phase transitions similar to the ones observed in this study were reported for various Ni-rich Heusler alloys [7].

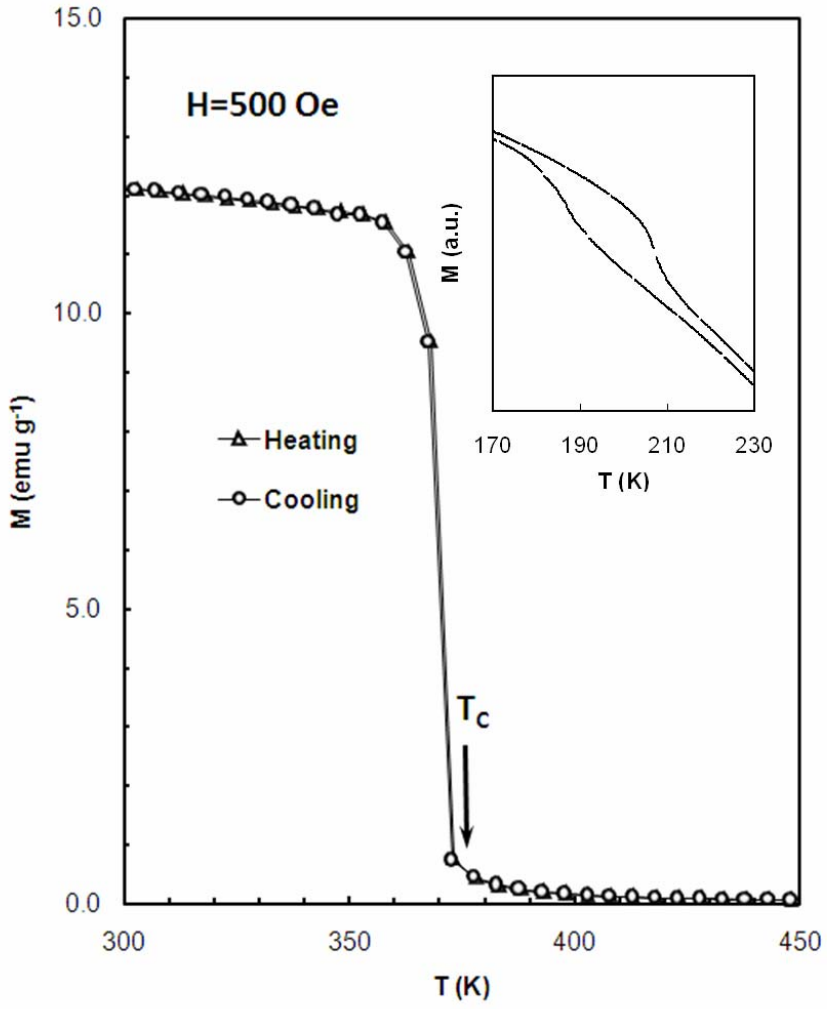

Figure 6.28 Temperature dependence of magnetization measured during cooling for the as-cast $Ni_{49}Mn_{25}Ga_{26}$ alloy under a constant magnetic field of 500 Oe.

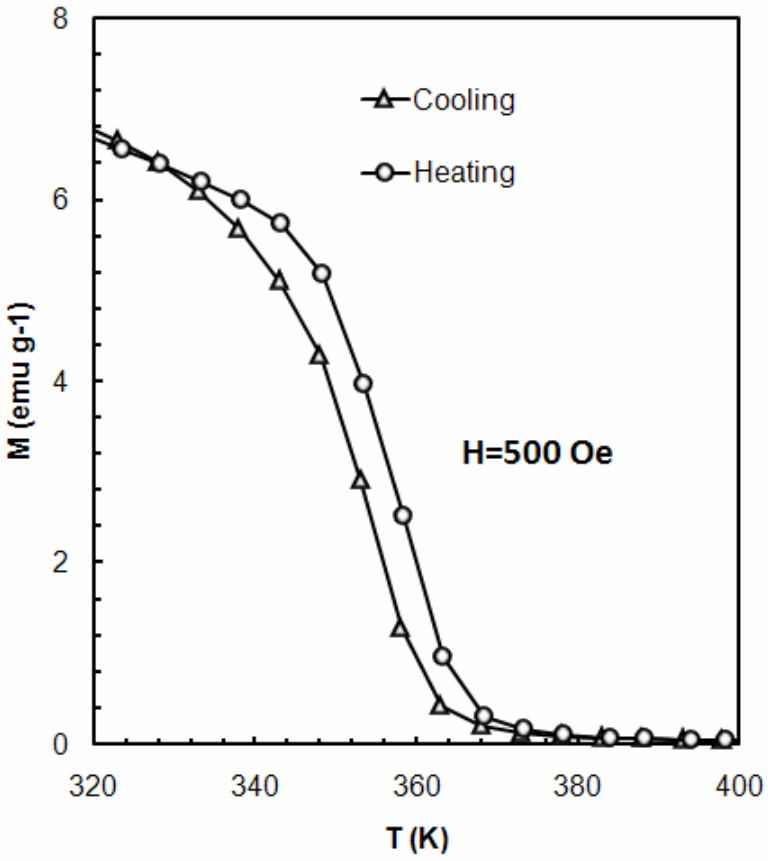

Figure 6.29 Temperature dependence of magnetization for the as-cast $Ni_{54}Mn_{20}Ga_{26}$ alloy under a constant magnetic field of 500 Oe.

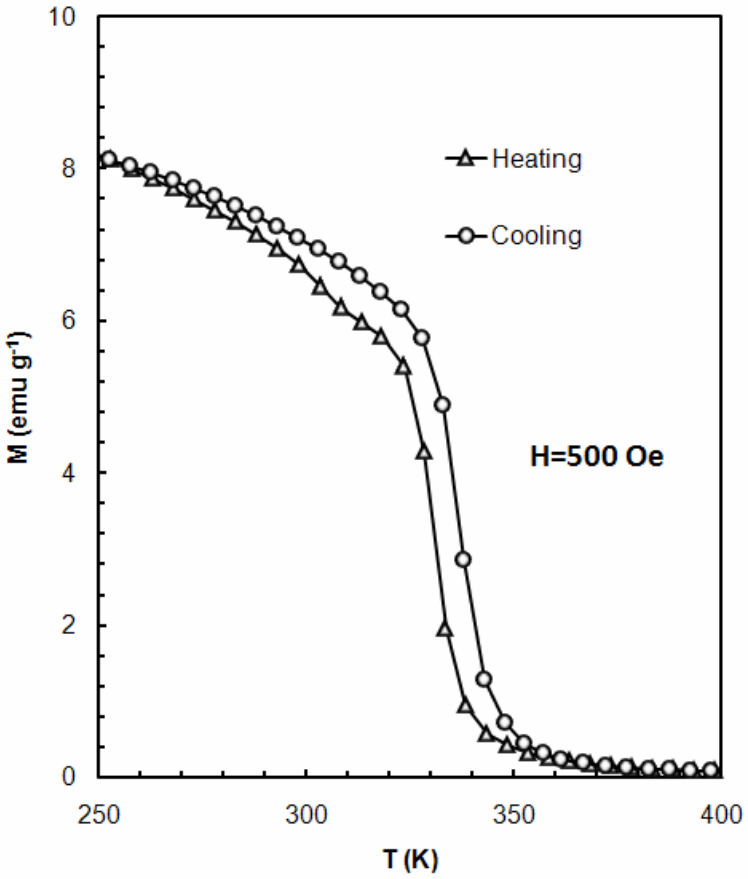

Figure 6.30 Temperature dependence of magnetization for the as-cast $Ni_{56}Mn_{18}Ga_{26}$ alloy under a constant magnetic field of 500 Oe.

6.2.1.3. Magnetocaloric effect in $Ni_{49+x}Mn_{25-x}Ga_{26}$ (x=5 and 7) Heusler alloys

In order to calculate ΔS_M values around the coupled martensitic and magnetic transformations (magneto-structural transformation); isothermal M-H measurements were performed. It is evident from Equation (2.13) that, ΔS_M is directly proportional to $(\partial M/\partial T)$. The greatest change in magnetization with respect to temperature is expected to occur at the magneto-structural transition, therefore, the ΔS_M values are calculated in the vicinity of this transition.

Figures 6.31 and 6.32 show the isothermal M-H curves measured for the $Ni_{54}Mn_{20}Ga_{26}$ and $Ni_{56}Mn_{18}Ga_{26}$ alloys, respectively. The M-H curves were acquired in 2K steps in applied fields up to 22 kOe. Samples were heated above T_C prior to each measurement in order to achieve demagnetization. A paramagnetic↔ferromagnetic transition is observed in Figures 6.31 and 6.32 for the as-cast $Ni_{54}Mn_{20}Ga_{26}$ and $Ni_{56}Mn_{18}Ga_{26}$ alloys, respectively. At high temperatures M-H curves are linear and magnetization values are relatively small. Upon cooling there is a marked increase in magnetization values. Another point worth mentioning is that, there is a significant increase in the curvature of the M-H curves upon cooling.

It is interesting to note that, there is a change of slope near 9 kOe for the M-H curves measured in 340 K<T<360 K for $Ni_{54}Mn_{20}Ga_{26}$ (Figure 6.31) and in 361 K<T<387 K for $Ni_{56}Mn_{18}Ga_{26}$ (Figure 6.32) alloys. Some of the intermetallic compounds which undergo magneto-structural transitions were reported to exhibit pronounced anomalies on isothermal M-H curves [135]. This characteristic feature is attributed to magnetic field induced magneto-structural transition. Similar features, which point out the first order characteristic of the magnetic transition were reported for Ni-Mn-Ga [9] and Gd-Si-Ge [32, 136] compounds.

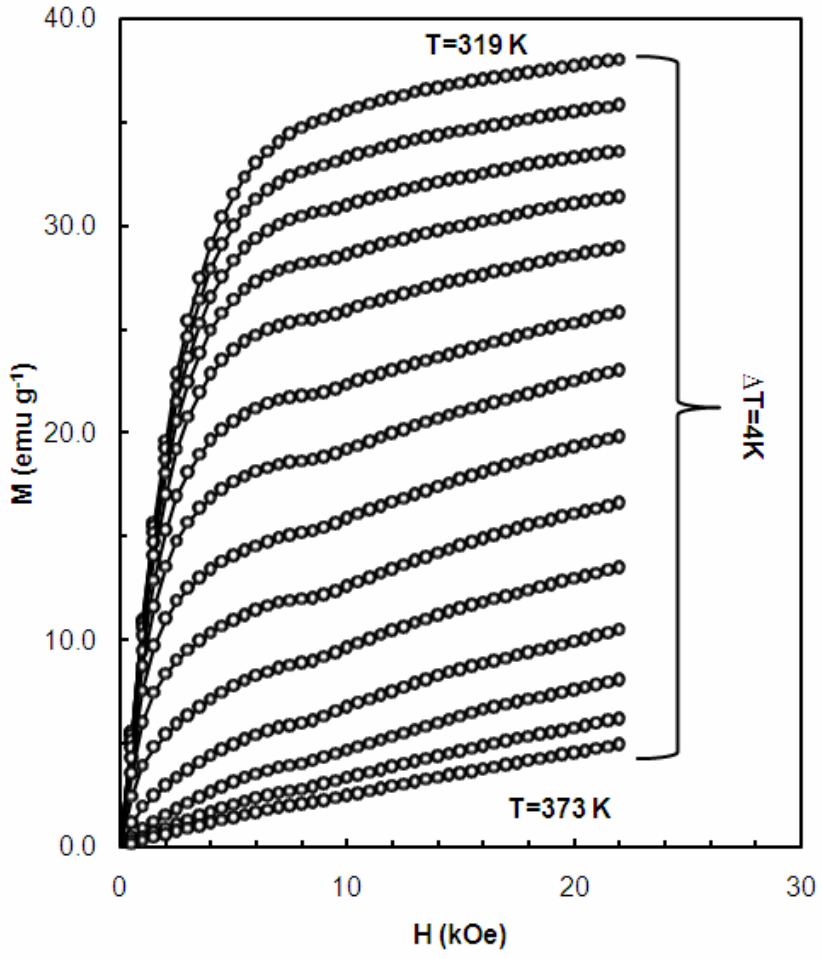

Figure 6.31 Magnetization of the as-cast $Ni_{54}Mn_{20}Ga_{26}$ alloy as a function of magnetic field measured in the temperature interval of 319 K<T<373 K, ΔT=4K for clarity.

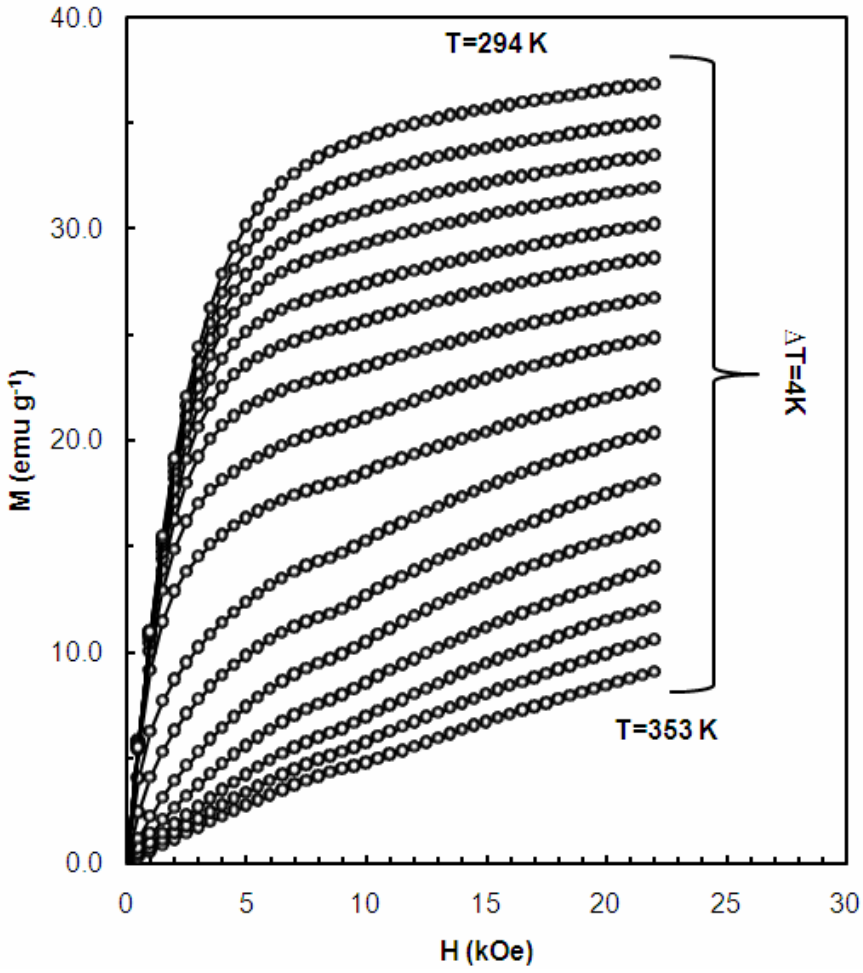

Figure 6.32 Magnetization of the as-cast $Ni_{56}Mn_{18}Ga_{26}$ alloy as a function of magnetic field measured in the temperature interval of 294 K to 353 K, ΔT=4K for clarity.

The isothermal M-H curves measured for the $Ni_{54}Mn_{20}Ga_{26}$ (Figure 6.31) and $Ni_{56}Mn_{18}Ga_{26}$ (Figure 6.32) alloys were used to estimate the ΔS_M values as a function of temperature for these alloys, as described in the Chapter 2. The ΔS_M dependencies on temperature was calculated by using Equation (2.13) in a magnetic field change of ΔH=22 kOe. ΔS_M is given as a function of temperature in the vicinity of the magneto-structural transition for the as-cast $Ni_{54}Mn_{20}Ga_{26}$ and $Ni_{56}Mn_{18}Ga_{26}$ alloys in Figures 6.33 and 6.34 respectively. It is evident from Figure 6.33 and 6.34 that ΔS_M has its maximum near 345 K and 330 K for the $Ni_{54}Mn_{20}Ga_{26}$ and $Ni_{56}Mn_{18}Ga_{26}$ alloys. These temperatures coincide with the magneto-structural transitions temperatures of these alloys. The maximum values of $|\Delta S_M|$ are determined as 1.84 $JKg^{-1}K^{-1}$ and 1.67 $JKg^{-1}K^{-1}$ for $Ni_{54}Mn_{20}Ga_{26}$ and $Ni_{56}Mn_{18}Ga_{26}$ alloys, respectively. A.A. Cherechukin et al. reported that besides the saturation magnetization, $|\Delta S_M|$ is also correlated by the Mn content [7]. It is noteworthy that $|\Delta S_M|$ decreases ~9% with a decrease in Mn content by 2 at. % for $Ni_{54}Mn_{20}Ga_{26}$ and $Ni_{56}Mn_{18}Ga_{26}$ alloys.

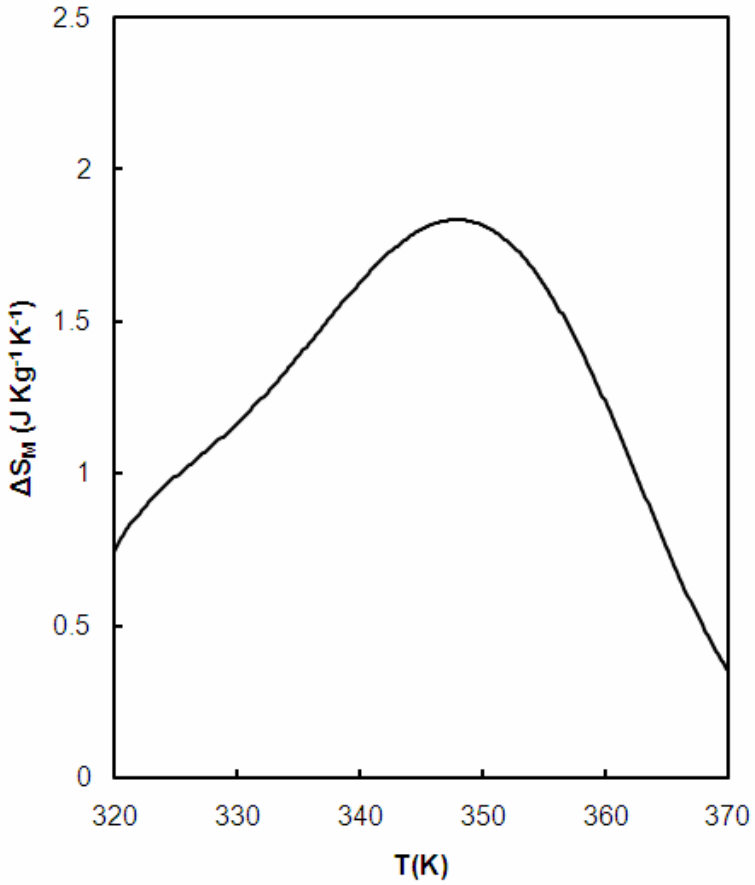

Figure 6.33 Magnetic entropy change of the as-cast $Ni_{54}Mn_{20}Ga_{26}$ alloy as a function of temperature.

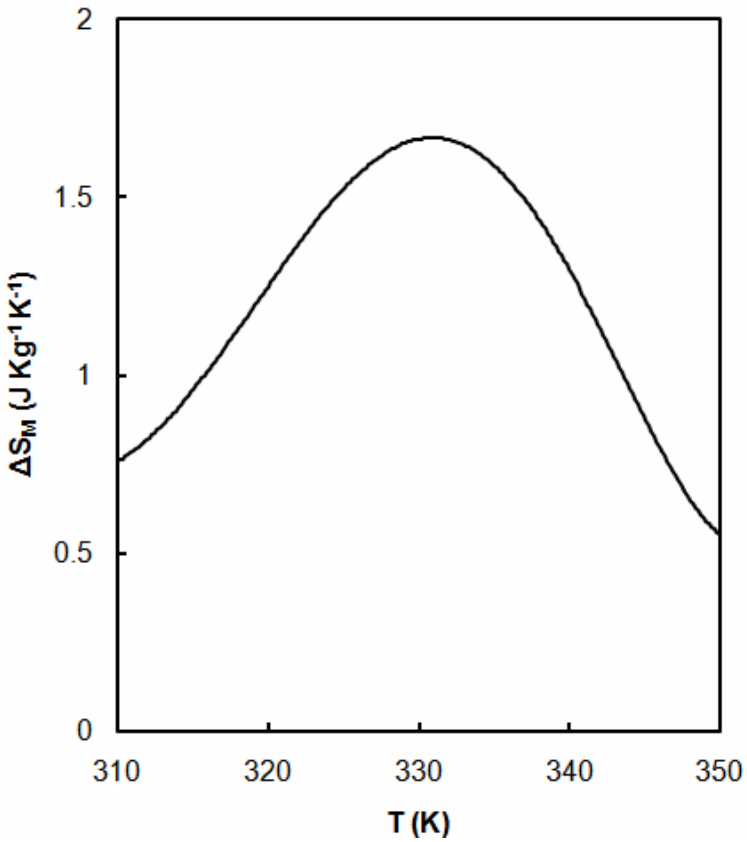

Figure 6.34 Magnetic entropy change of the as-cast $Ni_{56}Mn_{18}Ga_{26}$ alloy as a function of temperature.

6.2.2. Magnetic and Structural Properties of Ni-Mn-Al Heusler Alloys

In this chapter, experimental results and their discussion are presented for the ternary (Ni-Mn-Al) and binary (Ni-Al and Ni-Mn) alloys. The compositions of the investigated Ni-Mn-Al Heusler alloys determined by general EDS analyses are given in Table 6.7 together with calculated lattice parameters and e/a values. The e/a values were calculated by using Equation (4.2).

For all the investigated Ni-Mn-Al alloys, composition of Ni was kept constant at 50 at. % due to the following reasons. To obtain a fully ordered $L2_1$ phase, firstly nearest neighbour ordering must be fulfilled. In order to establish nearest neighbour ordering ,in other words, stabilize B2 phase, ordering at the Ni sublattice should be accomplished. This means that all the corner lattice sites that form the Ni sublattice should be occupied by Ni atoms. That is possible in only alloys where half of the atoms are Ni. Furthermore, near the β phase region, only A2, B2 and $L2_1$-type ordered structures may appear, other complex ordered structures like the $D0_3$-type structure is inconceivable for this composition range. The Al content, x, ranged from 10 to 40 at. % for the $Ni_{50}Mn_{50-x}Al_x$ alloys. Substitution of Al for Mn does not affect the volume of the unit cell. Therefore calculated lattice parameters for the cubic structure have identical values , which are consistent with the reported values [106, 112].

Table 6.7 Compositions, lattice constants (a,b and c) and e/a for investigated Ni-Mn-Al alloys.

Nominal Composition	Ni (at.%)	Mn (at.%)	Al (at.%)	a=b (Å)	c (Å)	e/a
$Ni_{50}Mn_{50}$	49.59	50.41	-	3.715	3.525	8.49
$Ni_{50}Al_{50}$	49.74	-	50.26	2.88	-	6.48
$Ni_{50}Mn_{25}Al_{25}$	50.11	24.90	24.99	5.5819	-	7.50
$Ni_{50}Mn_{20}Al_{30}$	49.97	19.8	30.23	5.5819	-	7.29
$Ni_{50}Mn_{30}Al_{20}$	49.81	29.85	20.34	5.5819	-	7.68
$Ni_{50}Mn_{40}Al_{10}$	49.75	39.97	10.28	7.54	6.84	8.08

$Ni_{50}Mn_{50}$, $Ni_{50}Mn_{30}Al_{20}$ and $Ni_{50}Mn_{40}Al_{10}$ alloys were reported to undergo martensitic transformation upon cooling [106]. A schematic representation of the martensitic transformation from the high symmetry cubic B2 phase to the low symmety $L1_0$ phase is presented in Figure 6.35.

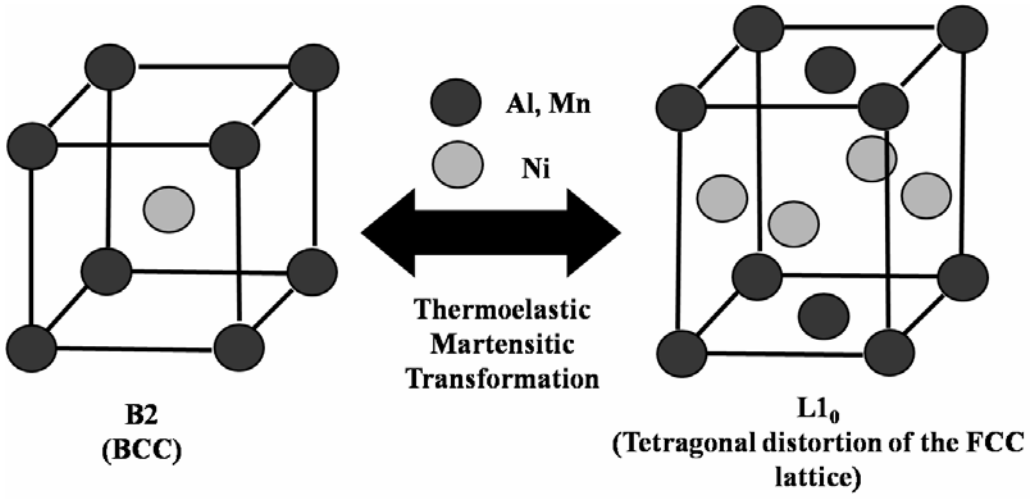

Figure 6.35 Martensitic transformation from the high symmetry B2 phase to the low symmetry $L1_0$ phase.

Ni-Mn-Ga and $Ni_{50}Mn_{50-x}Al_x$ ($20<x<30$) alloys have a large temperature interval between liquidus and solidus, which upon rapid solidification results in similar dendritic structures [137]. The dendritic microstructure of the as-cast Ni_2MnAl is given in Figure 6.36 as an example of the dendritic microstructures observed in $Ni_{50}Mn_{50-x}Al_x$ ($20<x<30$) alloys. The $Ni_{50}Mn_{50}$ and $Ni_{50}Mn_{40}Al_{10}$ alloy have similar martensitic microtructures. SEM images of the as-cast NiMn and $Ni_{50}Mn_{40}Al_{10}$ alloys are given in Figure 6.37 and 6.38.

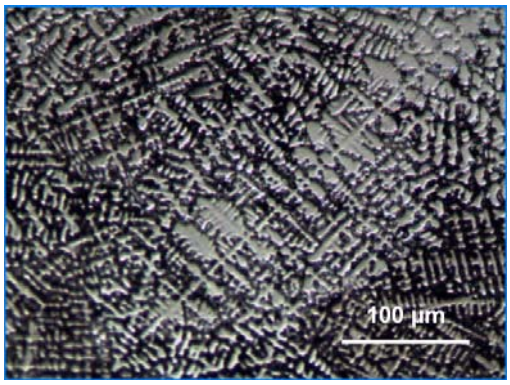

Figure 6.36 Optical microscopy image of the middle region of as-cast Ni_2MnAl alloy.

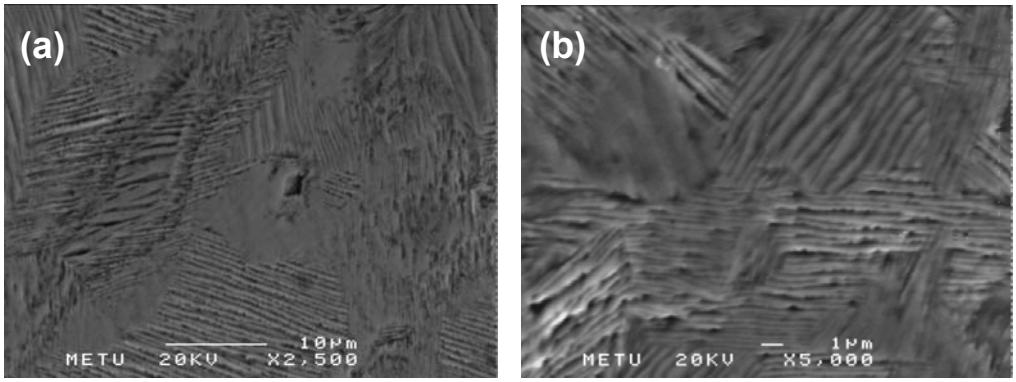

Figure 6.37 SEM images of the the middle region of as-cast $Ni_{50}Mn_{40}Al_{10}$ alloy**.**

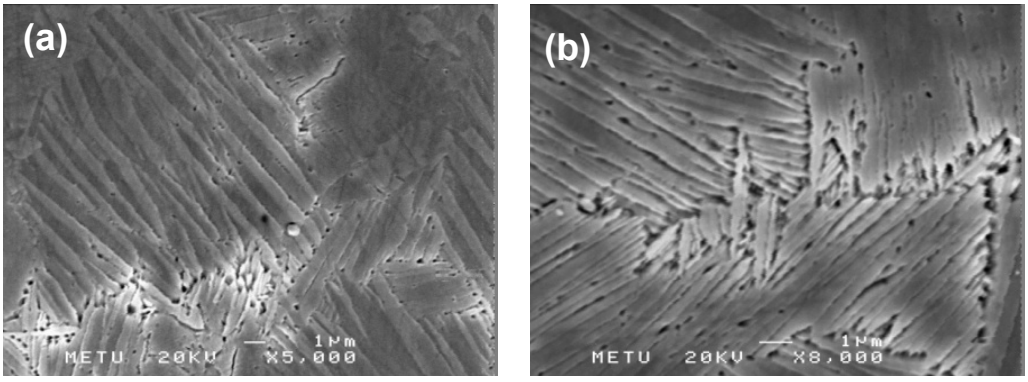

Figure 6.38 SEM images of the middle region of as-cast $Ni_{50}Mn_{50}$ alloy.

6.2.2.1. Effects of Composition and Aging on the Crystal Structures and Atomic Ordering in $Ni_{50}Mn_{50-x}Al_x$ (x=10, 20, 25, 30) Alloys

XRD measurements were performed to determine the effect of aging at 660 K for 12, 24 and 48 days on atomic ordering and crystal structure in $Ni_{50}Mn_{50-x}Al_x$ (x=10, 20, 25, 30) alloys. The RT XRD patterns of the as-cast and aged $Ni_{50}Mn_{50-x}Al_x$ (x=10, 20, 25, 30) alloys are shown in Figures 6.39-6.41. Similar to Ni-Mn-Ga alloys, the superlattice peaks were not observed in some cases and the intensities of several fundamental reflections are not in proportion because of the texturing in the polycrystalline Ni-Mn-Al alloys.

The XRD pattern of the Ni_2MnAl (Figure 6.39) and $Ni_{50}Mn_{20}Al_{30}$ (Figure 6.40) alloys can be indexed according to the $L2_1$-type crystal structure (space group: Fm3m) with identical lattice parameters. For the as-cast Ni_2MnAl alloy, peaks associated with the fully disordered A2 phase are present. Upon aging at 660 K there is a development of the ordering in the Ni sublattice, indicated by the emergence of (200) and (222) reflections which belong to the ordered B2 phase in the Ni_2MnAl alloy. It is evident from Figure 6.39 that for the 24 day-aged Ni_2MnAl alloy, the intensities of both the (200) and the (222) reflections related to the ordered B2 phase appear with relatively high intensities which can be taken as an indication of the development of further ordering between Ni atoms at the Ni sublattice. The XRD pattern of the 24 day-aged Ni_2MnAl alloy is given in Figure 6.43 for a more detailed analysis of the low intensity superlattice peaks. In addition to the ordering that occurred at the Ni sublattice, in the 24 day-aged Ni_2MnAl alloy further ordering took place at the Mn-Al sublattice, pointed out by the emergence of the (331) peak. The $L2_1$ phase is definitely present in 24 and 48 day-aged Ni_2MnAl alloys but the XRD data alone is not sufficient to make a conclusion about whether the $L2_1$ phase is single or a mixture of $L2_1$ and B2 phases are present.

Among the investigated Ni-Mn-Al Heusler alloys only the $Ni_{50}Mn_{20}Al_{30}$ alloy has the B2 phase in the as-cast state. As shown in Figure 6.40, the RT XRD pattern for

the as-cast $Ni_{50}Mn_{20}Al_{30}$ alloy has the (200) and (222) superlattice peaks related to the ordered B2 phase and the intensities of these peaks are higher for the 24 and 48 day-aged $Ni_{50}Mn_{20}Al_{30}$ alloys. The $Ni_{50}Mn_{20}Al_{30}$ alloy has the B2 phase in as-cast state but further ordering could not be obtained in this alloy by low temperature aging because of the deviation from stoichometry. Perfect order can only be achieved for the stoichiometric alloys since in the off-stoichiometric $Ni_{50}Mn_{20}Al_{30}$ alloy, all the Ni atoms can be at the original lattice sites of the Ni atoms but there will be Al atoms at Mn sites at all times.

In the XRD pattern of the as-cast $Ni_{50}Mn_{30}Al_{20}$ alloy shown in Figure 6.41, there is a splitting of the (220) peak and other fundamental peaks related to the A2 phase appear with very low intensities. The splitting of the fundamental (220) peak points out the loss of symmetry of the crystal structure. R. Kainuma et al. reported for this composition that prior to the martensitic transformation (M_s= 251 K, A_f=269 K) a premartensitic transition (M_s=292 K, A_f=295 K) occurs on cooling in this alloy and between martensitic and premartensitic transition temperatures there is an ‘‘Intermediate martensite phase with a slightly distorted B2 structure’’[106]. The XRD pattern for the $Ni_{50}Mn_{30}Al_{20}$ alloy (Figure 6.41) matches this definition, all the peaks related to the A2 phase are present and loss of symmetry is indicated by the splitting of the (220) peak. The XRD pattern for the $Ni_{50}Mn_{30}Al_{20}$ alloy can be indexed according to the distorted $L2_1$-type crystal structure. Formation of this metastable phase can be explained through, the temperature of the copper tray of arc melter which was kept at 290 K during the melting of this alloy. There was a quenching effect from elevated temperatures to 290 K associated to the very rapid cooling which explains the formation of the intermediate phase in the $Ni_{50}Mn_{30}Al_{20}$ alloy.

$Ni_{50}Mn_{40}Al_{10}$ alloy has the highest e/a (8.08) ratio among the investigated Ni-Mn-Al alloys. As stated in literature review, it was well established that M_s increases with increasing e/a values. Therefore the most unstable cubic structure among the investigated ternary Ni-Mn-Al alloys is the $Ni_{50}Mn_{40}Al_{10}$ alloy. The $Ni_{50}Mn_{40}Al_{10}$

has a martensitic structure at RT which is a confirmed by XRD (Figure 6.42) and SEM (Figure 6.37). The XRD patterns for the $Ni_{50}Mn_{40}Al_{10}$ alloy given in Figure 6.42 can be indexed according to the $L1_0$ -type crystal structure (space group: P4/mmm). Calculated lattice parameters (a=b=7.56 Å and c=6.86 Å) are close to the ones reported by R. Kainuma et al. for nearly the same composition ($L1_0$; a=b= 7.54 Å, c=6.84 Å) [106]. The intensities of the peaks for the as-cast alloy does not differ as a result of aging and no additional peaks are observed in the XRD patterns of the aged $Ni_{50}Mn_{40}Al_{10}$ alloys. According to XRD data given in the Figure 6.42 only, low temperature aging at 660 K does not have a significant effect on the atomic ordering and crystal structure of the $Ni_{50}Mn_{40}Al_{10}$ alloy.

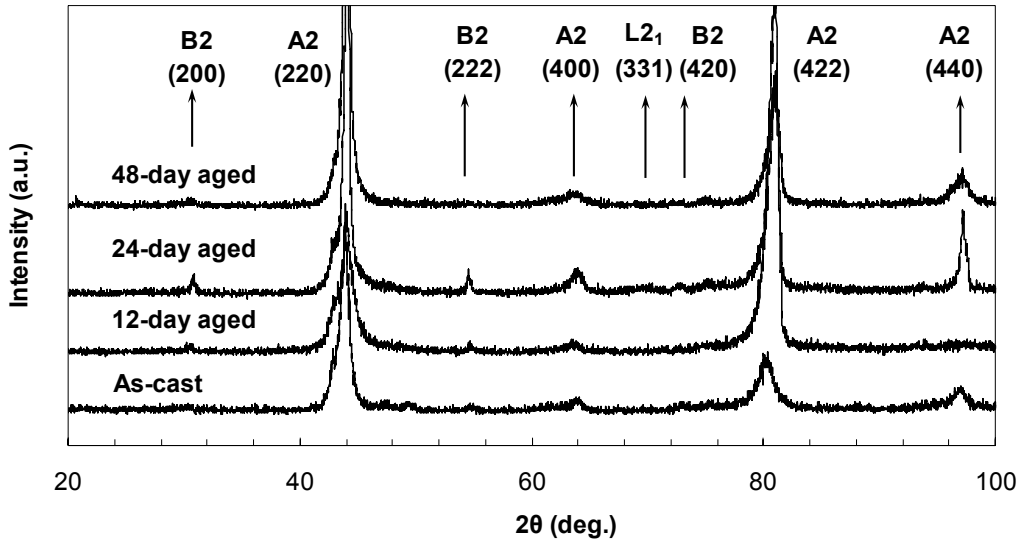

Figure 6.39 XRD patterns for the as-cast and aged Ni_2MnAl alloys measured at RT.

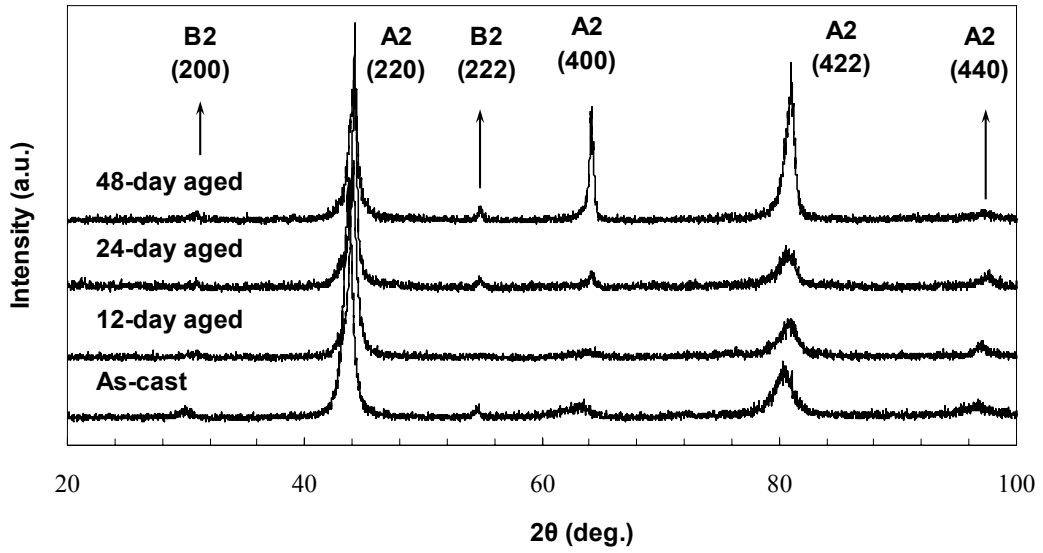

Figure 6.40 XRD patterns for the as-cast and aged $Ni_{50}Mn_{20}Al_{30}$ alloys measured at RT**.**

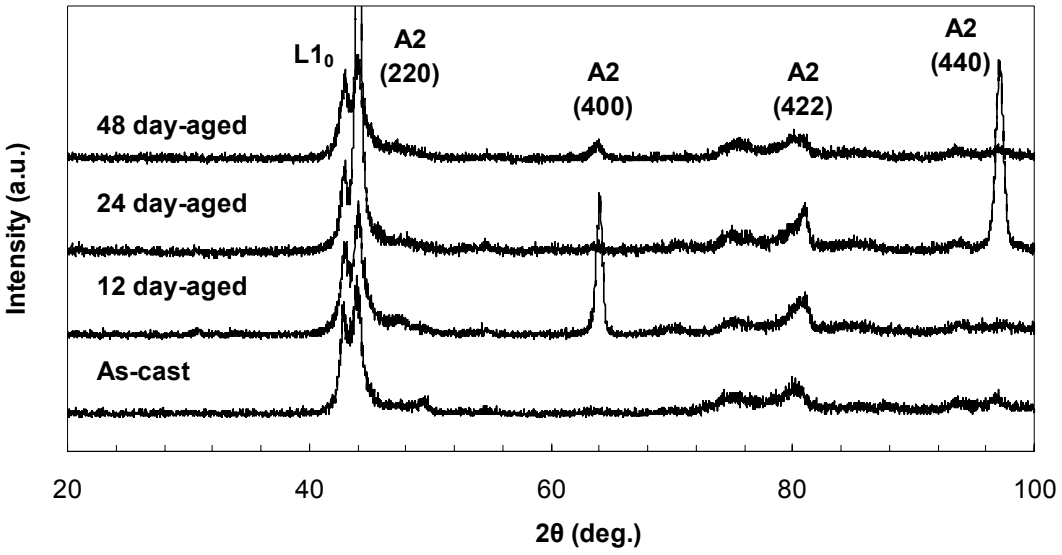

Figure 6.41 XRD patterns for the as-cast and aged $Ni_{50}Mn_{30}Al_{20}$ alloys measured at RT.

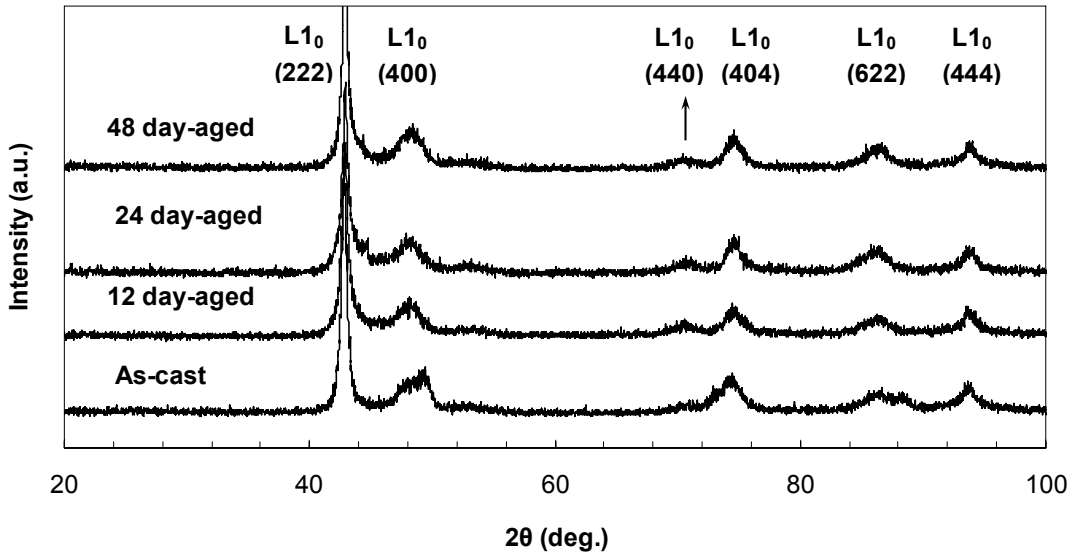

Figure 6.42 XRD patterns for the as-cast and aged $Ni_{50}Mn_{40}Al_{10}$ alloys measured at RT.

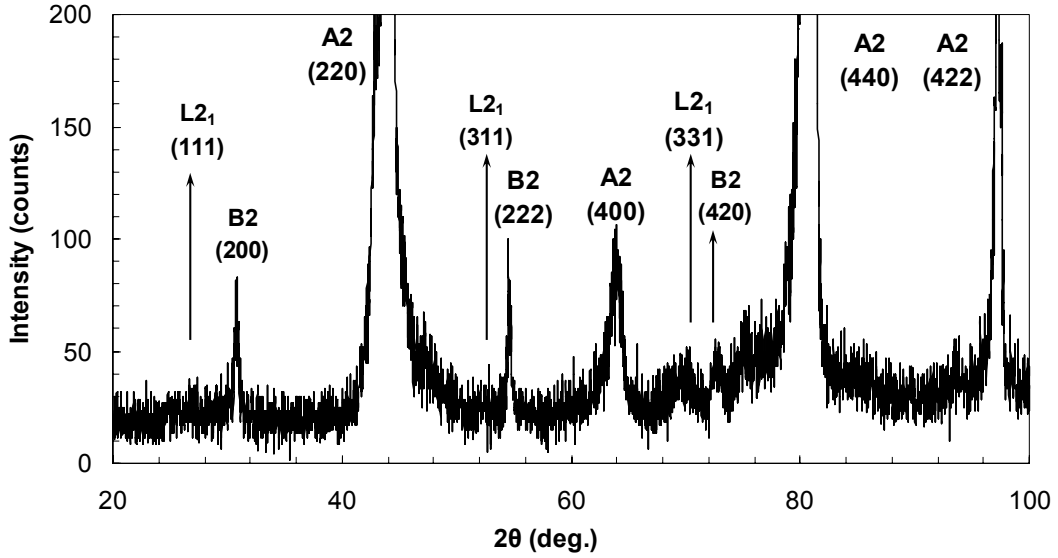

Figure 6.43 XRD pattern of the 24 day-aged Ni_2MnAl alloy measured at RT.

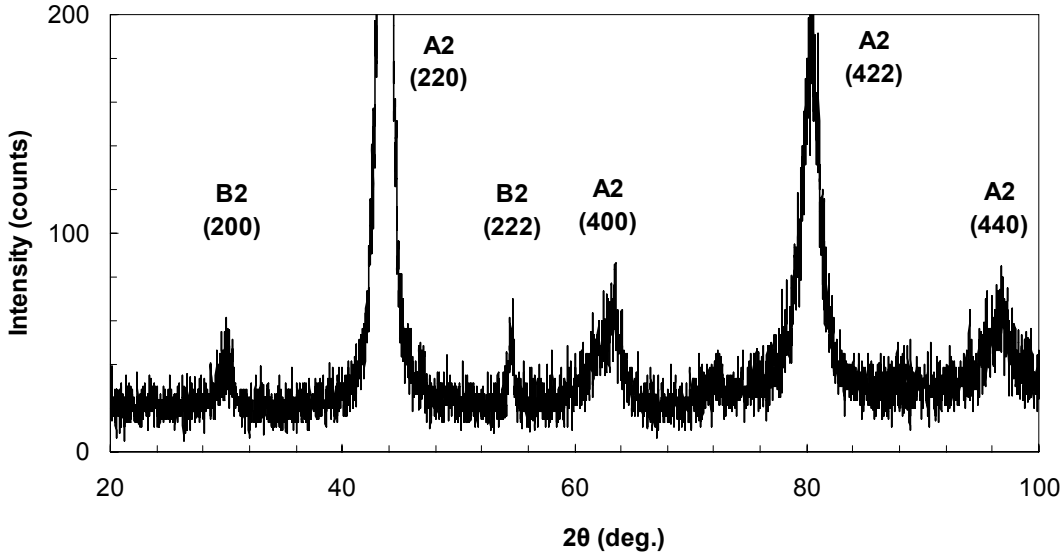

Figure 6.44 XRD pattern for the as-cast $Ni_{50}Mn_{20}Al_{30}$ alloy measured at RT.

6.2.2.2. Effects of Composition and Aging on the Magnetic Properties and Phase Transitions of $Ni_{50}Mn_{50-x}Al_x$ (x=10, 20, 25, 30) Alloys

Magnetic field and temperature dependence of magnetization for the as-cast and aged $Ni_{50}Mn_{50-x}Al_x$ (x=10, 20, 25, 30) alloys are measured in order to characterize the magnetic behaviour and phase transitions in these alloys.

Magnetization is given as a function of magnetic field for the as-cast and aged $Ni_{50}Mn_{50-x}Al_x$ (x=10, 20, 25, 30) alloys in Figures 6.45-6.48. M has a linear dependence of H for all the as-cast $Ni_{50}Mn_{50-x}Al_x$ (x=10, 20, 25, 30) alloys as shown in Figures 6.45-6.48. Furthermore, the magnetization values of the as-cast samples are significantly smaller than the aged samples in $Ni_{50}Mn_{50-x}Al_x$ (x=10, 20, 25, 30) alloys. This behaviour can result from paramagnetic and/or antiferromagnetic interactions for these alloys. In literature, paramagnetic behaviour was observed in M-H curves of Ni-Mn-Al alloys having the B2 phase due to the antiferromagnetic interactions between the Mn atoms [65, 112]. Conversely, the low temperature aged (~660 K) alloys having the $L2_1$ phase were reported to have a ferromagnetic-like behavior [65, 110]. Therefore, the linear dependence of M to H shown in Figures 6.45-6.48 results from the antifferomagnetism in the as-cast $Ni_{50}Mn_{50-x}Al_x$ (x=10, 20, 25, 30) alloys.

On the other hand, the M-H curves measured for the 12 day-aged $Ni_{50}Mn_{50-x}Al_x$ (x=10, 20, 25, 30) alloys (Figures 6.45-6.48) have considerable curvature. This curvature can be taken as an indication of ferromagnetic coupling. Under large magnetic fields, 12 day-aged samples have greater magnetization values than the as-cast samples but the magnetization of the 12 day-aged $Ni_{50}Mn_{50-x}Al_x$ (x=10, 20, 25, 30) alloys do not saturate even at 22 kOe and M-H curves have an explicit slope . As a result of aging at 660 K, there is a growing tendency of the magnetization of the 24 and 48 day-aged samples to saturate at high magnetic fields (Figures 6.45-6.48). The magnetization values for the 24 and 48 day-aged $Ni_{50}Mn_{50-x}Al_x$ (x=10, 20, 25, 30) alloys have slightly smaller values than the magnetization values of the

12 day-aged samples but the slope has decreased significantly for the 24 and 48 day-aged samples. However, the slopes of the M-H curves of 24 and 48 day-aged samples are still non-negligible and magnetization does not saturate at 22 kOe, suggesting that antiferromagnetic entity is still present in these alloys. Another resemblance among the $Ni_{50}Mn_{50-x}Al_x$ (x=10, 20, 25, 30) alloys is the overlapping of the M-H curves of the 24 day and 48 day-aged alloys. This can be attributed to the fact that further ordering at the Mn-Al sublattice has not developed significantly in that time period for the these alloys. This is also supported by XRD measurements, since there are no visible changes in the intensities of the peaks related to the $L2_1$ phase in these alloys (Figures 6.39-6.42).

In the off stoichiometric $Ni_{50}Mn_{40}Al_{10}$ alloy the probability of Mn atoms to be the nearest neighbors is greater than the Ni_2MnAl, $Ni_{50}Mn_{30}Al_{20}$ and $Ni_{50}Mn_{20}Al_{30}$ alloys due to the greater number of Mn atoms and nearly equiatomic binary Ni–Mn alloy is known to be antiferromagnetic. Therefore, based on these facts, a more pronounced antiferromagnetic behaviour is expected in the $Ni_{50}Mn_{40}Al_{10}$ alloy. Although XRD data for the $Ni_{50}Mn_{40}Al_{10}$ (Figure 6.42) suggests that there is no change in terms of atomic ordering for the aged $Ni_{50}Mn_{40}Al_{10}$ alloys, the M-H curve for the 12-day aged alloy has a slight curvature which becomes much more noticeable upon aging. The 24 and 48 day-aged alloys have curvature and hysteresis, indicating ferromagnetism is introduced in these alloys by low temperature aging but saturation of magnetization is not achieved. It is evident from comparison of the M-H curve of 48 day-aged $Ni_{50}Mn_{40}Al_{10}$ alloy with the M-H curves 48 day-aged $Ni_{50}Mn_{50-x}Al_x$ (x=20, 25 and 30) alloys that, magnetization in $Ni_{50}Mn_{40}Al_{10}$ alloy is the hardest to saturate and it is important to note that magnetization values are considerably lower than the $Ni_{50}Mn_{50-x}Al_x$ (x=20, 25 and 30) alloys. For the FSME to occur in the Ni-Mn-Al alloys, the alloy should be ferromagnetic in the martensitic phase. $Ni_{50}Mn_{40}Al_{10}$ alloy has a martensitic structure determined from the XRD patterns and ferromagnetism is introduced as a result of 24 day-aging at 660 K. Unlike Ni_2MnAl alloy, the ferromagnetic phase in $Ni_{50}Mn_{40}Al_{10}$ is not the cubic $L2_1$ phase but it can be concluded from XRD and

magnetic measurements that the atomic ordering similar to the one observed in Ni_2MnAl alloys generates ferromagnetism in the tetragonal $L1_0$ crystal structure.

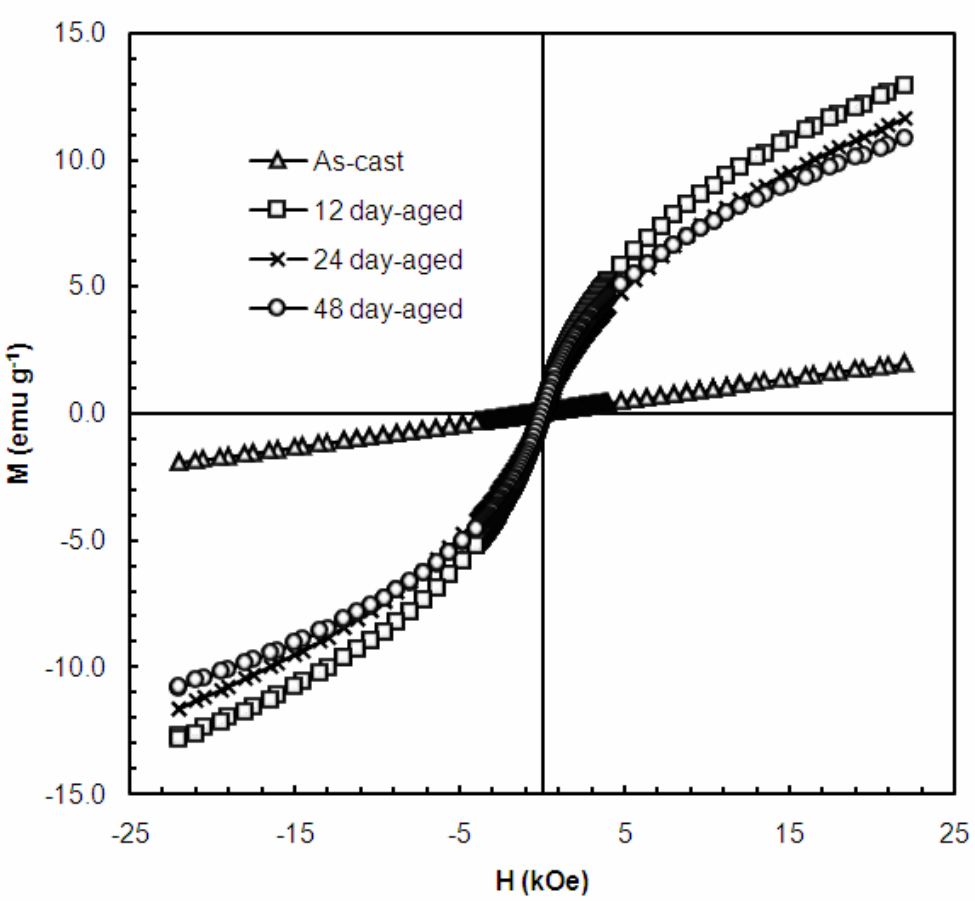

Figure 6.45 Hysteresis loops for the as-cast and aged Ni_2MnAl alloys measured at RT.

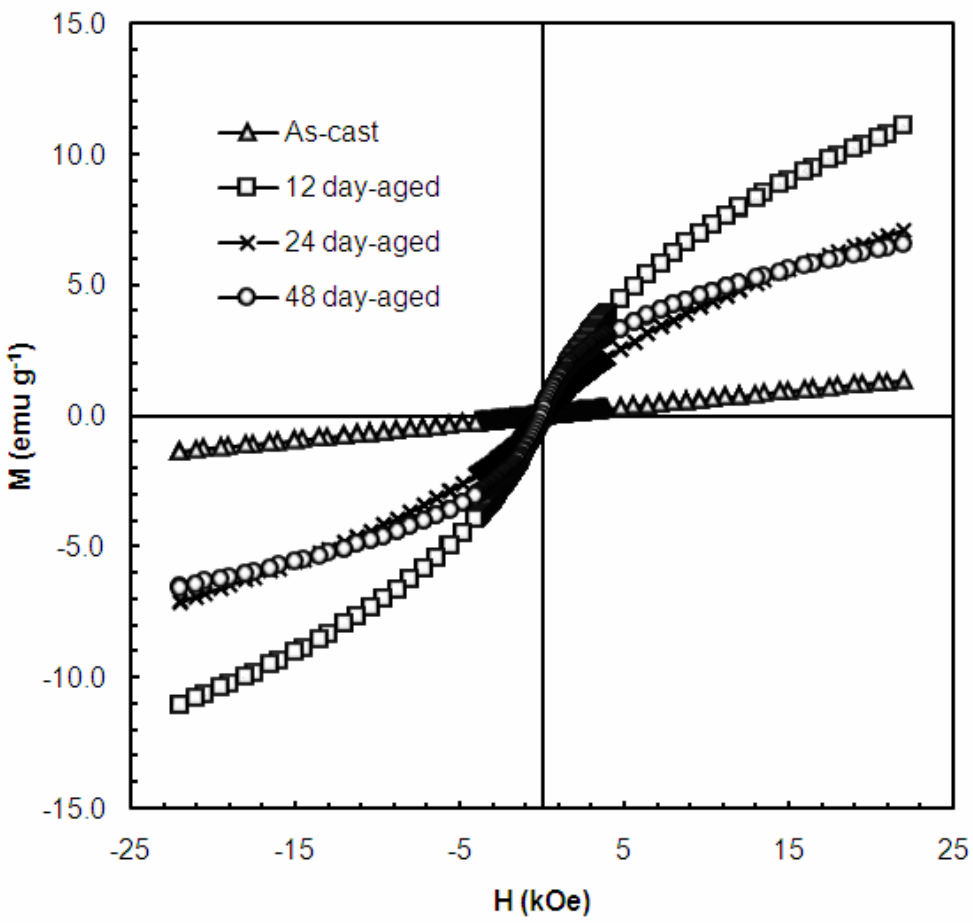

Figure 6.46 Hysteresis loops for the as-cast and aged $Ni_{50}Mn_{20}Al_{30}$ alloys measured at RT.

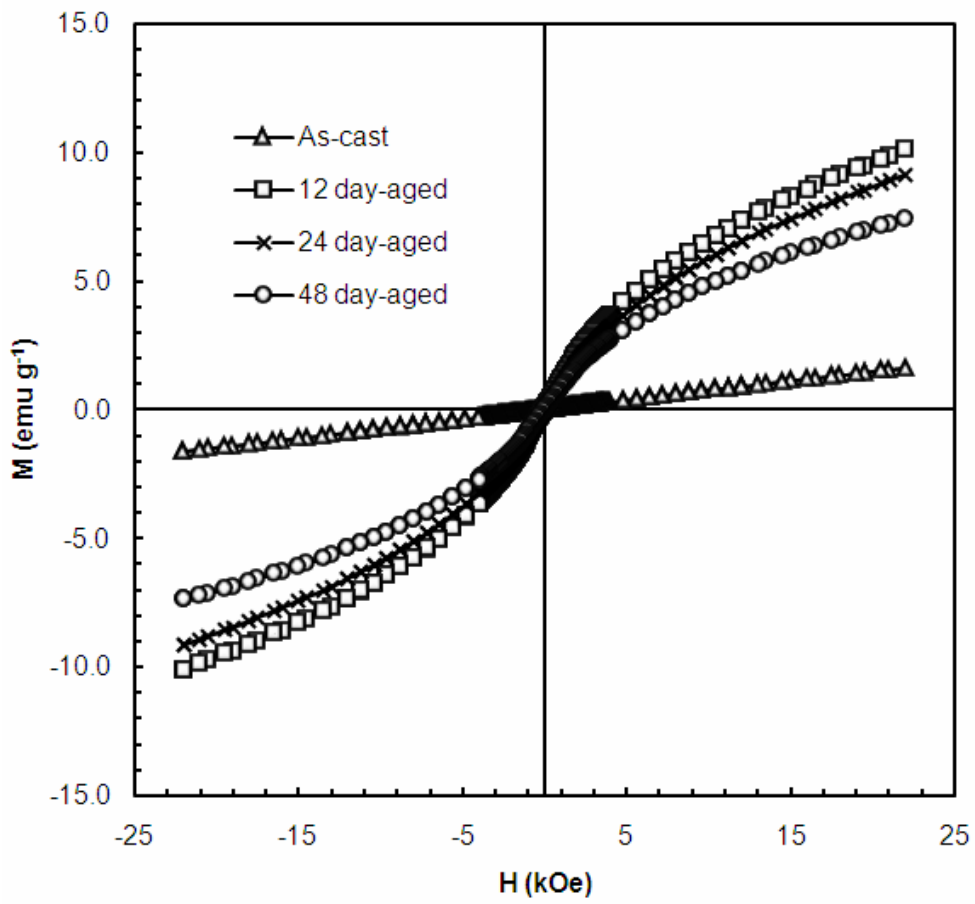

Figure 6.47 Hysteresis loops for the as-cast and aged $Ni_{50}Mn_{30}Al_{20}$ alloys measured at RT.

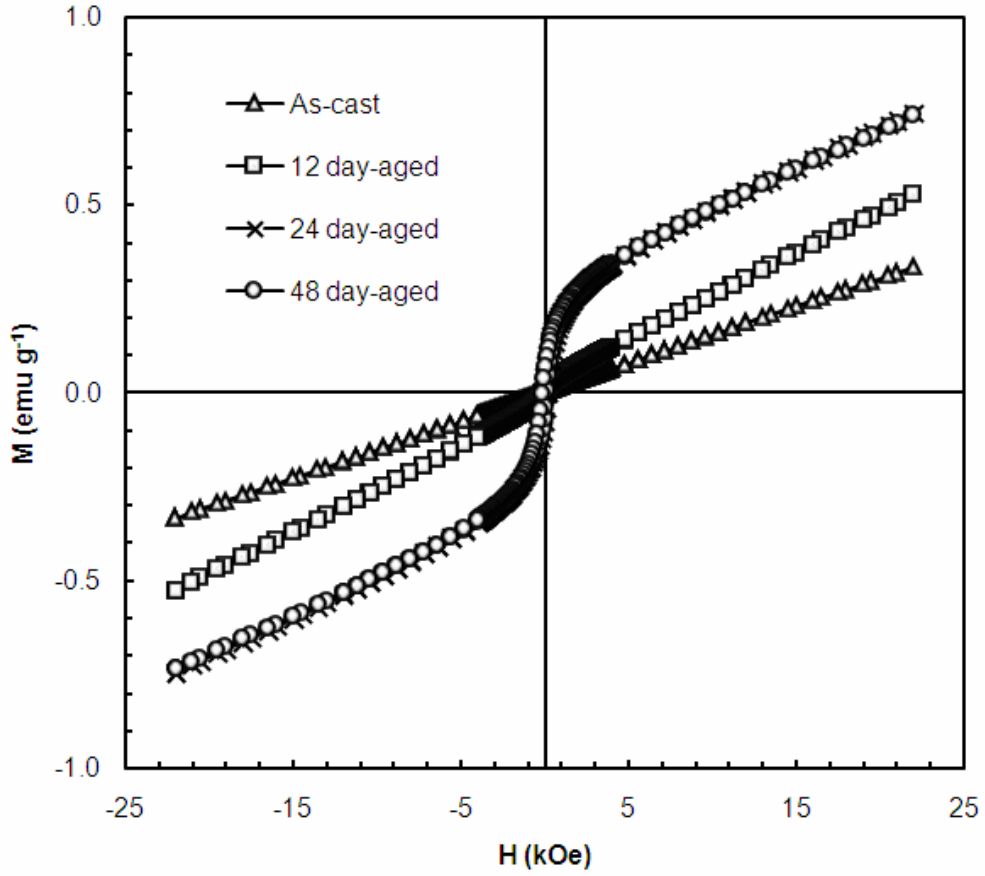

Figure 6.48 Hysteresis loops for the as-cast and aged $Ni_{50}Mn_{40}Al_{10}$ alloys measured at RT.

M-H curves given in Figures 6.45-6.48 showed that the as-cast $Ni_{50}Mn_{50-x}Al_x$ (x=20, 25, 30) alloys exhibit an antiferromagnetic behavior. In order to determine the T_N of these alloys magnetization is measured as a function of temperature. The peaks observed in Figures 6.49-6.51 correspond to the T_N in $Ni_{50}Mn_{50-x}Al_x$ (x=20, 25, 30) alloys. Referring back to the M-H curves of the as-cast samples (Figures 6.39-6.42), the linear behavior of the M-H curves is associated with the antiferromagnetism in these samples.

T_N are determined as 280 K, 240 K, and 297 K for the as-cast Ni_2MnAl, $Ni_{50}Mn_{20}Al_{30}$ and $Ni_{50}Mn_{30}Al_{20}$ alloys, respectively. These values are in agreement with the previously reported values [107, 112].

The peak observed in $Ni_{50}Mn_{30}Al_{20}$ (Figure 6.51) alloy is considerably sharper than the as-cast Ni_2MnAl (Figure 6.49) and $Ni_{50}Mn_{20}Al_{30}$ (Figure 6.50) alloys. This can be assumed to be an indication of a more pronounced antiferromagnetism in this alloy.

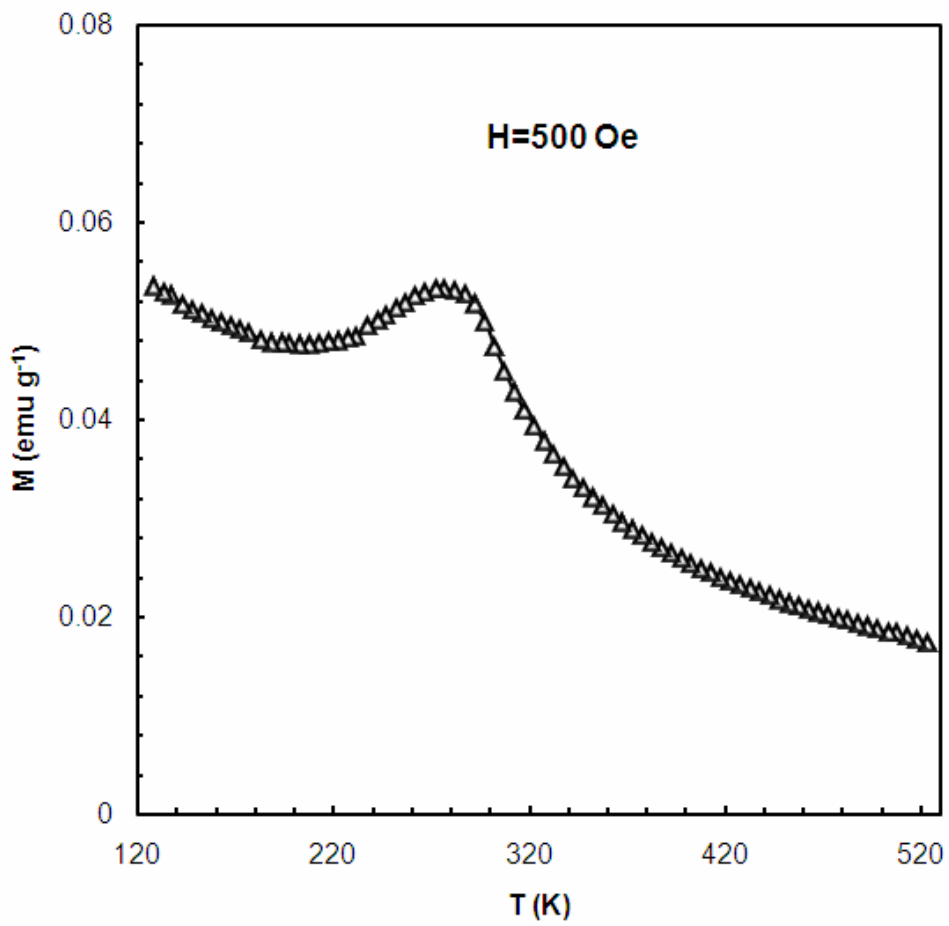

Figure 6.49 Temperature dependence of magnetization measured during cooling for the as-cast Ni_2MnAl alloy under a constant magnetic field of 500 Oe.

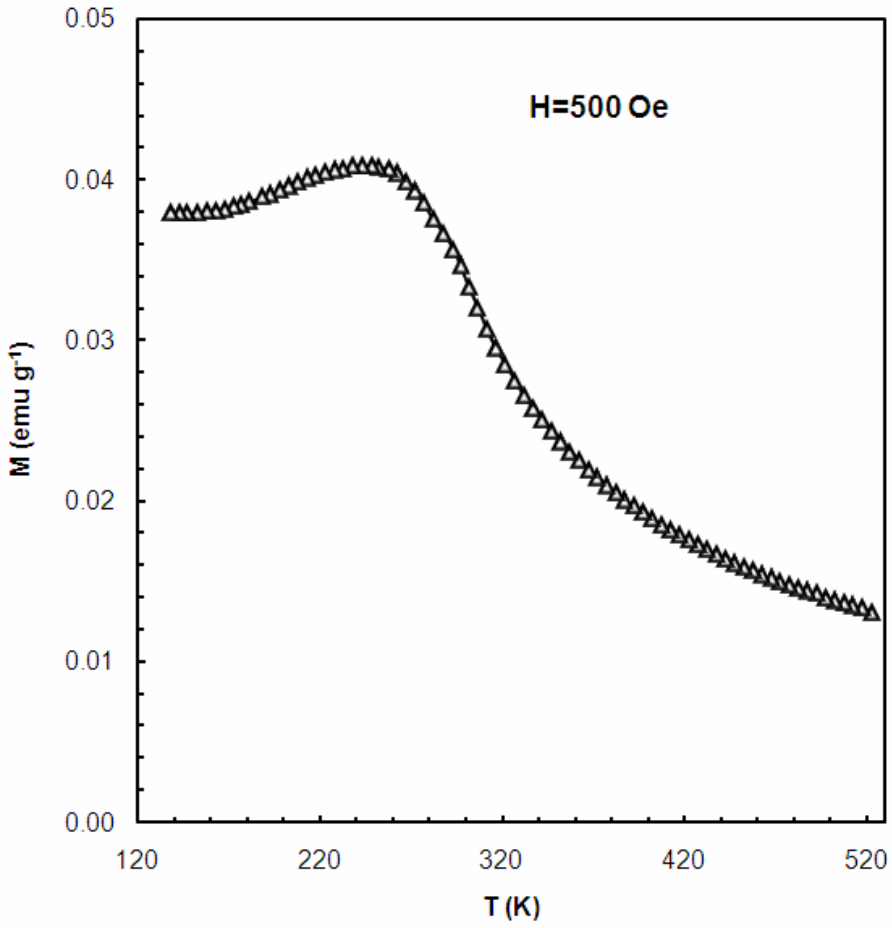

Figure 6.50 Temperature dependence of magnetization measured during cooling for the as-cast $Ni_{50}Mn_{20}Al_{30}$ alloy under a constant magnetic field of 500 Oe.

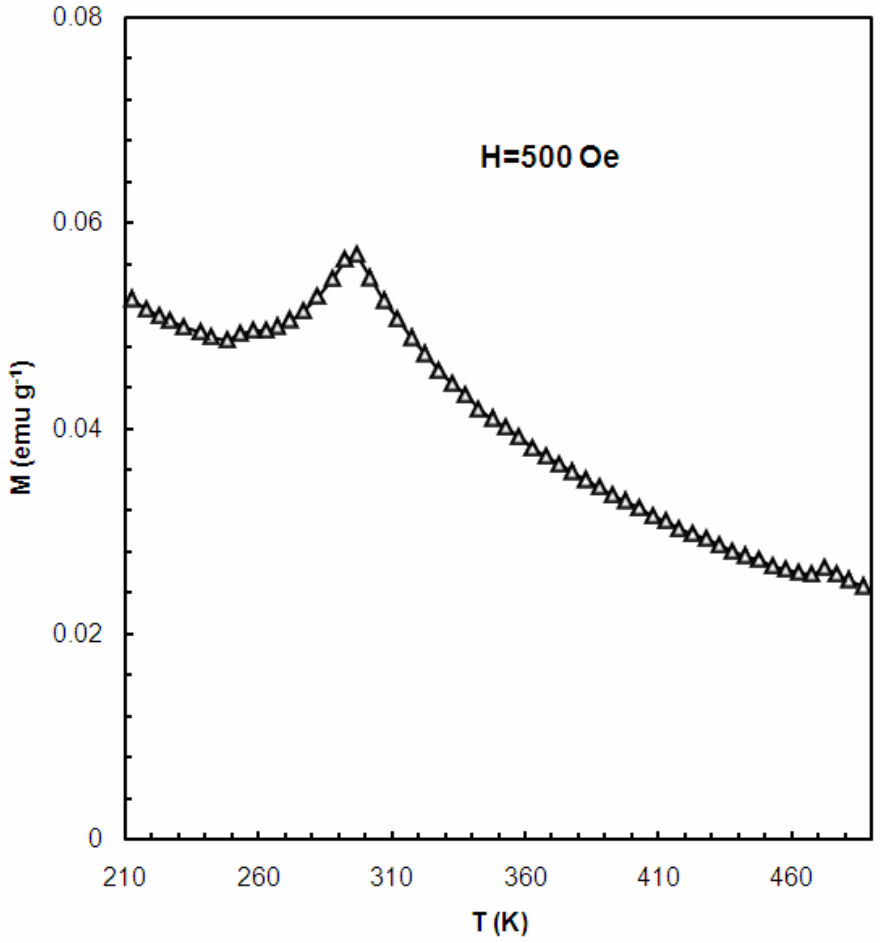

Figure 6.51 Temperature dependence of magnetization measured during cooling for the as-cast $Ni_{50}Mn_{30}Al_{20}$ alloy under a constant magnetic field of 500 Oe.

M-H curves given in Figures 6.45-6.48 indicated that the 48-day aged $Ni_{50}Mn_{50-x}Al_x$ (x=10, 20, 25, 30) alloys exhibit a ferromagnetic-like behavior. Magnetization is measured as a function of temperature to determine the T_C of these alloys. M-T curves measured under 500 Oe are given for the 48 day-aged $Ni_{50}Mn_{50-x}Al_x$ (x=10, 20, 25, 30) alloys in Figures 6.52-6.55. As can be seen from Figures 6.52-6.55 magnetization values measured during cooling and heating follow the same path, indicating the absence of a structural transition in the 48 day-aged $Ni_{50}Mn_{50-x}Al_x$ (x=10, 20, 25, 30) alloys in 120 K <T < 525 K.

M-T curve for the 48 day-aged Ni_2MnAl alloy (Figure 6.52) exhibits strong ferromagnetic features due to the following reasons. Magnetization of the 48 day-aged Ni_2MnAl alloy undergoes a sharp decrease and reaches values close to zero above the T_C, typical of a ferromagnetic material. T_C is determined as 376 K. M. Acet et al. reported T_C for nearly the same composition as 375 K [65]. In previous investigations, a peak just before the T_C was observed in all of the aged Ni-Mn-Al alloys. This is related to the antiferromagnetic↔paramagnetic transition and apperars because of the close values of T_C and T_N. In our sample this peak is almost negligible and below T_C, magnetization values are almost constant which is an expected feature from a ferromagnetic material. Furthermore, the magnetization values are greater in the 48 day-aged sample when compared to the as-cast Ni_2MnAl alloy. It is evident from Figures 6.45 and 6.52 that the dominant interaction in the 48 day-aged Ni_2MnAl alloy is the ferromagnetic interaction.

The M-T curve for the 48 day-aged $Ni_{50}Mn_{20}Al_{30}$ alloy given in Figure 6.53 shows a ferromagnetic-like behavior which is similar to the M-T curve of the 48 day-aged Ni_2MnAl alloy in many ways. The magnetization has constant values below T_C and reduces greatly above T_C. But the transition from ferromagnetic to paramagnetic is not as steep as the transition in the 48 day-aged Ni_2MnAl alloy. The drop in magnetization in the 48 day-aged $Ni_{50}Mn_{20}Al_{30}$ alloy occurs in a wider temperature interval than the 48 day-aged Ni_2MnAl alloy (Figure 6.52). There is a round peak near 273 K, below the T_C. This peak results from the close values of the T_N and T_C.

Near 273 K, the saturation of the magnetization of the ferromagnetic entity with decreasing temperature starts. Furthermore, the magnetization values are considerably greater for the 48 day-aged sample compared to the as-cast sample. However, from Figures 6.46 and 6.53 it is clear that antiferromagnetism coexists with ferromagnetism in the 48 day-aged $Ni_{50}Mn_{20}Al_{30}$ alloy.

S. Morito et al. reported temperature dependence of susceptibility for the annelaed (at 1123 K) $Ni_{50}Mn_{30}Al_{20}$ alloy in B2 phase [107]. Comparison of the quenched and furnace cooled samples showed that furnace cooled sample has $L2_1$ precipitates in the size of 2 nm whereas no $L2_1$ structure was observed in the quenched sample [107]. Furthermore the susceptibility of the furnace cooled sample is larger than the susceptibility of the quenched sample [107]. Based on these observations it can be assumed that in the aged $Ni_{50}Mn_{30}Al_{20}$ alloys that we have produced, a sligtly distorted $L2_1$ structure was obtianed. However, the amount of distortion in the $L2_1$ unit cell is quite small since in more distorted crystal structures like the tetragonal structure, more distinctive M-H curves were observed. Unlike Ni_2MnAl and $Ni_{50}Mn_{20}Al_{30}$ alloys which have low e/a values, the $Ni_{50}Mn_{30}Al_{20}$ alloy undergoes structural transitions from the B2 parent phase [106, 107]. However, the M-T curve given in Figure 6.54 indicates that martensitic (251 K) and premartensitic (292 K) transitions were suppressed. S. Morito et al. reported for nearly the same composition the suppression of the martensitic transition for the furnace cooled $Ni_{50}Mn_{30}Al_{20}$ alloy which was annealed at 1273 K [107]. It can be assumed that the sligtly distorted $L2_1$ precipitates formed in the 48 day-aged $Ni_{50}Mn_{20}Al_{30}$ alloy are responsible for the disappearance of the martensitic transformations in this alloy.

As shown in Figure 6.54, there is a peak at 332 K which is just below the T_C for the 48 day-aged $Ni_{50}Mn_{30}Al_{20}$ alloy. This peak is different from the peaks observed prior to the T_C in 48 day-aged Ni_2MnAl (Figure 6.52) and $Ni_{50}Mn_{20}Al_{30}$ (Figure 6.53) alloys. The peak observed in Figure 6.54 is significantly sharper and there is a remarkable alteration in magnetization. In $Ni_{50}Mn_{30}Al_{20}$ alloy a more enhanced antiferromagnetism is expected due to the excess Mn atoms. Increase in the number

of Mn atoms increases the possibilty of the Mn atoms to be nearest neigbours and this enhances the antiferromagnetic interactions. The observed peak before T_C is a result of the antiferromagnetic interactions. Based on the magnetization maesurements presented in Figures 6.47 and 6.54, it can be concluded that, ferromagnetism is certainly present in the 12, 24 and 48 day-aged $Ni_{50}Mn_{30}Al_{20}$ alloys. Since ferromagnetism is ascribed to the establishment of ordering in Mn-Al sublattice for Ni-Mn-Al alloys, the ferromagnetism probably results from the slightly distorted $L2_1$ phase that occured in the aged samples.

As shown in Figure 6.55, 48 day-aged $Ni_{50}Mn_{40}Al_{10}$ alloy exhibits a paramagnetic behaviour between 120 and 520 K due to the antiferromagnetic interactions between Mn atoms. From the magnetic field and temperature dependence of magnetization for the 48 day-aged $Ni_{50}Mn_{40}Al_{10}$ alloy given in Figures 6.48 and 6.55, it can be concluded that, there are ferromagnetic inhomogenities in the 48 day-aged $Ni_{50}Mn_{40}Al_{10}$ alloy. Unlike 48 day-aged $Ni_{50}Mn_{50-x}Al_x$ (x=20, 25 and 30) alloys, where a pronounced ferromagnetic behaviour was observed, there are traces of ferromagnetism in the 24 and 48 day-aged $Ni_{50}Mn_{40}Al_{10}$ alloys.

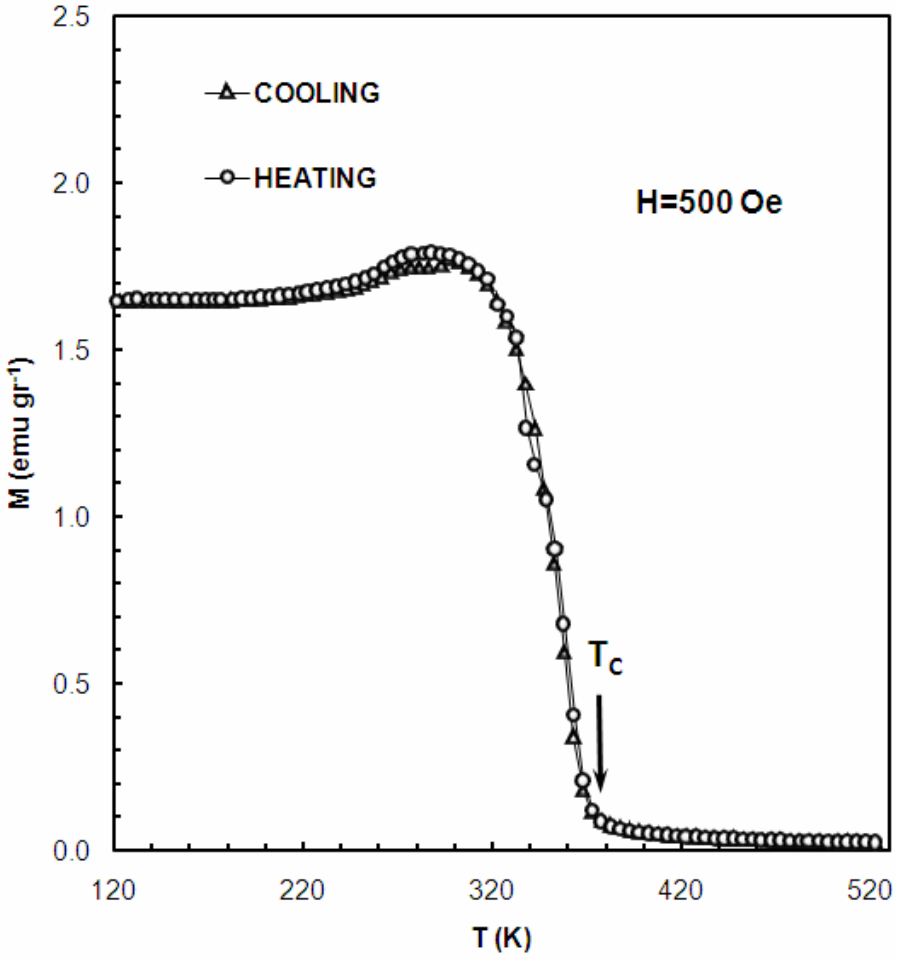

Figure 6.52 Temperature dependence of magnetization, measured during cooling and heating for the 48 day-aged Ni_2MnAl alloy under a constant magnetic field of 500 Oe.

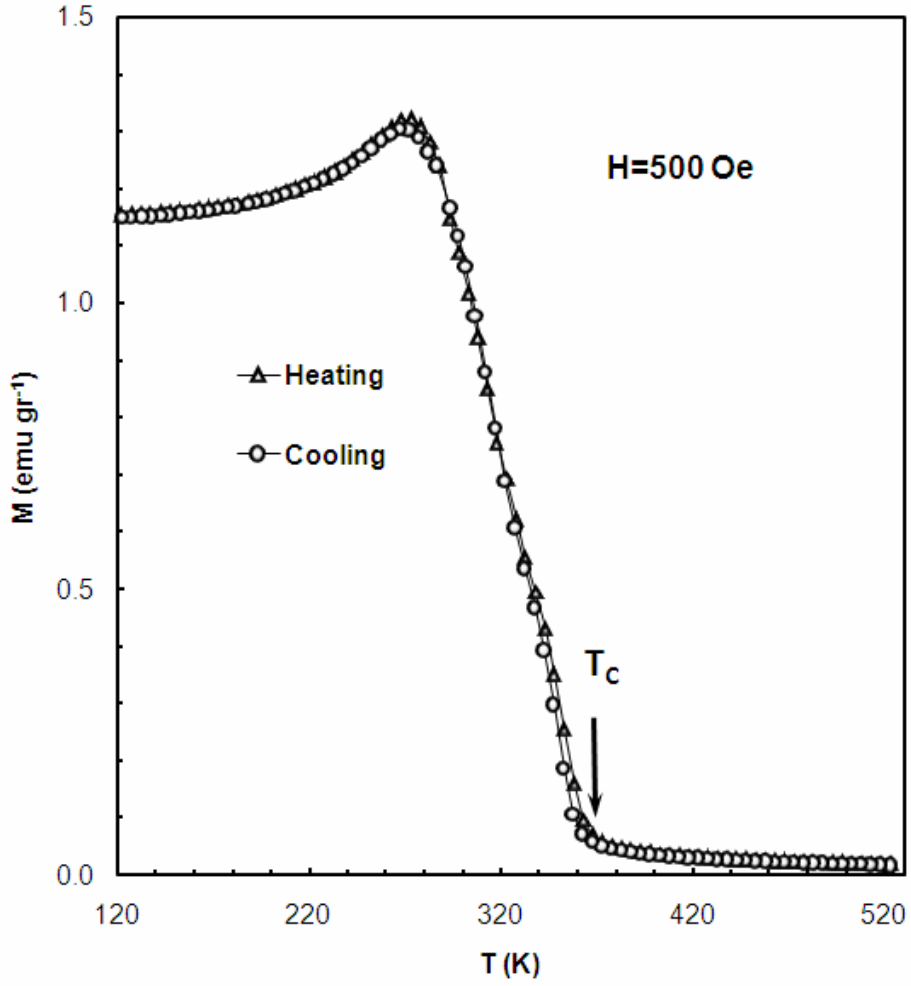

Figure 6.53 Temperature dependence of magnetization for the 48 day-aged $Ni_{50}Mn_{20}Al_{30}$ alloy under a constant magnetic field of 500 Oe.

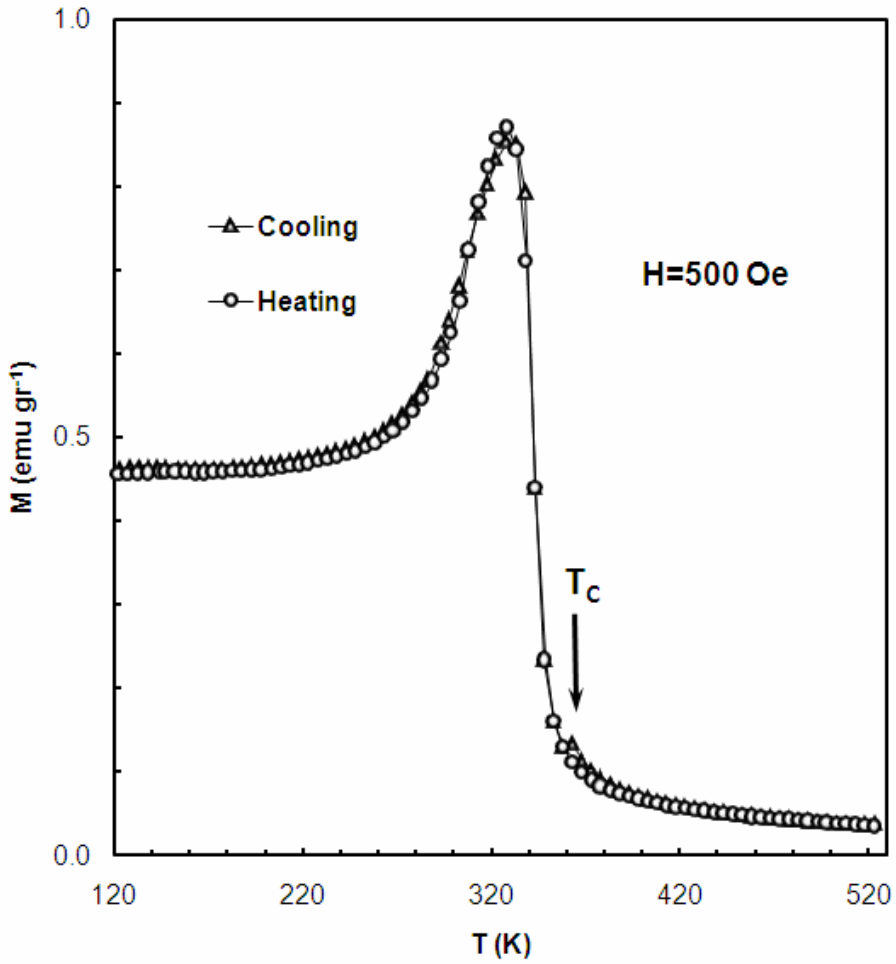

Figure 6.54 Temperature dependence of magnetization for the 48 day-aged $Ni_{50}Mn_{30}Al_{20}$ alloy under a constant magnetic field of 500 Oe.

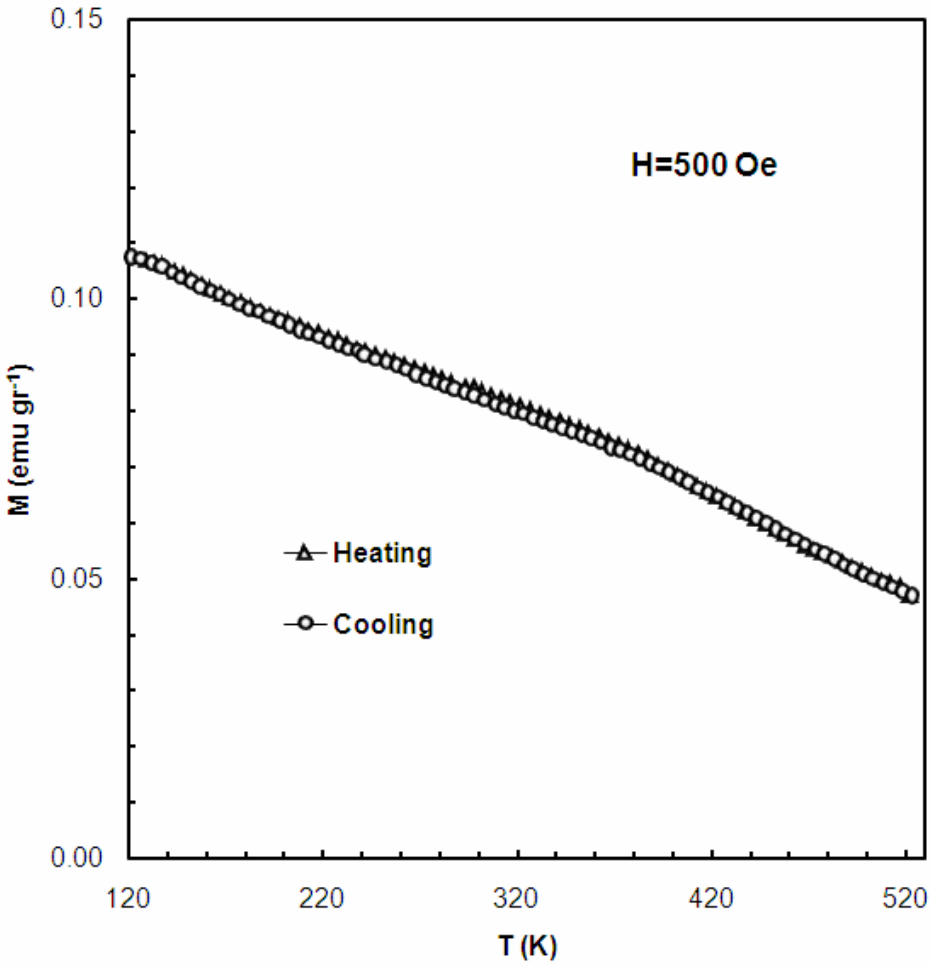

Figure 6.55 Temperature dependence of magnetization for the 48 day-aged $Ni_{50}Mn_{40}Al_{10}$ alloy under a constant magnetic field of 500 Oe.

There is a decrease in T_N with increasing Al content in as-cast $Ni_{50}Mn_{50-x}Al_x$ (x=20, 25 and 30) alloys. This is understandable since substitution of Al for Mn decreases the probability of the Mn atoms to be closest neighbours which results in the weakening of the antiferromagnetic interactions. As shown in Figure 6.56, T_N increases almost linearly with e/a . The T_C values determined for the 48 day-aged $Ni_{50}Mn_{50-x}Al_x$ (x=20, 25 and 30) from magnetization measurements are also presented in Figure 6.56. It is evident from Figure 6.56 that T_C values are almost constant with e/a between 7.3 and 7.7. T_C values determined as a function of e/a exhibit a very similar behaviour with the T_C values reported as a function of e/a for the Ni-Mn-Ga system. The Ni_2MnAl and Ni_2MnGa alloys have close T_C values. (for Ni_2MnAl T_C=376, for Ni_2MnGa T_C= 390 K) This is reasonable, because e/a of both alloys are same and T_C decreases very slightly with increasing e/a [53].

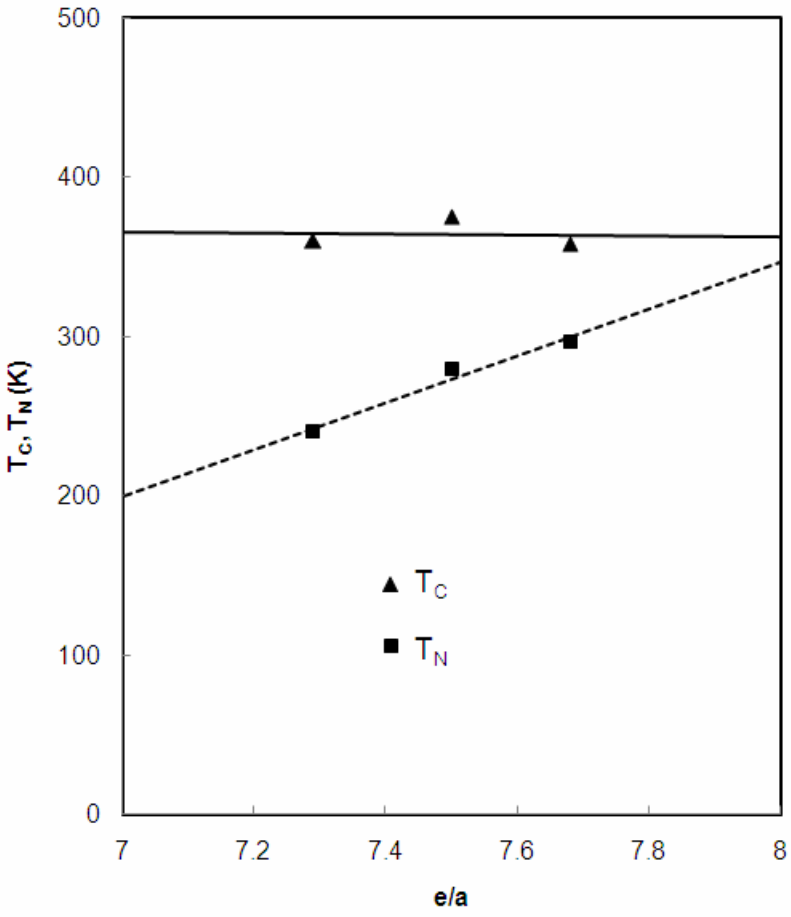

Figure 6.56 T_N of as cast and T_C of 48-day aged $Ni_{50}Mn_{50-x}Al_x$ (x=20, 25 and 30) alloys.

6.2.2.3. Magnetic and Structural Properties of Binary Ni-Al and Ni-Mn alloys

A_2BC-type Heusler alloys are well known for their exceptional magnetic properties that differ from the constituent elements and the binary alloys formed from these elements. However, equatomic Ni-Al and Ni-Mn alloys were prepared and characterized in order to make a comparison between the crystal structures and magnetic behaviours of the binary and the ternary Ni-Mn-Al Heusler alloys.

6.2.2.3.1. Structural Properties of Binary alloys

The RT XRD patterns of the $Ni_{50}Al_{50}$ and $Ni_{50}Mn_{50}$ alloys are shown in Figures 6.57 and 6.58. The RT XRD pattern for the as-cast $Ni_{50}Al_{50}$ alloy can be indexed according to the ordered B2 crystal structure (space group: Fm3m) with lattice parameter a= 2.88 Å. It is important to note that the lattice parameter of the B2 phase is half of the B2 phase previously mentioned for Ni-MnAl alloys. In the B2 structure of the binary Ni-Al alloy, Ni atoms occupy corner lattice sites while the Al atoms occupy body centered sites.

The XRD pattern for the as-cast $Ni_{50}Mn_{50}$ alloy can be indexed according to the $L1_0$ -type crystal structure (space group: P4/MMM) with lattice parameters a= b=3.715 Å and c=3.525 Å. The lattice parameter of the $L1_0$ phase is half of the double $L1_0$ phase previously mentioned for Ni-MnAl alloys.

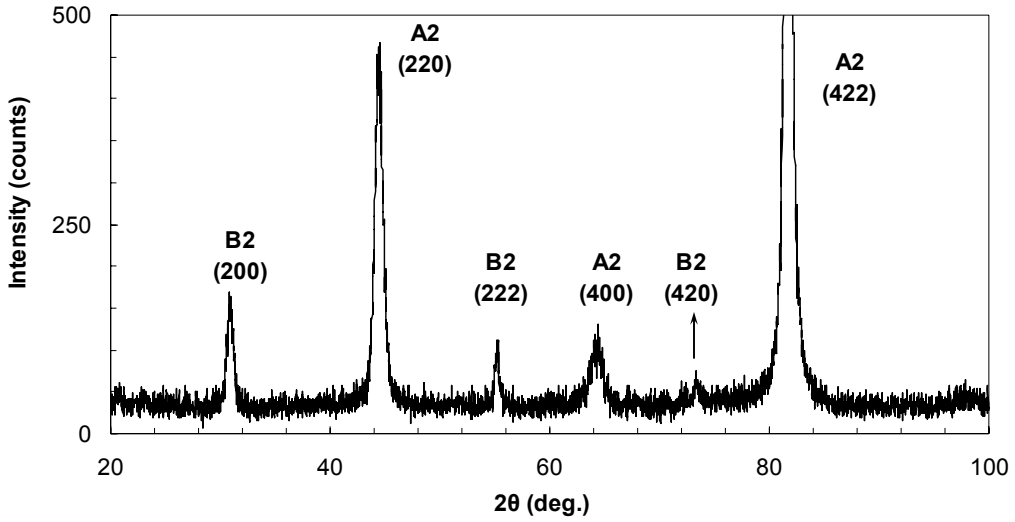

Figure 6.57 XRD pattern for the as-cast $Ni_{50}Al_{50}$ alloy measured at RT.

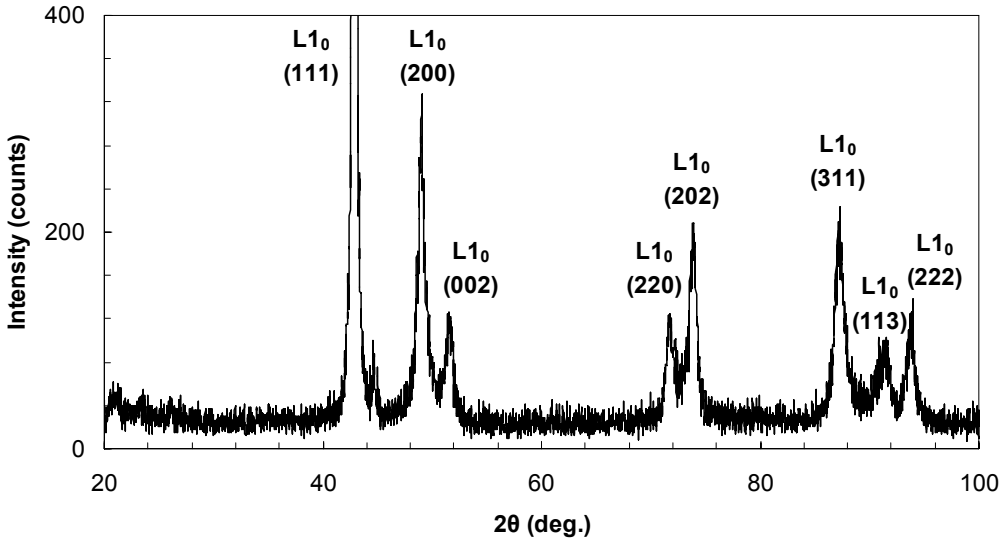

Figure 6.58 XRD pattern for the as-cast $Ni_{50}Mn_{50}$ alloy measured at RT.

6.2.2.3.2. Magnetic Properties of binary alloys

Magnetic field dependence of magnetization for the as-cast $Ni_{50}Al_{50}$ and $Ni_{50}Mn_{50}$ alloys are given in Figure 6.59 and 6.60, respectively. The magnetization values for the $Ni_{50}Al_{50}$ alloy are three orders of magnitude smaller than the magnetization values of Ni-Mn-Al Heusler alloys. $Ni_{50}Al_{50}$ can be considered as a non-magnetic material. Binary NiMn alloys were reported to exhhibit antiferromagnetic behaviour above 32 at.% Mn [138, 139]. Linear dependance of magnetization with magnetic field for the $Ni_{50}Mn_{50}$ alloy results from antiferromagnetic interactions between Mn atoms.

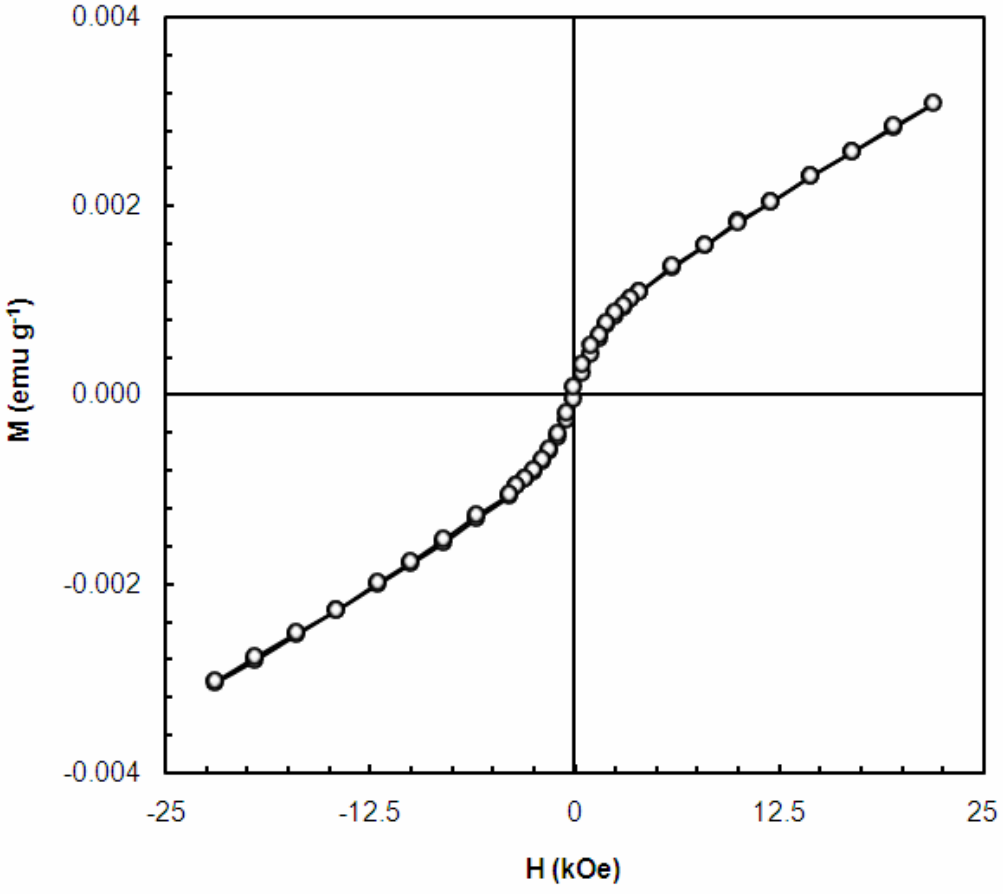

Figure 6.59 Hysteresis loop for the as-cast $Ni_{50}Al_{50}$ alloy measured at RT.

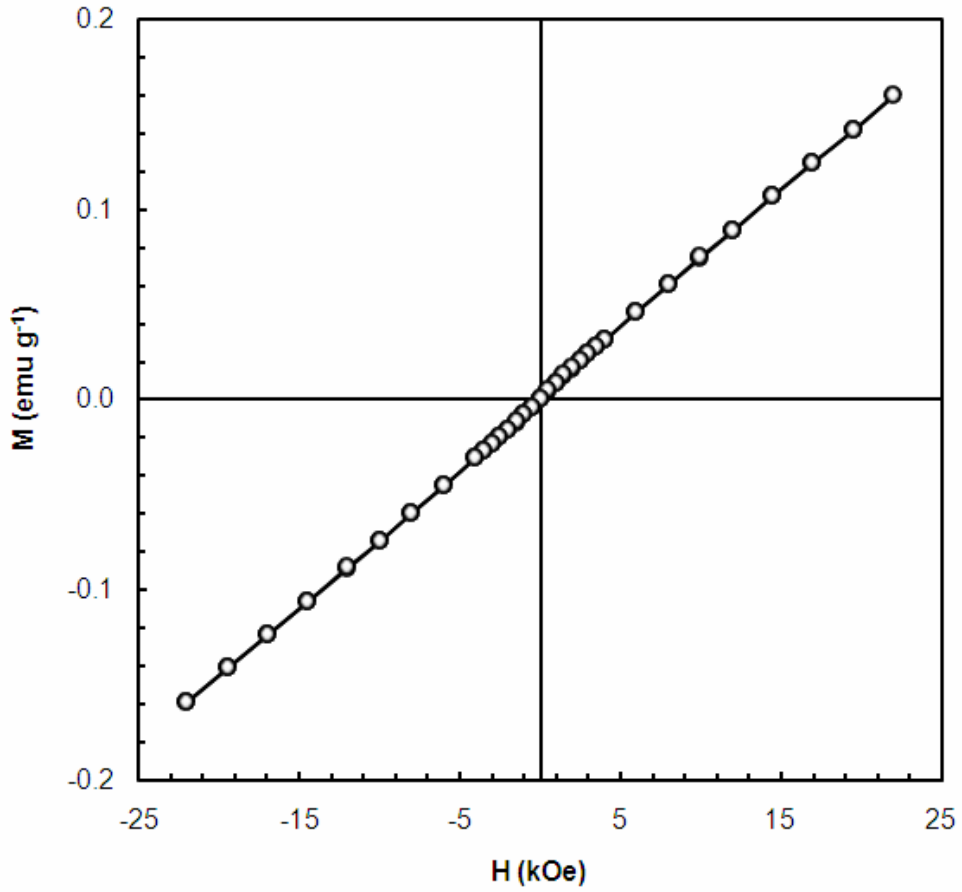

Figure 6.60 Hysteresis loop for the as-cast $Ni_{50}Mn_{50}$ alloy measured at RT.

The investigated ternary and binary Ni-Mn-Al alloys are marked in the isothermal phase diagram, presented in Figure 6.61. RT crystal structures are also given in this figure. The dotted line points out the constant composition where at. % of Ni is equal to 50.

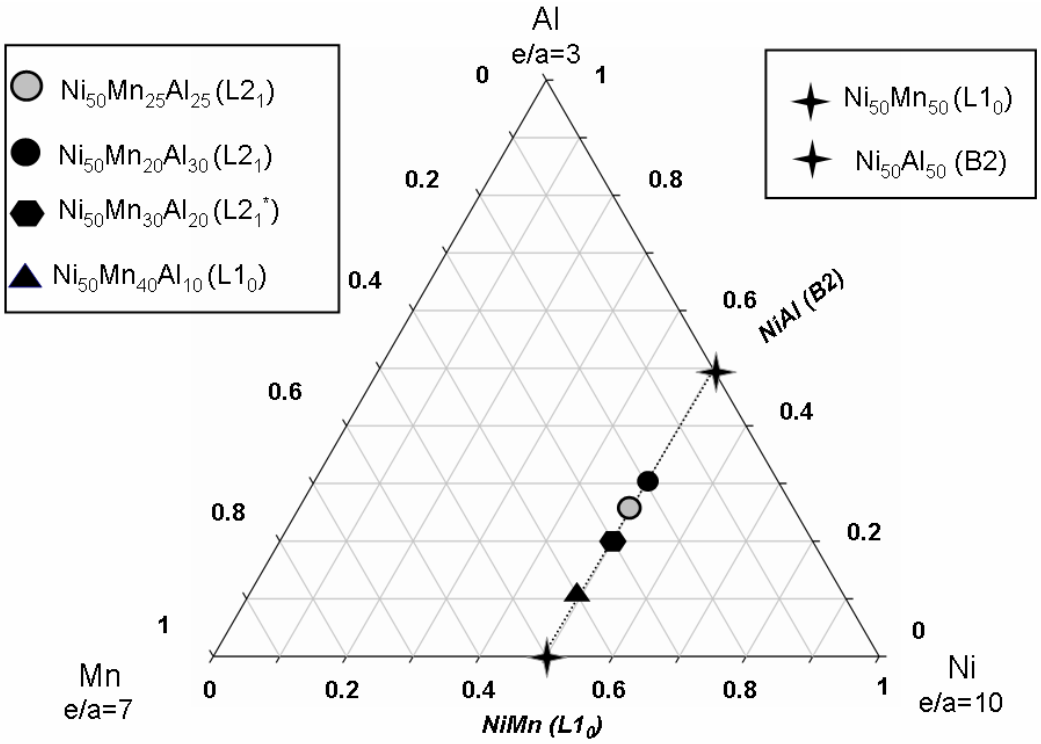

Figure 6.61 Ternary phase diagram showing the investigated binary and ternary Ni-Mn-Al alloys.

As stated previously, the NiAl alloy has a B2 –type structure with the lattice parameter that is half of the B2 observed in Ni-Mn-Al alloys. The B2 -type structure is stable with the substitution of Mn for Al up to 30 at. %. For the $Ni_{50}Mn_{30}Al_{20}$ alloy an intermediate phase with a slightly distorted cubic structure was observed and above 30 at. %, a martensitic $L1_0$ -type structure was observed. It is interesting to note that, a transition from the cubic B2 phase to the tetragonal $L1_0$ phase is occurs in $Ni_{50}Mn_{50-x}Al_x$ alloys in the composition range of $0<x<50$. In the middle region where the $20<x<30$, $L2_1$ -type structure was observed.

Another remarkable feature is the magnetic properties of the $Ni_{50}Mn_{50-x}Al_x$ alloys. Binary NiAl (x=50) and NiMn (x=0) alloys are non-magnetic and antiferromagnetic, respectively. But in between $20<x<30$, ferromagnetism was observed in Ni-Mn-Al Heusler alloys.

6.2.2.4. Magnetocaloric Effect in Ni_2MnAl Alloy

As shown in the previous section, coupling of T_M and T_C results in a first order magneto-structural transition in Ni-Mn-Ga alloys and quite large ΔS_M values. However, it was found that in the Ni-Mn-Al alloys the increase in the ferromagnetic $L2_1$ phase results in the supression of the martensitic transition. Therefore, MCE is calculated at the second order ferromagnetic↔paramagnetic transition in the 48 day-aged Ni_2MnAl alloy because the most marked ferromagnetism was observed in this alloy.

The ΔS_M values for the 48 day-aged Ni_2MnAl alloy were calculated from isothermal M-H curves shown in Figure 6.62. Sample was heated to 420 K prior to each measuremnt in order to achieve demagnetization. It can be seen from Figure 6.62 that above T_C (376 K) M-H curves are linear wheas there is an increase in curvature of these curves upon cooling. Nevertheless, the M-H curves for the 48 day-aged Ni_2MnAl alloy have a significantly higher slopes when compared to the M-H curves of the as-cast Ni_2MnGa alloy near RT.

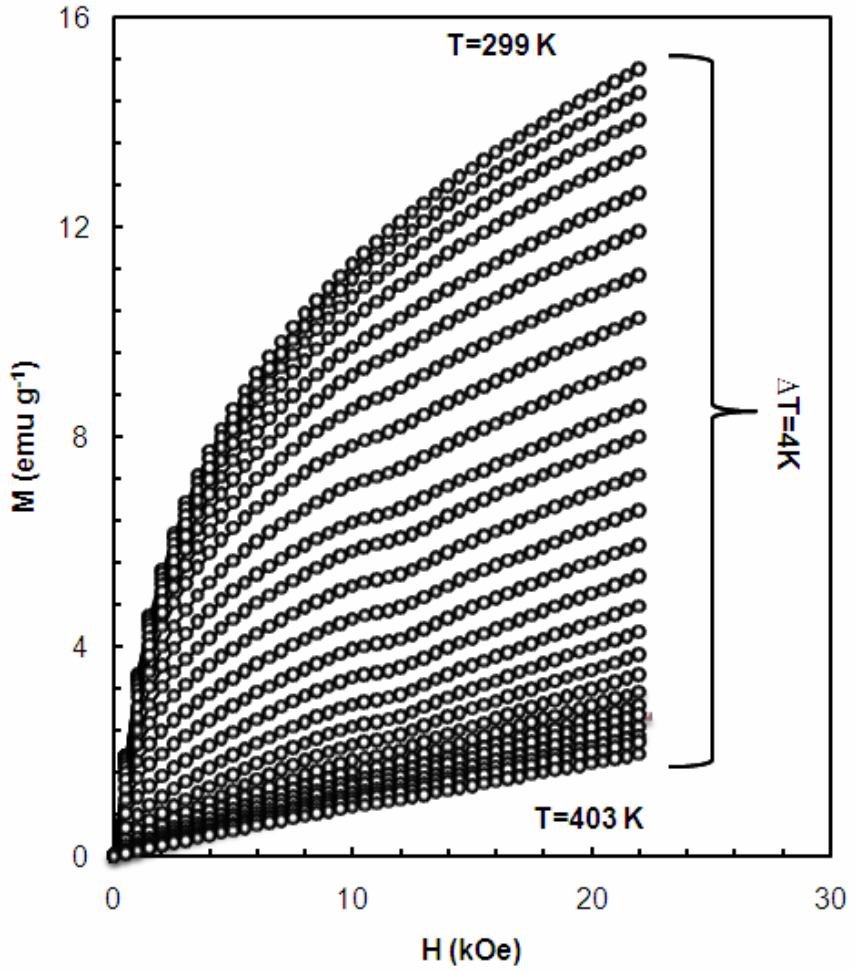

Figure 6.62 Magnetization of the 48 day aged Ni_2MnAl alloy as a function of magnetic field measured in the temperature interval of 299 K<T<403 K, ΔT=4K for clarity.

The ΔS_M values calculated for the 48 day-aged Ni_2MnAl alloy are shown in Figure 6.63 as a function of temperature. It is evident from Figure 6.63 that ΔS_M has its maximim (0.36 JKg^{-1} K^{-1}) near 335 K. The Ni_2MnGa alloy has significantly larger ΔS_M values than the 48 day-aged Ni_2MnAl alloy at the ferromagnetic↔paramagnetic transition [5, 10]. The relatively small ΔS_M values of the Ni_2MnAl alloy are due to the existance of antiferromagnetic B2 phase in this alloy.

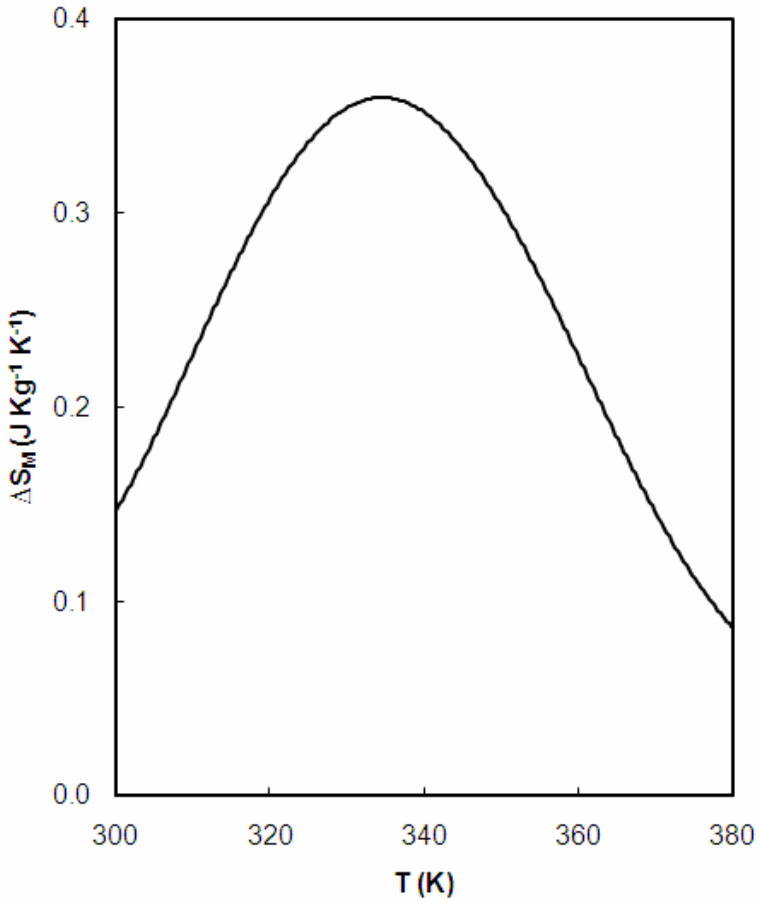

Figure 6.63 Magnetic entropy change of the 48 day-aged Ni_2MnAl alloy as a function of temperature.

CONCLUSIONS

The important points of the theoretical and experimental studies can be summarized as follows:

i. In the theoretical part of the thesis, partial ordering energies calculated by means of the electronic theory of alloys in pseudopotential approximation were used as input data in order to model the order-order and order-disorder phase transformations in full Heusler alloys. However, in the contrary of present approach, previous studies in the literature mainly involve fitting of experimental $L2_1 \leftrightarrow B2$ transformation temperature data to typical parabolic curves representing the $L2_1 \leftrightarrow B2$ transformation temperatures as a function of composition. Although, the results of our theoretical calculations are just qualitative in character, present study indicates that the statisco-thermodynamical theory of ordering by means of BWG method combined with electronic theory in the pseudopotential approximation can be successfully applied to the qualitative and/or semi-quantitative analysis of the complex $L2_1 \leftrightarrow B2$ and $B2 \leftrightarrow A2$ phase transformations for A_2BC-type ordered $Ni_{50}Mn_{50-x}C_x$ (C=Ga, In and Sb) and A_2BGa (A=Fe, Ni, Co; B=Ni, Mn, Co, Fe) full Heusler alloys.

ii. In the experimental part of the thesis, Ni-Mn-Ga and Ni-Mn-Al Heusler alloy systems were investigated. For the Ni-Mn-Ga system, the partial substitution of Ni for Mn in $Ni_{49+x}Mn_{25-x}Ga_{26}$ alloy increases the e/a and a ferromagnetic martensite alloy with a $L1_0$-type structure (I4/mmm) was observed for $Ni_{49+x}Mn_{25-x}Ga_{26}$ (x=5 and 7) alloys at RT. It is important to note that these alloys undergo a magneto-structural transition from ferromagnetic ($L1_0$) to paramagnetic ($L2_1$) near RT. The coupling of the magnetic and structural transformations observed in off-stoichiometric Ni-

Mn-Ga alloys is important for the occurence of MCE effect in these alloys. A maximum change in magnetic entropy, ΔS_M, of -1.84 $JKg^{-1}K^{-1}$ and -1.67 $JKg^{-1}K^{-1}$ were determined at the magneto-structural transition for $Ni_{54}Mn_{20}Ga_{26}$ and $Ni_{56}Mn_{18}Ga_{26}$ alloys, respectively. A significant drop in magnetization (~36%) and ΔS_M (~9%) was observed for a small increase in Ni concentration (7 at.%). The results are important for understanding the relationship between the structure, magnetism and the magnetocaloric effect in off-stoichiometric Heusler alloys.

iii. For the Ni-Mn-Al system, all the as-cast ternary Ni-Mn-Al alloys exhibit a paramagnetic behaviour due to antiferromagnetic interactions between Mn atoms. Low temperature aging (at 660 K) introduces ferromagnetism in $Ni_{50}Mn_{50-x}Al_x$ (x=20, 25, 30 and 40) alloys as a result of the establishment of ordering in the Mn-Al sublattice between Mn and Al atoms. Magnetization and XRD measurements revealed that there is no significant change in terms of ordering and magnetization for the 24 and 48 day-aged $Ni_{50}Mn_{50-x}Al_x$ (x=20, 25, 30 and 40) alloys. This suggests that further ordering at the Mn-Al sublattice has not developed significantly in that period or a metastable equilibrium between the B2 (antiferromagnetic) and $L2_1$ (ferromagnetic) phases was reached. The most pronounced ferromagnetic behaviour was observed for the Ni_2MnAl alloy. This is reasonable since the ferrromagnetic $L2_1$ phase was much more easily obtained in the stoichiometric alloy. The maximum ΔS_M value calculated for the 48 day-aged Ni_2MnAl alloy was found to be 0.36 JKg^{-1} K^{-1}. Another interesting result for this system is that, a transition from the cubic B2 to the tetragonal $L1_0$ –type structure occurs in the RT structures of $Ni_{50}Mn_{50-x}Al_x$ alloys in $0<x<50$.

REFERENCES

1. X. Moya, A. Planes, T. Krenke, M. Acet, M. Morin, J. L. Zarestky, T.A. Lograsso, Phys. Rev. B, 2006. **74**: p. 6.
2. A. N. Vasil'ev, V. V. Khovailo, I. E. Dikshtein, V. G. Shavrov, V. D. Buchelnikov, M. Matsumoto, S. Suzuki, T. Takagi, J. Tani, Phys. Rev. B, 1999. **59**: p. 1113
3. V. A. Chernenko, Scr. Mater. , 1999. **40**: p. 523
4. F. Hu, J. Sun, App. Phys. Lett., 2000. **76**: p. 3460
5. J. Marcos, L. Manosa, F. Casanova, X. Batlle, A. Labarta, B. Martinez, Phys. Rev. B, 2002. **66**: p. 224413
6. F. Albertini, S. Cirafici, E. A. Franceschi, M. Napoletano, A. Paouzi, L. Pareti, M. Solzi, J. Magn. Magn. Mater., 2004. **272-276**: p. 2047
7. A. A. Cherechukin, M. Matsumoto, V. D. Buchelnikov, Phys. Lett., A 2004. **326**: p. 146
8. C. Jiang, Y. Muhammad, L. Deng, W. Wu, H. Xu, Acta Mater., 2004. **52**: p. 2779
9. X. Zhou, W. Li, H.P. Kunkel, G. Williams, J. Magn. Magn. Mater, 2005. **293**: p. 854
10. L.Pareti, M. Solzi, F. Albertini, A. Paouzi, Eur. Phys. J. B, 2003. **32**: p. 303
11. M. Kreissl, K. U. Neumann, T. Stephens, K.R.A. Ziebeck J. Phys.: Condens. Matter., 2003. **15**: p. 3831
12. Mahendran, M., Smart Mater. Struct. , 2005. **14**: p. 1403
13. H. Hosoda,T. Sugimoto, K. Ohkubo, S. Miura, T. Mohri, S. Miyazaki, Int. J. Appl. Electromagn. Mech., 2000. **12**: p. 9
14. Y. Murakami, S.K., N. Nakanishi, H. Takehara, Acta Metall. 1971. **19**: p. 9.
15. V.V. Khovailo, T. Takagi , A. N. Vasil' ev, H. Miki , M. Matsumoto, R. Kainuma, Phys Atat.Sol., 2001. **183**: p. R1

16. R. W. Overholser, M. Wuttig, D.A. Neumann, Scr. Mater., 1999. **40**: p. 1095
17. K. Ishikawa, R. Kainuma, I. Ohnuma, K. Aoki, K. Ishida, Acta Mater., 2002 **50**: p. 2233
18. K. Ishikawa, H. Mitsui, I. Ohnuma, R. Kainuma, K. Aoki, K. Ishida, Mater. Sci. Eng. A, 2002. **A329–331**: p. 276
19. K K. Ishikawa, I. Ohnuma, R. Kainuma, K. Aoki, K. Ishida, J. Alloys Compd., 2004. **367:** p. 2
20. K. Kobayashi, K. Ishikawa, R.Y. Umetsu, R. Kainuma, K. Aoki, K. Ishida, Magn. Magn. Mater. , 2007. **310**: p. 1794
21. R. Kainuma, K. Urushiyama, K. Ishikawa, C. C.Jia, I. Ohnuma, K. Ishida Mater. Sci. Eng. A, 1997. **239-240**: p. 235
22. C.E. Reid, J. A. Barclay, J. L. Hall, S. Sarangi, J. Alloys Compd., 1994. **207**: p. 366
23. V. K. Pecharsky, K. A. Gschneider, J. Magn. Magn. Mater., 1999. **200**: p. 44
24. S.L. Russek, C. Zimm., Int. J. Refrrigeration, 2006. **29**: p. 1366
25. E. Brück, J. Phys. D: Appl. Phys. , 2005. **38**: p. R381.
26. E. Warburg, Ann. Phys., 1881. **13**. p. 141
27. P. Debye, Ann. Phys., 1926. **81**: p. 7.
28. W.F.Giauque, J. Amer.Chem. Soc, 1927. **7**: p.1864
29. W. F. Giauque, D.P. MacDougall., Phys. Rev., 1933. **43**: p.768
30. C. Zimm, A. Jastrab, A. Sternberg, V.K. Pecharsky, K.Jr. Gschneidner, M. Osborne, I. Anderson, Advances in Cryogenic Engineering, 1998. **43**: p. 1759
31. Ames Laboratory, U.S. Department of Energy, http://www.ameslab.gov/final/News/2001rel/01magneticrefrig.htm, "Last accessed date": June 2008.
32. V.K. Pecharsky, K.A. Gschneidner Jr., Jr. Phys. Rev. Lett., 1997. **78**: p. 4494
33. F.X. Hu, B.G. Shen, J.R. Sun, Z.H. Cheng, Appl. Phys. Lett., 2001. **78**: p. 3675

34. F.X. Hu, M. Ilyn, A.M. Tishin, J.R. Sun, G.J. Wang, Y.F. Chen, F. Wang, Z.H. Cheng, B.G. Shen, J. Appl. Phys., 2003. **93**: p. 5503
35. S. Fujieda, A.Fujita, K. Fukamichi, Appl. Phys. Lett., 2002. **81**: p. 1276
36. T. Hashimoto, T. Numusawa, M. Shino, T. Okada, Cryogenics, 1981. **21**: p. 647
37. H. Wada, Y. Tanabe, Appl. Phys. Lett., 2001. **79**: p. 3302
38. H. Wada, K. Taniguchi,Y. Tanabe, Mater. Trans., 2002. **43**: p. 7
39. A.M. Tishin, Cryogenics, 1990. **30**: p. 127
40. R.A. Swalin, , *Thermodynamics of Solids*. 1962, New York: Wiley.
41. I.P Bazarov, *Thermodynamics*. 1964, New York: Oxford.
42. S.V. Vansovskii , *Magnetism*. 1974, Jerusalem: Israel Program Sci. Translations.
43. B.R. Gopal, R. Chahine, M. Foeldeaki, T.K. Bose, Rev. Sci. Istrum., 1995. **66**: p. 232
44. B.R. Gopal, R. Chahine, T.K. Bose, Rev. Sci. Instrum., 1997. **68**: p.1818
45. S. Y. Danov, A.M. Tishin, V.K. Pecharsky, K.A. Jr Gschneidner, Rev. Sci. Instrum., 1997. **68**: p. 2432
46. K. Ullakko, J. K. Huang, C. Kantner, R. C. O'Handley, Appl. Phys. Lett., 1996. **69**: p. 1966
47. R. C. O'Handley, S. J. Murray, M. Marioni, H. Nembach, S. M. Allen, J. Appl. Phys., 2000. **87**: p. 4712
48. M. A. Marioni, R. C. O'Handley, S. M. Allen, S. R. Hall, D. I. Paul, M. L. Richard, J. Feuchtwanger, B. W. Peterson, J. M. Chambers, R. Techapiesancharoenkij, J. Magn. Magn. Mater., 2005. **290/291**: p. 35
49. J. Feuchtwanger, K. Griffin, J. K. Huang, D. Bono, R. C. O'Handley, S. M. Allen, J. Magn. Magn. Mater., 2004. **272-276**: p. 2038
50. V. V. Martynov, V. V. Kokorin, J. Phys. III, 1992. **2**: p. 739
51. S. J. Murray, M. Marioni, S.M. Allen, R.C. O'Handley, T.A. Lograsso, Appl. Phys. Lett., 2000. **77**: p. 886
52. P. Mullner, V.A. Chernenko, G. Kostorz, J. Appl. Phys., 2004. **95**: p. 1531

53. V.A. Chernenko, E. Cesari, V.V. Kokorin, I.N. Vitenko, Scr. Metall. Mater., 1995. **33**: p. 1239.
54. G. Pirge, C.V. Hyatt, S. Altintas, J. Mater. Proc. Tech., 2004. **155-156**: p. 1266
55. H. Hosoda, K. Wakashima, T. Sugimoto, S. Miyazaki Mater. Trans., 2002. **43**: p. 852
56. Y. Liang, H. Kato, M. Taya, T. Mori Scr. Mater., 2001. **45**: p. 569
57. O. Heczko, K. Jurek, K. Ullakko, J. Magn. Magn. Mater., 2001. **226-230**: p. 996
58. V. V. Khovailo, K. Oikawa, T. Abe, J. Appl. Phys., 2003. **93**: p. 8483
59. V.A. Chernenko, J. Pons, C. Segui, E. Cesari, Acta Mater., 2002. **50**: p. 53
60. V.V. Kokorin, M. Wutting, J. Magn. Magn. Mater., 2001. **234**: p. 25
61. S.Y. Chu, R. Gallagher, M. De Graef, M. E. McHenry, IEEE Trans. Magn., 2001. **37**: p. 2666
62. M.R. Sullivan, A.A. Shah, H.D. Chopra, Phys. Rev. B, 2004. **70**: p. 094428
63. Y. Li, Y. Xin, C. Jiang, H. Xu, Scr. Mater. , 2004. **51**: p. 849
64. P. Mullner, V.A. Chernenko, G. Kostorz J. Magn. Magn. Mater. , 2003. **267**: p. 325
65. M. Acet, E. Duman, E.F. Wassermann, L. Manosa and A. Planes, J. App. Phys., 2002. **92**: p. 5
66. L. Manosa, A. Planes, M. Acet, E. Duman, E.F. Wassermann, J. App. Phys., 2003. **93**: p. 3
67. J. Cui, T.W. Shield, R. D. James Acta Mater., 2004. **52**: p. 35
68. Y. Liang, Y. Sutou, T. Wada, C.C. Lee, M. Taya, T. Mori, Scr. Mater., 2003. **48**: p. 1415
69. T. Okazaki, T. Ueno, Y. Furuya, M. Spearing, N.W. Hagood Acta Mater. , 2004. **52**: p. 5169
70. K. Oikawa, T. Omori., Y. Sutou, R. Kainuma, K. Appl. Phys. Lett. , 2002. **79**: p. 3290
71. Y. Tanaka, T. Ohmori., K. Oikawa, R. Kainuma, K. Ishida, Mater.Trans., 2004. **45**: p. 427

72. H. Morito, A. Fujita., K. Fukamichi, R. Kainuma, K. Ishida, K. Oikawa Appl. Phys. Lett., 2002. **81**: p. 1657
73. K. Oikawa, T. Ota., F. Gejima, T. Ohmori, R. Kainuma, K. Ishida Mater. Trans., 2001. **42**: p. 2472
74. M. Wutting, J.Li., C. Craciunescu , Scr. Mater., 2001. **44**: p. 2393
75. T. Durieg, A. Pelton, D. Stockel, Mater. Sci. Eng. A, 1999. **273–275**: p. 149
76. Z. Nishiyama, Academic Press, 1978: p. 467
77. F. Heusler, Verh. Dtsch. Phys. Ges., 1903. **5**: p. 219
78. J. Kübler, A. R. Williams, C. B. Sommers, Phys. Rev. B, 1983. **28**: p. 1745
79. P. J. Webster, K. R. A. Ziebeck, in Alloys and Compounds of d-Elements with Main Group Elements, 1988.
80. P. J. Webster, K. R. A. Ziebeck, S. L. Town, M. S. Peak, Philos. Mag., 1984. **B49**: p. 295
81. T. Kira, K. Murata., T. Shimada, S-J. Jeong, S. Inoue, K. Koterazawa, K. Inoue , Mater.Sci. Forum, 2003. **426–432**: p. 2207.
82. H. Hosoda, T. Sugimoto, S. Miyazaki, Trans. Mater. Res. Soc. Japan, 2001 p. 26273
83. Y. Liang, H. Kato, M. Taya, T. Mori, Scr. Mater., 2001. **45**: p. 569
84. O. Heczko, K. Straka, K. Ullako, J. Phys. IV France, 2003. **112**: p. 9459
85. V. A. Chernenko, V. L'vov, J. Pons, E. Cesari , J. Appl. Phys., 2003. **93**: p. 2394
86. S. Besseghini, M. Pasquale, F. Passaretti, A. Sciacca, E. Villa , Scr. Mater., 2001. **44**: p. 2681
87. M. Stipcich, L. Manosa, A. Planes, M. Morin, J. Zarestky, T. Lograsso, C. Stassis Phys. Rev. B, 2004. **70**: p. 054115
88. A. Sozinov, A. A. Likhachev, N. Lanska, K. Ullakko Appl. Phys. Lett., 2002. **80**: p. 1746
89. K.Ullakko, Y. Ezer, A. Sozinov, G. Kimmel, P. Yakovenko, V.K. Lindroos Scripta Mater., 2001. **44**: p. 475
90. L. Manosa, A.G. Comas, E. Obrado, A. Planes, Phys. Rev. B, 1997. **55**: p. 11068

91. J. Pons, V. A. Chernenko, R. Santamarta, E. Cesari, Acta Mater., 2000. **48**: p. 3027
92. O.Heczko, A. Sozinov, K. Ulakko, IEEE Trans. Magn. , 2000. **36**: p. 3266
93. A. Sozinov, A.A. Likhachev, N. Lanska, K. Ulakko, V.K. Lindroos, J. Phy.IV, 2003. **112**: p. 955
94. O O. Tegus, E. Brück, L. Zhang, Dagula, K.H.J. Buschow, F.R. de Boer, Physica B, 2002. **319**: p. 174
95. K. Koho, J. Vimpari, L. Straka, N. Lanska, O. Söderberg, O. Heczko, K. Ullako, V.K. Lindros, J. Phys. IV France, 2003. **112**: p. 943
96. S.V. Soolshenko, N. Lanska, K. Ullako, J. Phys. IV France, 2003. **112**: p. 947
97. P. Entel, V.D. Buchelnikov, V.V: Khovailo, A.T. Zayak, W.A. Adeagbo, M.E. Gruner, H.C. Herper, E.F. Wassermann, J. Phys. D: Appl. Phys., 2006. **39** p. 865
98. H. Oikawa, T. Ota., F. Gejima, T. Ohmori, R. Kainuma, K. Ishida, Mater. Trans. , 2001. **42**: p. 2472
99. K. Oikawa, L. Wulff, T. Lijima, F. Gejima, T. Ohmori, A. Fujita, K. Fukamichi, R. Kainuma, K. Ishida, App. Phys. Lett., 2001. **79**: p. 3290
100. K. Oikawa, T. Ota, T. Ohmori, V. Morito, A. Fujita, R. Kainuma, K. Fukamichi, K. Ishida, App. Phys. Lett., 2002. **81**: p. 5201
101. K. Oikawa, T. Ota, Y. Sutou, T. Ohmori, R. Kainuma, K. Ishida, Mater. Trans., 2002. **43**: p. 2360
102. N. Lanska, O. Söderberg, A. Sozinov, Y. Ge, K. Ullakko, V. K. Lindroos, J. App. Phys., 2004. **95:** p. 80704.
103. F. Hu, B. Shen, J. Sun, G. Wu, Phys. Rev. B, 2001. **64**: p. 132412
104. K.Ishida, R. Kainuma, N. Ueno, and T. Nishizawa, Metall. Trans. A, 1991. **22A**: p. 441
105. Y. Sutou, I. Ohnuma, R. Kainuma, K. Ishida, Metall. Mater. Trans. A, 1998. **29A**: p. 2225
106. R. Kainuma, H Nakano, K. Ishida, Metall. Mater. Trans. A, 1996. **27A**: p. 4153

107. S. Morito, T. Kakeshita, K. Hirata, Otsuka, Acta Mater., 1998. **46**: p. 5377
108. R. Kainuma, F. Gejima, Y. Sutou, I. Ohnuma, K. Ishida, Mater Trans JIM, 2000. **41**: p. 943
109. A. Fujita, K. Fukamichi, F. Gejima, R. Kainuma, K. Ishida, App. Phys. Lett., 2000. **77**: p. 3054
110. F. Gejima, Y. Sutou, R. Kainuma and K. Ishida, Metall. Mater. Trans. A, 1999. **30 A**: p. 2721
111. C. Paduani, A. Migliavacca, M. L. Sebben, J. D. Ardisson, M.I. Yoshida, S. Soriano, M. Kalisz, Sol. Stat. Comm., 2007. **141**: p. 145
112. K.R.A. Ziebeck and P.J.Webster., J. Phys. F: Metal Phys., 1975. **5**: p. 1756
113. T. Büsgen, J. Fedt, R. Hassdorf, S. Thienhaus, M. Moske, M. Boese, A. Zayak, P. Entel, Phys. Rev.B, 2004. **70**: p. 014111
114. W.L. Bragg,F.R.S Williams, Proc. R. Soc. A, 1934. **15**: p. 699
115. V.V. Geichenko, V.M. Danilenko, A. A. Smirnov, Fiz. Metal. Metalloved., 1962. p. 321
116. T. Hirone, S. Matsuda., Bull. Inst. Phys. Chem. Res. Japan, 1950. **21**: p. 992
117. V.P. Fadin, V.E. Panin, E.D. Vasserlauf, M.F. Jorokov, Izv. Vyssh. Ucheb. Zaved., 1967. **10:** p. 25
118. K. Ishikawa, I.O., R. Kainuma, K. Aoki, K. Ishida J. Alloys Compd., 2004. **367**: p. 2.
119. A.A. Katsnelson, A.O. Mekhrabov, V.M. Silonov Fiz. Metal. Metalloved. , 1981. **52**: p. 661
120. A.O. Mekhrabov, M. Doyama, Phys. Stat. Sol.(B), 1984. **126**: p. 453
121. A. O. Mekhrabov, Z. M. Babaev, A.A. Katsnelsan Z.A., Matysina, Fiz. Metal. Metalloved. , 1986. **61**: p. 1089
122. A.O. Mekhrabov, A. Ressamoglu, T. Ozturk, J. Alloys. Compd., 1994. **205**: p. 147
123. A.O. Mekhrabov, M.V. Akdeniz, M.M. Arer, Acta mater., 1997. **45**: p. 1077
124. M.V. Akdeniz, A.O. Mekhrabov., Acta mater., 1998. **46**: p. 1185
125. A.O. Mekhrabov, M.V.Akdeniz, Acta mater., 1999. **47**: p. 2067

126. A.O. Mekhrabov, M.V.Akdeniz., Metall. Mater. Trans. A 2003. **34**: p. 721
127. A.O. Mekhrabov, M.V.Akdeniz., Model. Simul. Mater. Sci. Eng. , 2007. **15**: p. 1
128. Hubbard, J., Proc. Roy. Soc., 1957. **A240**: p. 359
129. A.O.E Animalu, Phys. Rev. B, 1973. **8**: p. 3542
130. K. Endo, T. Phayama, R. Kitamura, J. Phys. Soc. Jpn.,1964. **19**: p. 1494
131. R. Ducher, R. Kainuma, I. Ohnuma, K. Ishida, J. Alloys. Compd., 2007. **437:** p. 93
132. J. Pons, C. Segui, V. A. Chernenko, E. Cesari, P.Ochin, R. Portier, Mater. Sci. Eng. A, 1999. **273**: p. 315
133. V.A. Chernenko, E. Cesari, J. Pons, C. Segui, J. Mat. Res., 2000. **15:** p. 1496
134. R. Tickle, R.D.James, J. Magn. Magn. Mater., 1999. **195**: p. 627
135. E.M. Levin, V.K. Pecharsky, K. A. Gschneidner, Phys. Rev. B, 2000. **62:** p. R14625
136. F. Casanova, A. Labarta, X. Batle, J. Marcos, L. Manosa, A. Planes, S. De Brion, Phys. Rev. B, 2004. **69**: p. 104416
137. J. Chen, M.A. Gharghouri, C.V. Hyatt Proc. SPIE, 2004. **5387**: p. 549
138. W. Abdul-Razzaq, J.S.K., Phys. Rev. B, 1987. **35**: p. 1464
139. O. Moze, T. J. Hicks, P. von Blanckenhagen, J. Magn. Magn. Mater., 1984. **42**: p. 103

APPENDIX A

EDS ANALYSES OF Ni-Mn-Al AND Ni-Mn-Ga ALLOYS

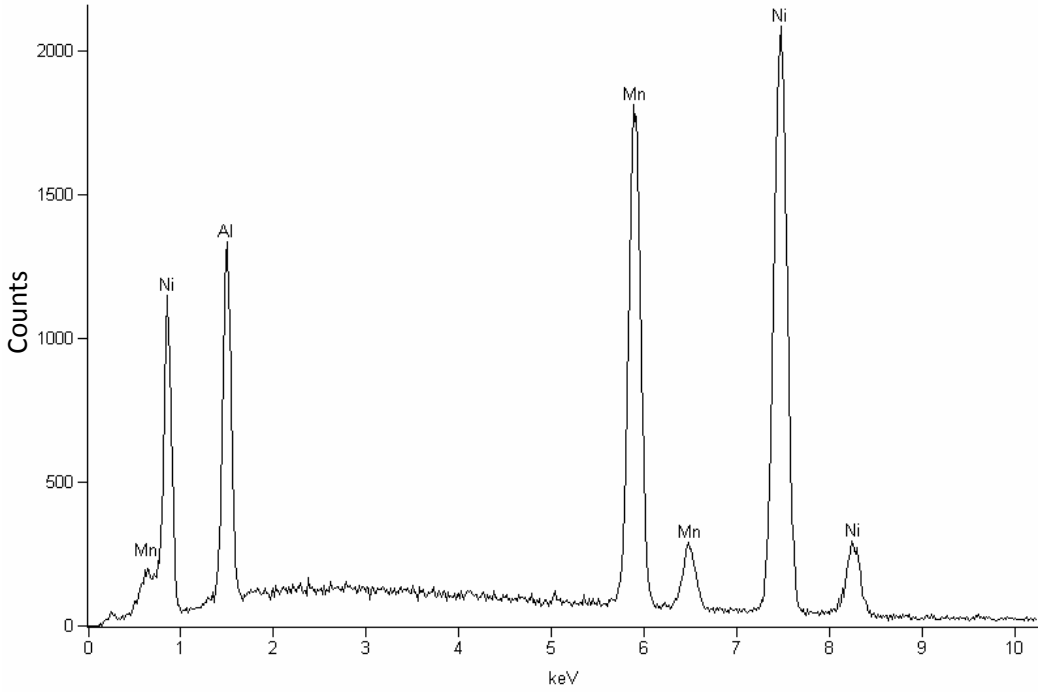

Figure A.1 EDS spectrum of the Ni_2MnAl alloy.

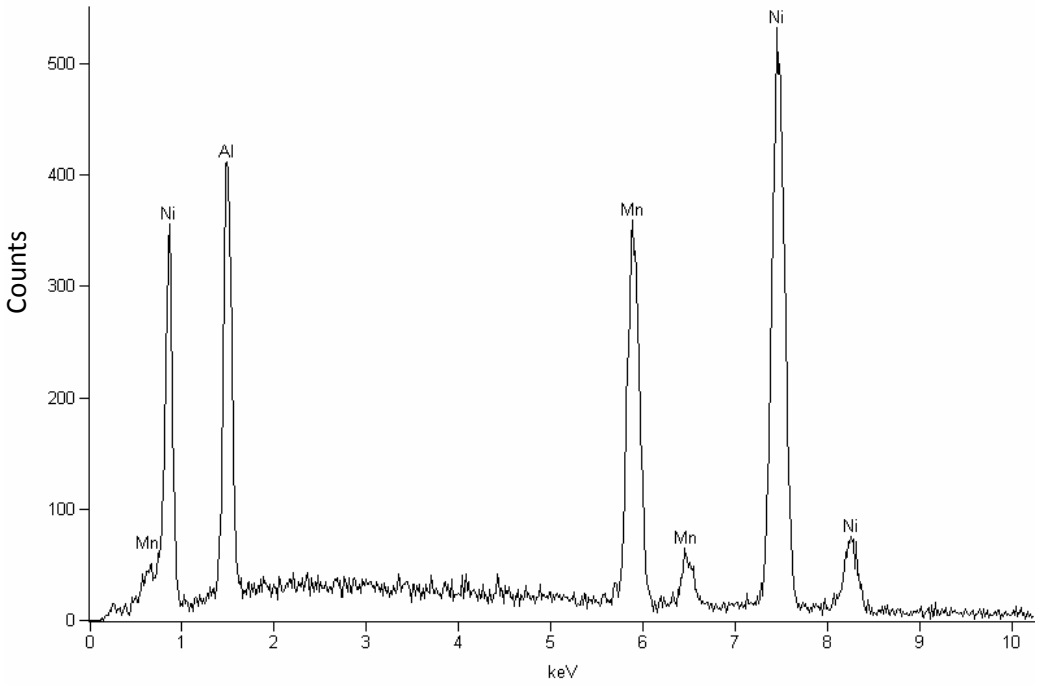

Figure A.2 EDS spectrum for the $Ni_{50}Mn_{20}Al_{30}$ alloy.

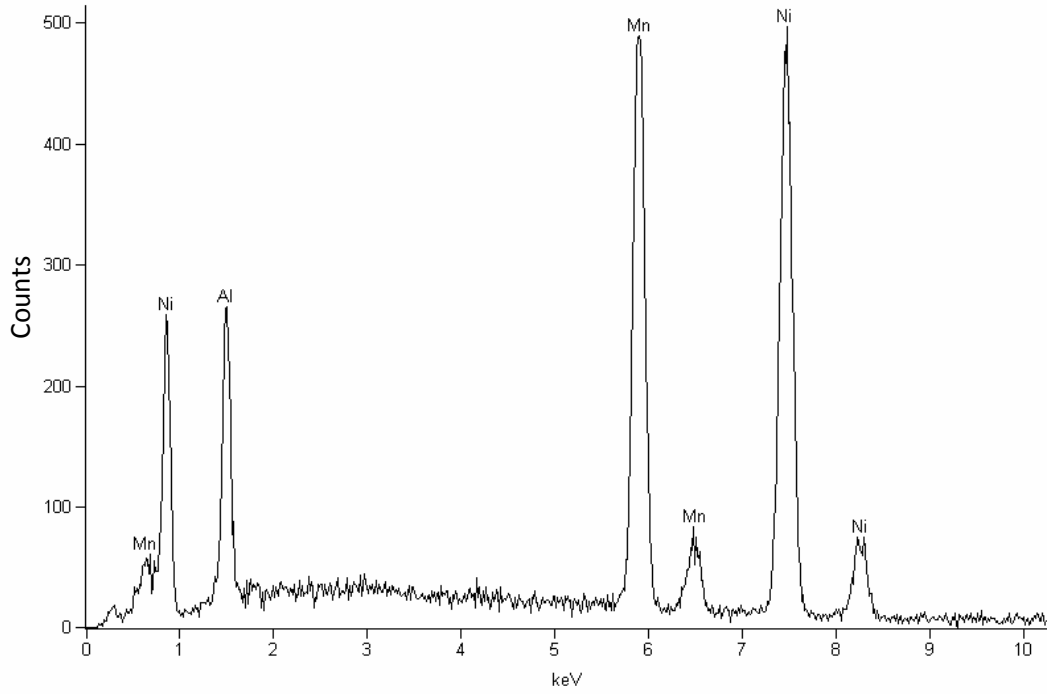

Figure A.3 EDS spectrum for the $Ni_{50}Mn_{30}Al_{20}$ alloy.

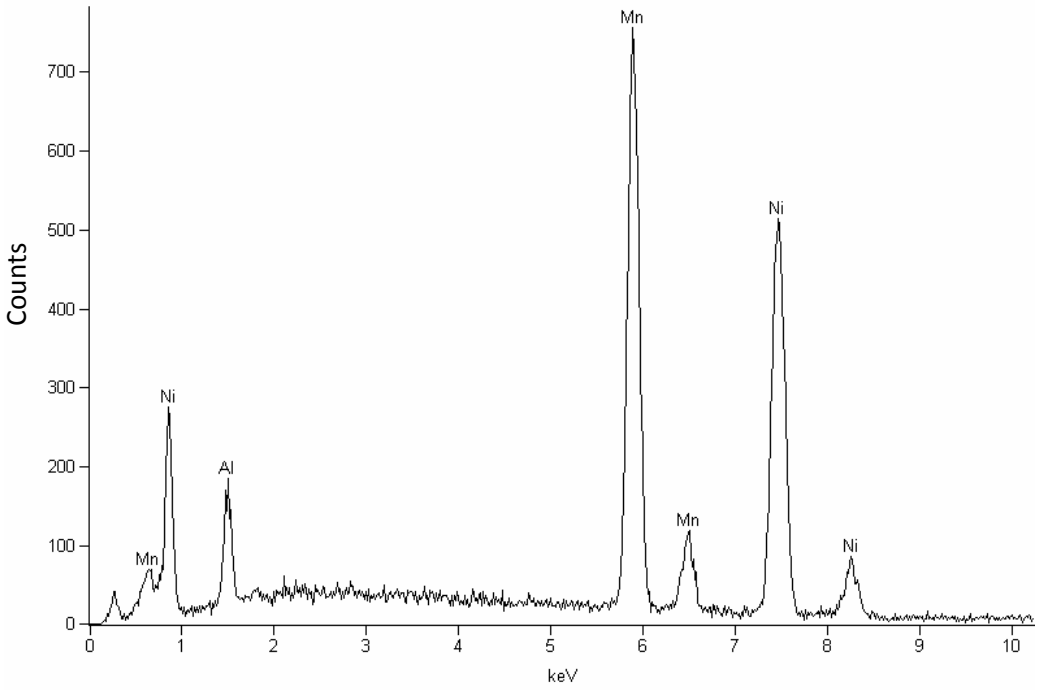

Figure A.4 EDS spectrum for the $Ni_{50}Mn_{40}Al_{10}$ alloy.

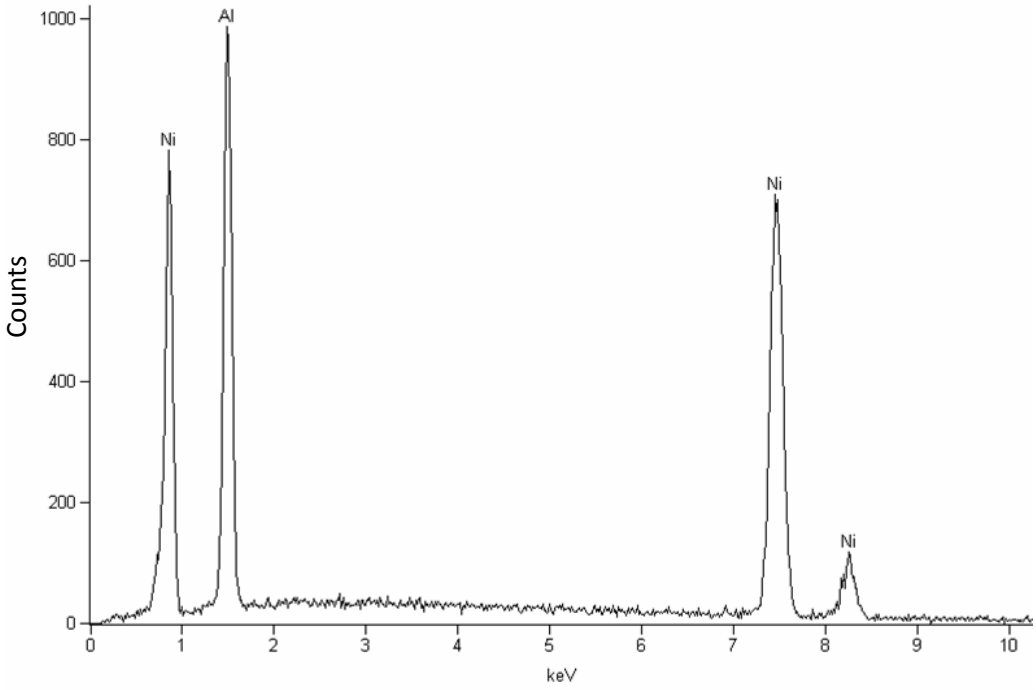

Figure A.5 EDS spectrum for the $Ni_{50}Al_{50}$ alloy

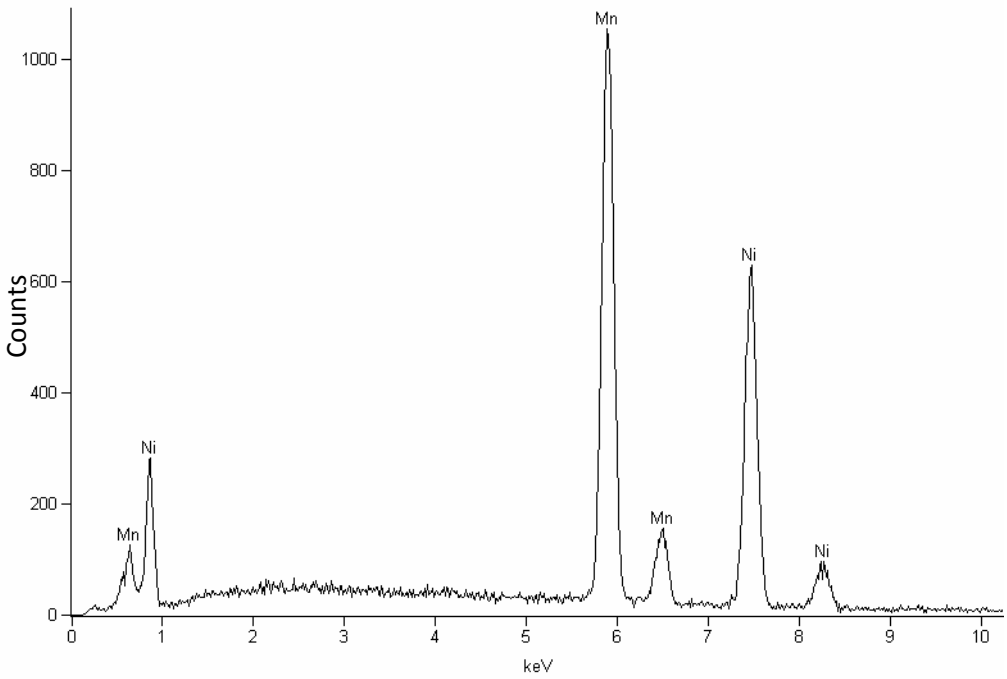

Figure A.6 EDS spectrum for the $Ni_{50}Mn_{50}$ alloy.

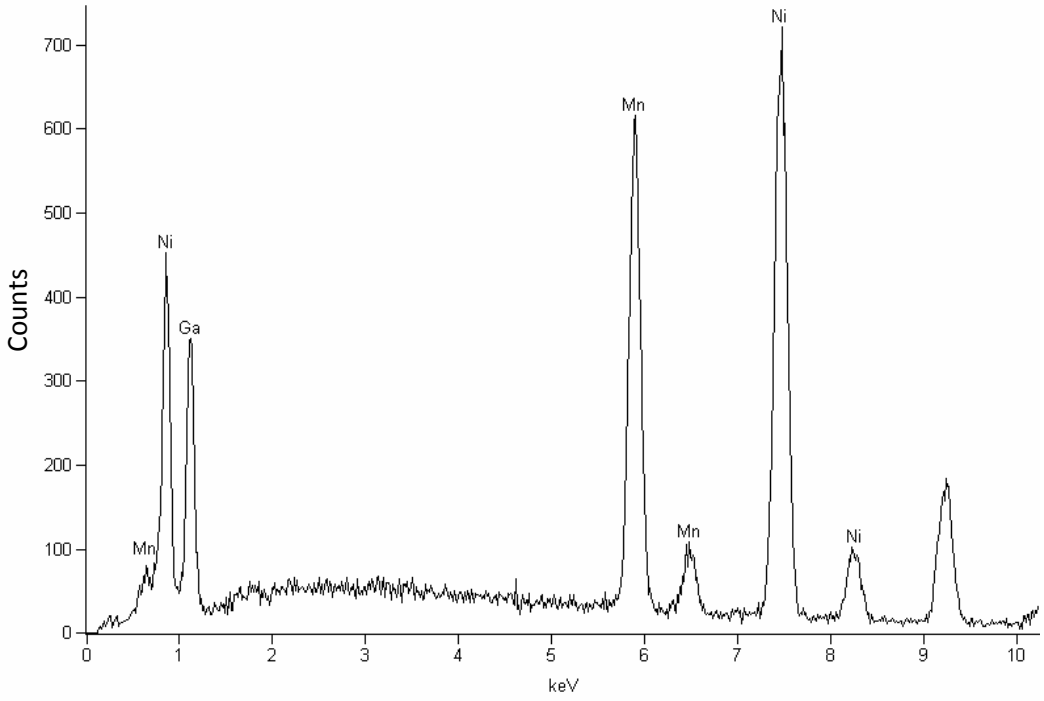

Figure A.7 EDS spectrum of the $Ni_{49}Mn_{25}Ga_{26}$ alloy.

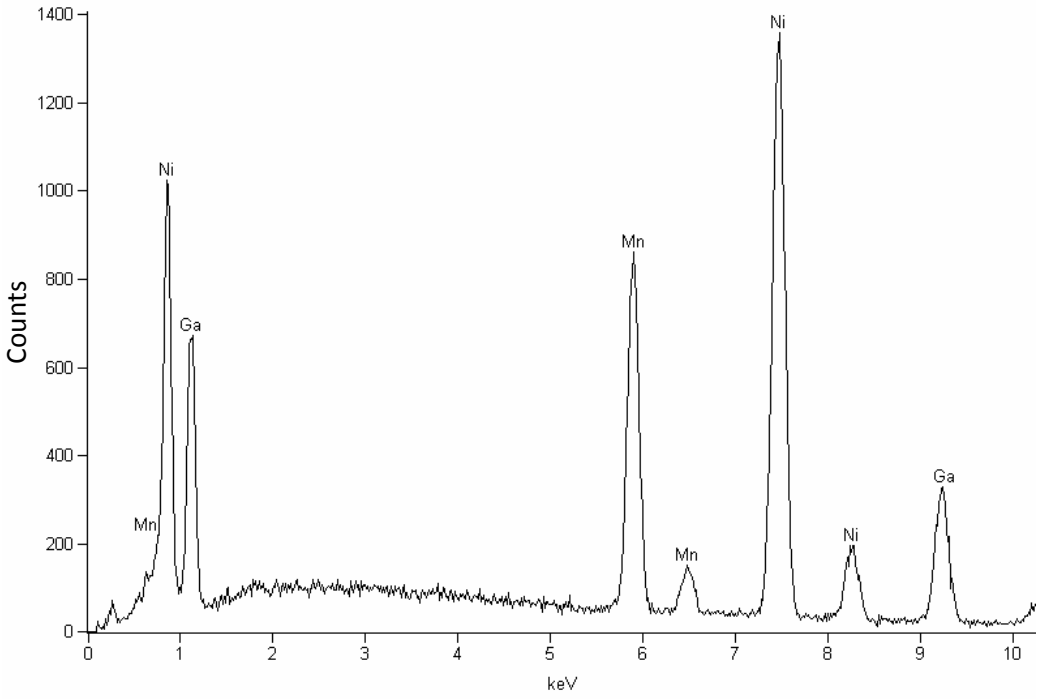

Figure A.8 EDS spectrum of the $Ni_{54}Mn_{20}Ga_{26}$ alloy.

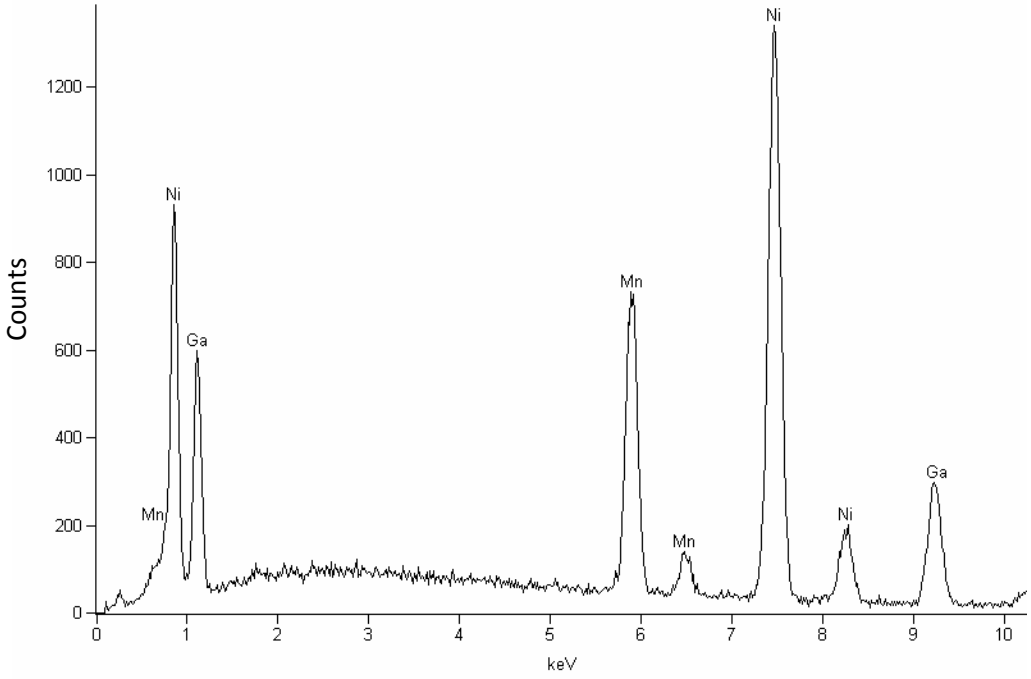

Figure A.9 EDS spectrum of the $Ni_{56}Mn_{18}Ga_{26}$ alloy.